FABRICATION AND CHARACTERIZATION OF FERROMAGNETIC TIPS FOR MAGNETIC RESONANCE FORCE MICROSCOPY

A Thesis

Presented in Partial Fullfillment of the Requirements for the Degree Bachelor of Science in Electrical and Computer Engineering with Distinction in the College of Engineering

By

Ross A. Steward,

* * * * *

The Ohio State University

2008

Examination Committee:

Prof. Chris Hammel, Co-Adviser

Prof. Bradley Clymer, Co-Adviser

Approved by

Co-Adviser
Department of Physics

Co-Adviser
Department of Electrical and Computer Engineering

ABSTRACT

This thesis deals with the custom fabrication of micron scale rare-earth ferromagnetic tips for use in magnetic resonance force microscopy (MRFM) experiments. Magnetic resonance force microscopy is a three dimensional subsurface imaging technique with the potential for atomic scale sensitivity and resolution. Tips are fabricated here by gluing particles as small as 1 μm to end of atomic force microscopy (AFM) cantilevers and milling the particles to a desired size and shape by sputtering material off using a focused beam of gallium ions. Particle gluing followed by focused ion beam (FIB) milling is shown here to be a promising and, so far, somewhat effective technique for fabricating optimal ferromagnetic tips for certain MRFM experiments. Fabrication results displaying ferromagnetic tips possessing sharp points with radii smaller than 50 nm are presented here. One of the major problems that has been encountered when FIB milling small particles is a loss in coercivity, sometimes from around 10,000 Gauss to less than 100 Gauss. Although indications lead to the conclusion that ion beam related damage is the cause of this decrease in coercivity, this assertion has not yet been proven. Based on the results of simulations and previous research it is believed that the loss of coercivity is related to particle heating caused by ion beam exposure, rather than direct damage caused by impinging ions from the beam or secondary recoil atoms knocked loose by the beam. This loss in coercivity is

one of several different sources of variability that leads to inconsistent fabrication results. Room temperature cantilever magnetometry is shown here to be an extremely sensitive, time efficient, and economical technique for determining certain magnetic properties of the tip including magnetic moment, hysteresis loop, and anisotropy. Results are presented here from measurements on magnetic tips micron scale dimensions and moments as small as 10^{-13} J/T. Calculations described here show the theoretical sensitivity limit of the room temperature magnetometer to be as high as 4×10^{-17} J/T using commercially available AFM cantilevers.

ACKNOWLEDGMENTS

I would like to begin by thanking all the past and current members of professor Chris Hammel's research group in the physics department at The Ohio State University who contributed in at least some capacity to my research. This includes but is not limited to Chris Hammel, Palash Banerjee, Denis Pelekhov, Yuri Oboukhov, Tim Mewes, Inhee Lee, Jongjoo Kim, KC Fong, Michael Boss, Vidya Bhallamudi, Youngwoo (Jay) Jung, Michael Herman, Josh Angelini, Jesse Martin, Seongjin Choi, Camelia Selcu, Eric Gingrich, Yulu Che. I would also like to thank Henk Colijn for his invaluable training and advice pertaining to use of the DB235 focused ion beam. I extend a special thanks to Tim Mewes with whom I worked very closely during the early parts of my research, Inhee Lee and Jonjoo Kim who fabricated several of the MRFM tips measured in the magnetometer and presented in this thesis, Denis Pelekhov who served as a reliable technical reference for many of the problems encountered during my research, and Palash Banerjee with whom I collaborated on nearly every aspect of my research and who has been a mentor to me during the last few years of work in professor Hammel's lab. Finally, I offer my sincerest thanks to Professor Peter Christopher Hammel, who several years ago extended an invitation to me to join his research group and collaborate with a truly gifted group of researchers. This experience has led me to more opportunities than I could have ever imagined

when I first joined the group, and I am incredibly thankful to have met such a distinguished professional who was so convinced of my potential. His support in all my academic and professional endeavors has been greatly appreciated.

DESIGN ELEMENTS

This senior thesis has been completed in accordance with the requirements for the degree Bachelor of Science in Electrical and Computer Engineering with Distinction. It is also being substituted (along with the required courses ECE H783 and ECE H683) for the normally required design course, ECE 682. In order for the senior thesis to fulfill the engineering design requirement normally fulfilled by ECE 682, the thesis research or related work must involve some aspect of design. The following will serve as a summary of the design elements performed during the work related to this senior thesis.

One design element developed in this research was a systematic procedure used to glue micron-scale ferromagnetic particles to the end of atomic force microscope cantilever and then mill these particles to a desired shape using a focused ion beam milling tool. This design process is described in detail in sections 3.3 and 3.4.2.

Another element of design performed in this research was the development of a mechanical fixture used to stabilize and precisely position the cantilever within the focused ion beam chamber. This fixture is described in detail in the last paragraph of section 3.4.2.

One final design produced during this research was a micropositioning alignment stage used to precisely position the cantilever relative to an optical fiber within the cantilever magnetometer vacuum chamber. This mechanical system is described in detail in section 4.3.1

TABLE OF CONTENTS

Page

List of Tables x

List of Figures xi

LIST OF TABLES

Table **Page**

LIST OF FIGURES

Figure **Page**

CHAPTER 1

Introduction

This thesis presents the results of various research efforts related to the fabrication and characterization of micron-scale ferromagnetic tips for use in magnetic resonance force microscopy (MRFM) experiments. In particular the research focuses on the advantages and disadvantages of focused ion beam (FIB) milling as a means of fabrication and the sensitivity and versatility of room temperature magnetometry as a method of characterizing these fabricated tips. A general overview of MRFM is presented to provide the necessary backround and motivation for the research efforts. Detailed descriptions and results are given for various stages of the fabrication process including magnetic particle gluing to atomic force microscopy (AFM) cantilevers and particle shaping using the FIB. Special attention is given to issues encountered during the FIB milling process such as electrostatic charging and FIB induced damage. A detailed description of cantilever magnetometry is then provided followed by magnetometry measurements evaluating the properties of various fabricated tips. Measurements and calculations documenting the capabilities and sensitivity of room temperature magnetometry are also discussed. Finally several conclusions are made regarding the successes of this approach to producing MRFM tips and suggestions for future research and improvements are given.

1.1 Motivation

Magnetic resonance force microscopy is a very promising imaging technology that may one day have extensive and field changing applications in a wide range of disciplines including medicine, biology, chemistry, materials science, and even computer science. The strength of MRFM is its ability to produce three dimensional (3D) subsurface images with potential sensitivity and resolution limitations at the atomic scale. Although each of these characteristics has been achieved individually by several different imaging technologies, there is currently no single imaging technology with the ability to achieve both. Such technology would represent a milestone in scientific progress.

One particularly promising, but not yet realized, application of the MRFM is the ability to image the molecular structure of proteins. This breakthrough would contriubute to several fields of science including chemistry, biology, and medicine. For instance, there is currently no *efficient* method of determining the molecular structure of proteins. Current methods involve performing numerous chemical procedures that can require a significant amount of time for the description of a single protein molecule. With improvements in the sensitivity and resolution of the MRFM, such molecules could be imaged on a time scale of hours, with complete documentation of the atomic composition and ordering of the molecule. This imaging capability could potentially be applied to many other materials and chemicals such as steels, ceramics, semiconductors [3], organic compounds, and even DNA. Some researchers have already reported investigations of microscopic biological elements using MRFM [4]. MRFM may also prove to be very useful for studying magnetic materials and interfaces with potential applications in the magnetic data storage industry [5].

In addition to its imaging capability, MRFM may have some promising applications in the field of computing [6, 7]. MRFM could prove very effective in the manipulation (writing) and imaging (reading) of electron spin states in quantum dots. This could be used to produce a new approach to data storage with a much higher information density than current devices, such as magnetic hard drives, are capable of achieving.

1.2 Magnetic Resonance Force Microscopy

The magnetic resonance force microscope (MRFM) is one of the newest types of scanned probe microscopes under development. What makes this instrument so promising is its ability to generate 3D subsurface images with the potential for atomic scale resolution and sensitivity [8, 9, 10, 11, 12, 13]. This is accomplished by combining aspects of 3D magnetic resonance imaging (MRI) with ultra-sensitive scanned probe microscopy (SPM). While there already exists scanned probe microscopes that can image single atoms, such as the atomic force microscope (AFM) and the scanning tunneling microscope (STM), no such instrument yet exists that is also capable of generating 3D subsurface images. The AFM and STM are limited to probing the surface of the sample they are investigating. This is due, in part, to the short-ranged nature of the interactions they exploit. In the case of the STM, the image is generated by the quantum-mechanical tunneling phenomenon which only occurs on the scale of a few angstroms. Because this tunneling behavior occurs only in conductive samples the range of materials which can be imaged by STM is also limited. AFM relies on slightly longer range atomic force interactions such as Pauli repulsion, Van der Walls attraction, and the Lennard-Jones interaction force, but is

still limited to sample surface imaging. Magnetic resonance force microscopy, however, exploits the comparatively long-range force generated by magnetic dipolar interaction and controls the length scale of the interaction using magnetic resonance condition. This control over the resonance condition, and therefore depth of the probe-sample interaction, gives the MRFM the extra spatial dimension that other scanned probed microscopes lack.

Like many other scanned probe microscopes, the MRFM uses mechanical oscillators (cantilevers) to detect the interaction force used to construct an image. The cantilever is essentially a tiny leaf spring with one end fixed and the other end free to vibrate. Since cantilevers designed for the MRFM are not, for the most part, commercially available, AFM cantilevers are commonly used. In some cases, cantilevers are custom fabricated [14, 15] to produce the most desirable specifications for use in certain MRFM experiments. In order for the cantilever to be useful for MRFM studies, the free end of the cantilever must bear some quantity of magnetic material. It is this magnetic material, whether a deposited layer or an attached particle, which couples the magnetic interaction with the sample to a measurable force and displacement on the cantilever. An alternative imaging setup uses a fixed magnetic probe and positions the sample on the vibrating cantilever. In either case, this crucial link between the sample and a measurable force makes the magnetic probe one of the most important parts of the MRFM.

Now that the potential of the MRFM has been thoroughly described, the relevance of the research presented here to MRFM will be explained. The sensitivity and resolution of the MRFM is heavily dependent on the physical properties of the cantilever and magnetic properties of the tip. The magnetic tip and cantilever material as well

as the magnetic tip and cantilever size/shape all influence the interaction between sample and cantilever. This is why establishing consistent fabrication procedures and characterization techniques for the MRFM probe tip is one of the most crucial steps in the design of such an instrument.

1.3 Probe Tip Fabrication

Because the MRFM is still in the developmental stage and has not made it to the commercial market yet there are no commercially available probes that are well-suited for MRFM studies. To solve this problem some experimentalists have chosen to fabricate both cantilever and magnetic tip in efforts to produce optimal probes [14]. The approach used in the research efforts here, however, was to buy commercially available AFM cantilevers and modify them appropriately to meet the requirements of the particular experiment they will be used in. In most cases this involves removal of the current etched probe tip and attachment of a new magnetic tip. This is usually accomplished in three main steps. The first step is removal of the prefabricated cantilever tip using a focused ion beam (FIB) milling instrument. The second step is manual attachment of a micron scale magnetic particle using epoxy. The final step involves the shaping and dimensioning of the particle again using the FIB milling instrument. The above procedures will all be discussed in much greater detail in chapter 3.

1.4 Cantilever and Tip Characterization

Although systematic procedures for tip fabrication have been established, there is still some inconsistency in the characteristics of each probe produced. Some of this can

be attributed to inconsistency in the cantilever fabrication process used to produce the commercial AFM cantilevers. The cantilever quality factor (Q) is one particular cantilever property of interest that tends to vary from cantilever to cantilever [16]. In short, the quality factory quantifies the energy loss exhibited by the cantilever during oscillation. Other sources of inconsistency are variability in the magnetic properties of the particles that are manually fixed to the end of the cantilever and damage effects introduced during FIB milling of the particle. All of these issues bring about a need to characterize each fabricated probe before it is used in an MRFM experiment.

Most MRFM experiments are capable of measuring most of the probe characteristics of interest and offer, without a doubt, the best performance when it comes to tip characterization. They also, however, require much more time for setup than alternative methods and are often too expensive to use for the task of characterization, especially when fabrication success rates are low. One of the most useful instruments for characterizing the probe is the room temperature cantilever magnetometer. This instrument is capable of measuring the tip magnetic moment, magnetic hysteresis, coercivity, and overall anisotropy of the particle, as well as resonant frequency and Q of the cantilever [15, 17, 18, 19, 20]. The instrument is also much cheaper, faster to use, and easier to operate than a full-scale MRFM.

1.5 Thesis Layout

Chapter 2 gives an introduction to MRFM, describing some of the basic principles of magnetic resonance and giving a comparison with other prominent microscopic imaging technologies. The basics of mechanical detection of magnetic resonance are covered with emphasis on some of the key aspects relevant to the research presented

in the proceeding chapters. Some practical applications of MRFM are also discussed in order to justify the motivation for this research. Chapter 3 discusses the procedures used to fabricate MRFM probes, namely particle gluing and FIB milling. Key accomplishments and challenges are highlighted, with emphasis on the fabrication of desirable ferromagnetic tips and the documented loss in coercivity resulting from FIB milling. Chapter 4 gives a thorough presentation of the underlying principles of cantilever magnetometry followed by several measurement results and discussions, each representing an important aspect of characterization. Particular emphasis is placed on instrument sensitivity and past and future improvements to the instrument used for this research. Chapter 4 contains many concepts similar to those presented in chapter 2, especially with regard to cantilever behavior. Chapter 4 also serves as a compliment to chapter 3, since characterization is an effective method of evaluating the success of the fabrication efforts discussed in chapter 2. Finally, chapter 5 wraps up the thesis with a short conclusion giving a summary of the accomplishments highlighted and the focus of future related research efforts.

CHAPTER 2

Magnetic Resonance Force Microscopy

2.1 Magnetic Resonance

Magnetic resonance is a condition exhibited by a nuclear or electronic spin system in response to simultaneous static and oscillating external magnetic fields satisfying certain criteria. Every atomic nucleus and electron possesses both a magnetic moment $\boldsymbol{\mu}$ and angular momentum $\boldsymbol{J}$. When a static external field $\boldsymbol{H_0}$ is applied the magnetic moment (spin) will begin to precess around the external field as a result of the magnetic interaction. The picture shown in figure 2.1 represents the relative orientations of the moment and external field and the resulting precession experienced by the moment. This motion is described by the relationship

$$\tau = \boldsymbol{\mu} \times \boldsymbol{H_0} = \frac{d\boldsymbol{J}}{dt} \tag{2.1}$$

where

$$\mu = \gamma \hbar \boldsymbol{J} \tag{2.2}$$

The frequency of precession ω_{rf}, often referred to as the Larmor frequency, will be proportional to both the external field $\boldsymbol{H_0}$ and the gyromagnetic ratio γ according to

$$\omega_{rf} = \gamma \boldsymbol{H} \tag{2.3}$$

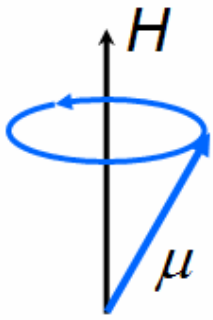

Figure 2.1: Diagram showing the orientation of a magnetic moment (spin) precessing about an external field; taken from [1].

The gyromagnetic ratio γ is a constant of proportionality that is unique for each nuclear moment and considerably different for nuclear and electronic moments. The phenomenon of magnetic resonance occurs when a transverse oscillating magnetic field $\boldsymbol{H_1}$ with frequency $\gamma \boldsymbol{H_0}$ is applied in a direction perpedicular to the static external field $\boldsymbol{H_0}$. Without the oscillating external field the spins are all precessing around the static field, but in a random fashion. Once the oscillating field is applied, the spins satisfying equation 2.1, where ω_{rf} is the frequency of the oscillating field, will begin to precess coherently about the effective field $\boldsymbol{H_{eff}}$ as shown in figure 2.2. This coherent precession is, essentially, the definition of magnetic resonance.

2.1.1 The Rotating Frame of Reference

When trying to understand the physical behavior of resonant spins it is often beneficial to consider them from a rotating frame of reference. This rotating frame can be visualized as a plane that rotates about an axis (usually referred to as the z-axis) parallel to the static external field $\boldsymbol{H_0}$ with a frequency of rotation equal to the

Larmor frequency [21]. In such a frame of reference the oscillating transverse field $\boldsymbol{H_1}$ (usually pictured along the x-axis) will appear static. Figure 2.2 shows the various field components involved and the precession of a magnetic moment about the effective field from the plane of the rotating frame. In this figure there is a magnetic field

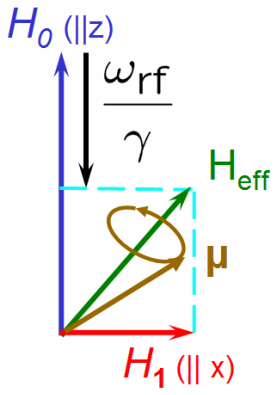

Figure 2.2: Diagram showing the various magnetic field components and spin precession behavior in the plane of the rotating frame of reference; taken from [1]

component along the negative z-direction which subtracts from the static external field. This field does not really exist, but is used to compensate for the effect of visualizing the precessing moment in the rotating frame. This negative static field is introduced because in the rotating frame the transverse field $\boldsymbol{H_1}$ appears static. Thus, in the rotating frame the $\boldsymbol{H_0}$ field is suppressed by an amount determined by equation 2.3, such that for spins experiencing the resonant external field, the effective field H_{eff} is aligned parallel to the tranverse field H_1 in the rotating frame. The effective field, or total field, defines the axis about which the magnetic moment precesses on resonance. In the lab frame of reference this precession about the effective field will

also be combined with a rotation of the effective field (with the rotating frame) about the static external field $\boldsymbol{H_0}$.

2.1.2 Nuclear vs. Electronic Spins

Magnetic resonance experiments can be performed on either nuclear spins or electronic spins. When performed on nuclear spins the term used is nuclear magnetic resonance (NMR). When performed on electronic spins the term used is either electron spin resonance (ESR) or ferromagnetic resonance (FMR), depending on the magnetic properties of the sample involved. ESR refers to resonance in paramagnetic samples while FMR refers to resonance in ferromagnetic samples. Although the basic principles of resonant behavior for nuclear moments and electronic moments are very similar, there are some important differences between the two that should be noted. These differences have major implications for each of the different types of magnetic resonance experiments.

One major difference is that the magnetic moments of nuclear spins are much smaller than an electronic moment. The magnetic moment of a proton, about 1.41×10^{-26} J/T, is over 600 times smaller than an electronic moment, about -928×10^{-26} J/T. The magnetic moment of a neutron is over 900 times smaller than that of an electron. This has a direct and proportional effect on the signal magnitude, but is also largely responsible for the significant difference in the gyromagnetic ratios of nuclear and electronic spins. From equation 2.1 one can see that the torque induced on the magnetic moment is proportional to the moment itself. The frequency of precession, the Larmor frequency, will, for a given external field, increase with the magnitude of the magnetic moment. Equation 2.3 shows that this increase in Larmor frequency is

directly reflected in the gyromagnetic ratio. For this reason, ESR and FMR experiments usually require $\boldsymbol{H_1}$ frequencies in the microwave range (typically 3-10 GHz). NMR, on the other hand, can suffice with RF fields (MHz range) because nuclear spins have a much lower gyromagnetic ratio. FMR experiments typically produce the largest signals because the ferromagnetic interaction between spins results in a much higher spin polarization than spins in a paramagnetic sample can achieve. FMR experiments also, however, present additional challenges because of the interaction of spins throughout the sample.

Because the nuclear composition varies between different elements and even different isotopes of the same element, the gyromagnetic ratios of these different nuclei will also be different. Since the nuclear gyromagnetic ratio is chemically specific, NMR experiments can differentiate between different nuclear spins by their resonant frequencies, allowing the spatial analysis of nuclear composition in a sample.

2.2 Force Detection

Non-inductive detection of magnetic resonance was first proposed by Sidles [8] in 1991 as an ultrasenstive method for investigating micron-scale samples. This proposal suggested that magnetic resonance could be detected by coupling a spin to a micron-scale mechanical oscillator, commonly referred to as a cantilever, through the well known gradient-moment interaction force

$$\boldsymbol{F} = (\boldsymbol{\mu} \cdot \nabla)\boldsymbol{B} \tag{2.4}$$

where $\boldsymbol{B}$ is the magnetic flux density (usually referred to as magnetic field from this point forward, since the distinction between magnetic field $\boldsymbol{H}$ and magnetic flux density $\boldsymbol{B}$ is of little consequence). In general, this is achieved by coupling the spins

(most experiments to date have involved coupling to many spins rather than just a single spin) in the sample to the gradient of a magnetic tip on a cantilever in such a manner that the gradient-generated force on the cantilever changes as a function of position, resulting in a measurable cantilever excitation amplitude or frequency shift. There are several experimental procedures or protocols that can achieve such results, however, a discussion of these is beyond the scope of this thesis. If the proper force coupling is achieved, the cantilever will undergo either a shift in its resonant frequency or oscillations driven at its resonant frequency depending on the experiment. In the case of frequency shift detection, the position dependant force acts as a modification to the spring constant of the cantilever, resulting in a frequency shift described by

$$f_0 + \Delta f = \sqrt{\frac{k + \Delta k}{m}} \tag{2.5}$$

where f_0 is the cantilever resonant frequency, k is the cantilever spring constant, and m is the cantilever mass.

Although the gradient is needed to produce the force interaction between sample and cantilever it also serves another purpose. It produces a non-uniform field defining a thin, bowl-like, 3D slice, called the *sensitive slice*, over which the resonant field condition is satisfied. Only the spins within this resonant slice will effectively couple to the magnetic tip. The higher the gradient from the tip, the thinner this slice and, the higher the achievable resolution, as well as force interaction per spin. It is this feature that allows MRFM to realize both high spatial resolution and 3D subsurface imaging. In addition, by varying an externally applied uniform field, the sensitive slice can be forced to penetrate deeper or shallower into the sample. This dimension of freedom, combined with a mechanical lateral scanning of the tip (usually achieved with piezo-electric actuators), allows a 3D image to be generated using image

deconvolution techiques [10, 11]. Figure 2.3 shows the magnetic field profile from a 1 μm diameter spherical magnetic particle, with a roughly 1000 G sensitive slice shown in black. One can see that for a resonant magnetic field corresponding to a specific

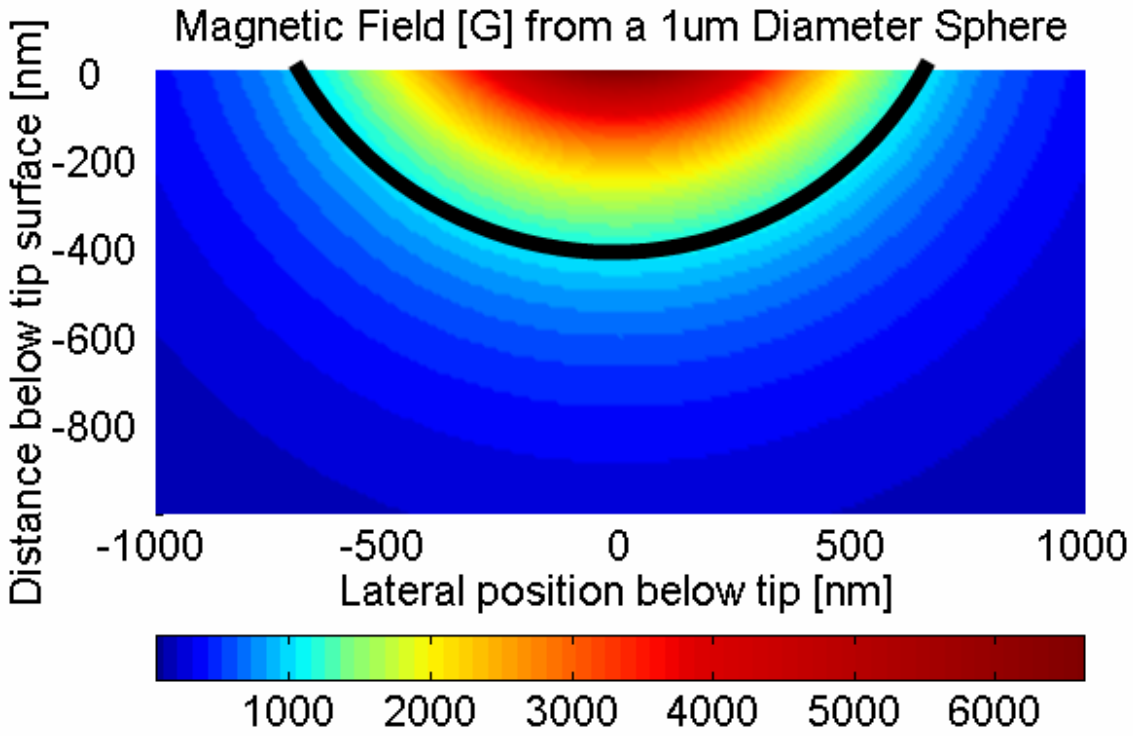

Figure 2.3: Magnetic field profile below a 1 μm diameter spherical magnetic particle with a sensitive slice around 1000 G shown in black. The origin of the axes represents the surface of the spherical tip radially outward from the center along the direction of magnetization.

shade of color there will be a bowl shaped sensitive slice, as visualized by rotating the two dimensional profile about a vertical axis centered laterally in the plot.

2.2.1 Displacement Detection

The position of the cantilever can be detected using a technique called optical interferometry. Optical interferometry uses the interference between light reflected off the end of an optical fiber and light reflected off the surface of the cantilever to measure the position of the cantilever. This tracking of the cantilever position allows information such as cantilever oscillation amplitude, frequency, and phase to be easily calculated. In optical interferometry [22, 23, 24], coherent light is sent through an optical fiber that is positioned perpedicular and in close proximity to the end of the cantilever. When this light reaches the end of the fiber some is reflected back from the end of the fiber and some passes out of the fiber. The portion that passes out of the fiber is then reflected off of the cantilever surface and passes back into the fiber. It will be assumed for simplicity that from this point forward in the discussion the light is completely reflected from the surface of the cantilever closest to the fiber. This is a reasonable approximation for some cantilevers and serves the purpose of this discussion well. The above-mentioned reflection behavior is illustrated in figure 2.4. Note that the relative thicknesses of the fiber cladding, fiber wall, fiber core, and cantilever are not drawn to scale. The light reflected off of the end of the fiber and the light reflected off of the cantilever and back into the fiber are, in general, no longer in phase and interfere, producing a resultant wave that is a superposition of the two separate waves.

With the first light wave described by

$$y_1 = A_1 \sin\left(\frac{2\pi x}{\lambda_a} - \omega t\right) \tag{2.6}$$

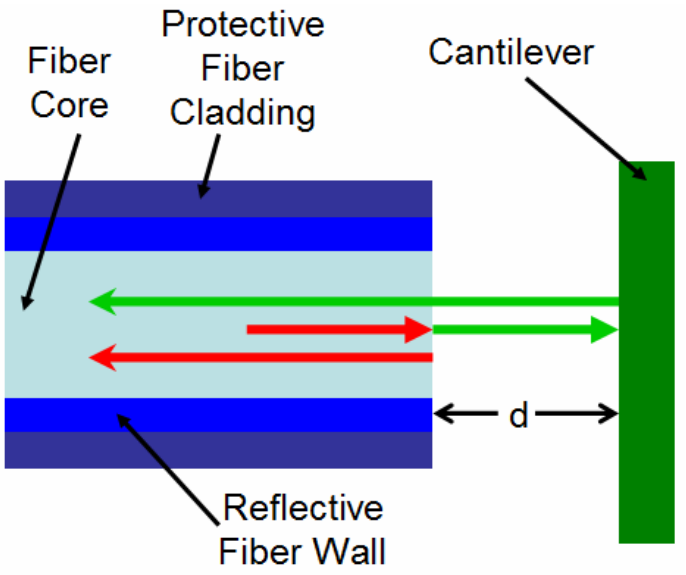

Figure 2.4: Illustration showing the basic inteference principle involved in optical interferometry. The light waves reflected from the end of the fiber and the cantilever travel different paths and are therefore, in general, out of phase resulting in interference. Note that the relative thicknesses of the fiber cladding, fiber wall, fiber core, and cantilever are not drawn to scale.

and the second light wave described by

$$y_2 = A_2 \sin\left(\frac{2\pi x}{\lambda_a} - \omega t + \phi\right) \tag{2.7}$$

where y is the instanteous magnitude, A is the peak amplitude of the wave, x is the position along the fiber, λ_a is the wavelength of the light in the fiber core, ω is the frequency of the light, t is time, and ϕ is the phase difference between the two waves, the resultant wave can be represented as

$$y\prime = A' \sin\left(\frac{2\pi x}{\lambda_a} - \omega t + \phi'\right) \tag{2.8}$$

where A' is the peak amplitude of the resultant wave and ϕ' is the phase of the resultant wave. A' and ϕ' can be determined by adding the phasors representing the

amplitude and phase of each of each of the two original waves resulting in

$$A' = \sqrt{A_2^2 \sin(\phi) + 2A_1A_2\cos(\phi) + A_2^2\cos(\phi)} \tag{2.9}$$

The phase difference ϕ between the two waves is a function of the spacing between the fiber and the cantilever represented by

$$\phi = \frac{4\pi d}{\lambda_b} + P \tag{2.10}$$

where d is the fiber-cantilever spacing, λ_b is the wavelength of light in the medium between the fiber and cantilever (usually near vacuum for a typical experiment), and P is a term accounting for phase shifts introduced to both waves by reflection and transmission between different media.

A block diagram of the entire optical interferometry setup is shown in figure 2.5. The light produced by the laser diode is first fed into an optical fiber and then through

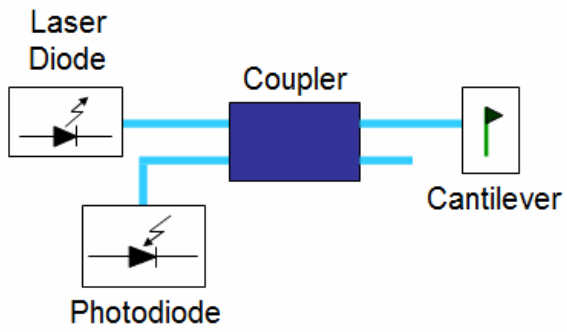

Figure 2.5: Block diagram of the optical interferometry setup used to detect the cantilever position. The laser diode, directional coupler, cantilever, and photodiode are shown.

a directional coupler before falling indicent on the cantilever surface. When the light is reflected back from the cantilever the coupler directs the light through to another

optical fiber that is incident upon a photodiode. It is this photodiode that converts the amplitude of the light to a voltage signal which can be correlated to cantilever position. Since the voltage induced in the photodiode (detector) is proportional to the light intensity rather than amplitude, A'^2 is the quantity that will determine the relationship between voltage and cantilever position. Combining equations 2.9 and 2.10 and simplifying yields

$$V \propto I_v \propto A'^2 = A_1^2 + A_2^2 + 2A_1A_2\cos\left(\frac{4\pi d}{\lambda_b} + P\right) \tag{2.11}$$

where V is the voltage induced in the photodiode (detector) and I_v is the luminous intensity of the resultant light wave. One can now see that this dependence of ϕ on the fiber-cantilever spacing d leads to a sinusoidal dependence of V on d after addition of the two phasors representing the two separate waves. The result is that the light signal reaching the photodiode changes amplitude as the spacing between the fiber and cantilever changes during cantilever oscillation. The first two terms to the right of the equals sign represent a DC offset voltage that will appear at the detector. In order to achieve maximum sensitivity of the voltage to changes in position, the phase difference ϕ should be $\pi/2$. This is equivalent to maximizing the derivative of the cosine function. Since it is difficult to adjust the fiber-cantilever spacing precisely on the scale of λ_b, ϕ is usually adjusted by tuning λ_b via the laser diode temperature. For more details on specific procedures used to calibrate and tune the optical inteferometer see section 4.3.2.

Although other methods of displacement detection such as capacitive and piezoresistive detection have been used occasionally, optical inteferometry is superior in most respects and is the dominant method used in current MRFM experiments. Perhaps

the greatest advantage of optical inteferometry is its extreme sensitivity, with displacement detection resolution as high as 0.01 angstroms. Optical interferometry is also relatively easy to implement. Perhaps the only major disadvantage of this method of displacement detection is the vulnerability of the optical fiber to breakage.

2.2.2 Cantilever Excitation

In order to achieve maximum sensitivity in the force detector (cantilever) it must be driven at or very close to its resonant frequency. This is the frequency at which the cantilever experiences the lowest energy loss per cycle, allowing the signal to be amplified many times. In fact, near resonance, the mechanical oscillator actually acts as an extremely low noise and high gain amplifier. It is this amplification efficiency, unparalleled in the coil detectors used for inductive detection, that makes MRFM so sensitive. In some experiments the cantilever is driven directly by the resonant spins. In others the cantilever is driven by an external device at its resonant frequency through the use of electronic feedback.

The most common method of driving the cantilever into oscillations is through the use of a piezoelectric device. The cantilever must be placed in contact with the piezo directly or through another object. An AC voltage is applied to both electrodes of the piezo causing it to expand and contract at the frequency of the applied voltage. This is equivalent to applying an AC force to the cantilever, which will cause it to oscillate. Various feedback techniques can be utilized to track the resonant frequency as well as modify the effective cantilever parameters through feedback control methods. An alternative method of cantilever excitation is through the use of an electrostatic force resulting from the capacitance between an electrode and the cantilever. The same

control methods can be used with this approach as well. The only difference is that, here, the origin of the force is the electrostatic attraction or repulsion between the cantilever and electrode. It is common when driving the cantilever with an electrostatic force to use a metallic coated cantilever to provide the electrical conductivity needed to establish a voltage at the end of the cantilever.

2.2.3 Force Detectors

There have been many different types of mechanical oscillators used as force detectors. Commercially available AFM cantilevers are commonly used in MRFM experiments because they are economical and easily obtained. Figure 2.6 shows a commercially available silicon nitride (SiN) AFM cantilever chip (Veeco, model # MLCT-NONM) with several different cantilevers. The cantilever marked by the arrow in figure 2.6 is the particular cantilever referred to in the research presented in this thesis whenever a SiN cantilever is mentioned. Figure 2.7 shows a silicon AFM

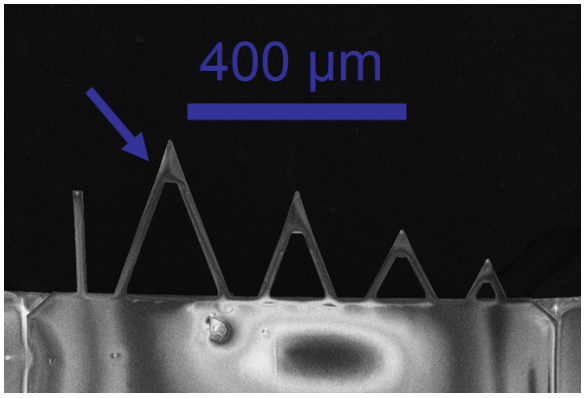

Figure 2.6: SiN AFM cantilever chip supporting several different cantilevers, including both triangular and rectangular cantilevers. This chip (model # MLCT-NONM) is manufactured by Veeco Probes [2]. The blue arrow points to the only SiN cantilever used in the research presented in chapters 3 and 4.

cantilever and chip.

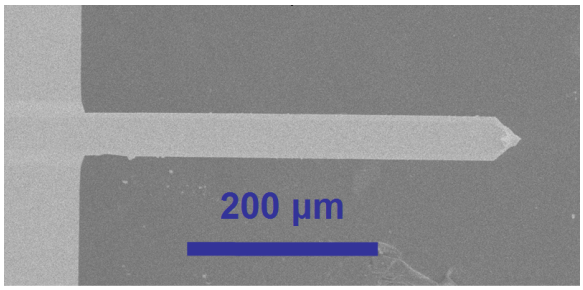

Figure 2.7: Single silicon rectangular AFM Veeco cantilever extending from a chip. This cantilever (model # MPP-32100) is manufactured by Veeco Probes [2].

As progress has been made in the field of MRFM many researchers are opting to fabricate their own cantilevers tailored specifically for performance in MRFM experiments [14, 15, 16, 19, 20], which require much higher sensitivity [14, 15, 24] (lower thermal noise) than AFM cantilevers. Cantilevers with spring constants more than 1000 times smaller than commercially available AFM cantilevers have been fabricated by Stowe et. al. [14]. The cantilevers must also be compatible with the particular displacement detection method used and must contain or be capable of accepting a magnetic tip. The most popular materials used for cantilever fabrication are currently polysilicon, single crystal silicon, and silicon-nitride. Researchers have demonstrated single crystal silicon to be a preferrable candidate due to its low instrinsic mechanical loss [16]. The cantilever material is typically chosen for its compatibility with fabrication methods as well as mechanical properties such as low internal stress, and low intrinsic mechanical loss (high Q) [16]. Higher Q results in higher signal strength and lower noise. Cantilever Q (mechanical quality factor) is one of the most difficult

cantilever parameters to control during fabrication but also one of the most important for high sensitivity. Because there are so many factors that can affect the Q of a cantilever [16], a thorough treatment will be too extensive for this paper. For a summary of the properties of three cantilevers used for MRFM experiments in our research group see table 4.2.4 in section 4.2.4. Also, table 4.3.3 in section 4.3.3 shows the measured quality factors and resonant frequencies of a sample of 6 Veeco silicon cantilevers (model # MPP-32100), the same model shown in figure 2.7. Sections 2.2.5 and 4.3.3 discuss cantilever quality factor in more detail.

2.2.4 Experimental Layout

Figure 2.8 shows a diagram of the layout of a typical MRFM experiment in the "horizontal" cantilever geometry, in which the cantilever length is parallel to the sample surface . One can see that a gradient producing magnetic tip is fixed to the end of an AFM cantilever. This non-uniform magnetic field is supplemented by a static uniform external field that together define a sensitive slice over which the resonant field condition is met. The spins in this bowl-shaped slice are being driven into resonance by an oscillating transverse magnetic field generated from a small coil. These spins are manipulated using specialized techniques in such a manner as to produce a force on the cantilever measurable through a change in either its vibration amplitude or resonant frequency. In the experiment in figure 2.8 fiber optic interferometry is used for displacement detection and one can see that the fiber is positioned perpendicular to the end of the cantilever.

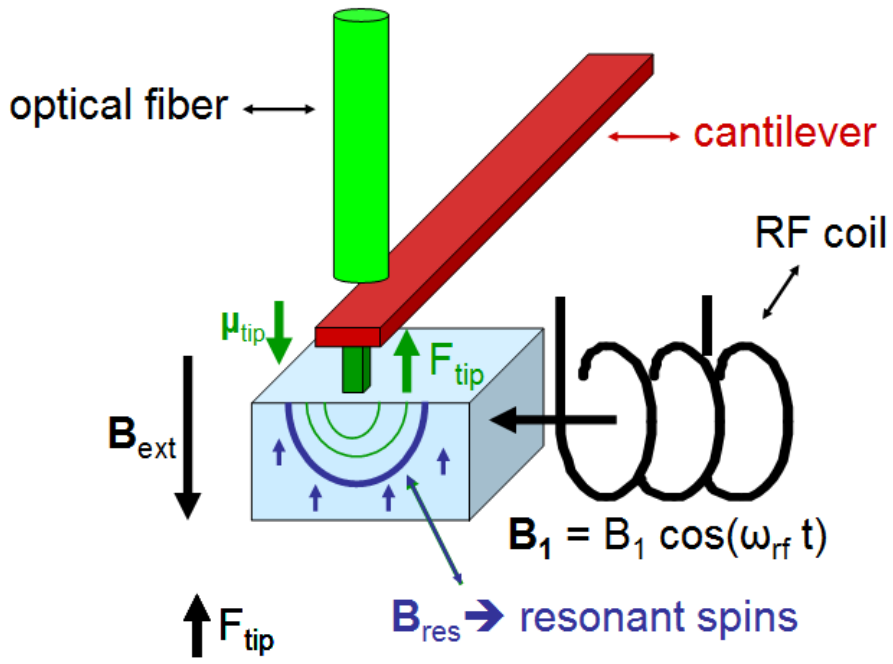

Figure 2.8: MRFM experimental layout for the horizontal cantilever geometry.

In the horizontal cantilever geometry of figure 2.8 the coupling force [5] shown in equation 2.1 reduces to

$$\boldsymbol{F_z} = M_z \frac{\partial B_z}{\partial z} \hat{z} \tag{2.12}$$

because the cantilever is oscillating in the z-direction and is only sensitive to forces which act in this direction. In equation 2.12 M_z is the magnetization of the interacting spins and B_z is the z-component of the magnetic field in the region of the spins. Figure 2.9 shows the z-gradient ($\partial B_z/\partial x$) profile below a 1 μm spherical magnetic tip. One can see that the shape of this profile similar to that of the overall field from a spherical tip (shown in figure 2.3) such that the z-gradient is fairly constant throughout the sensitive slice. One might also note that the strongest force interaction between

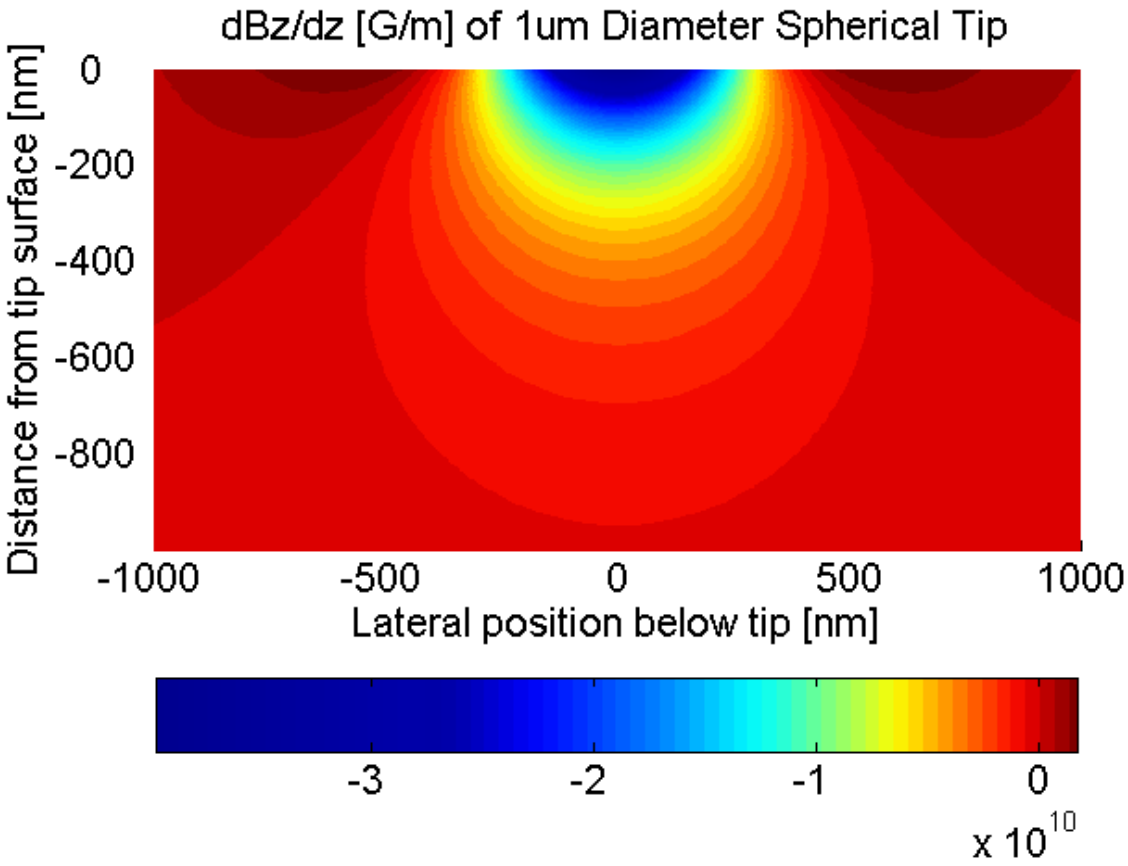

Figure 2.9: $\partial B_z/\partial z$ magnetic field gradient profile below a 1 μm diameter spherical magnetic particle. The origin of the axes represents the surface of the tip radially outward from the center of the tip along the direction of magnetization.

magnetic tip and spins occur when the sensitive slice is positioned very close to the tip where the z-gradient is strongest.

Figure 2.10 shows the "vertical" cantilever experimental geometry, an alternative MRFM experimental geometry that is becoming more widely used and will probably be the only viable option for achieving single nuclear spin sensitivity. In the vertical geometry the cantilever is positioned perpendicular to the sample surface and oscillates parallel to the sample surface. The magnetization of the tip, however, is still

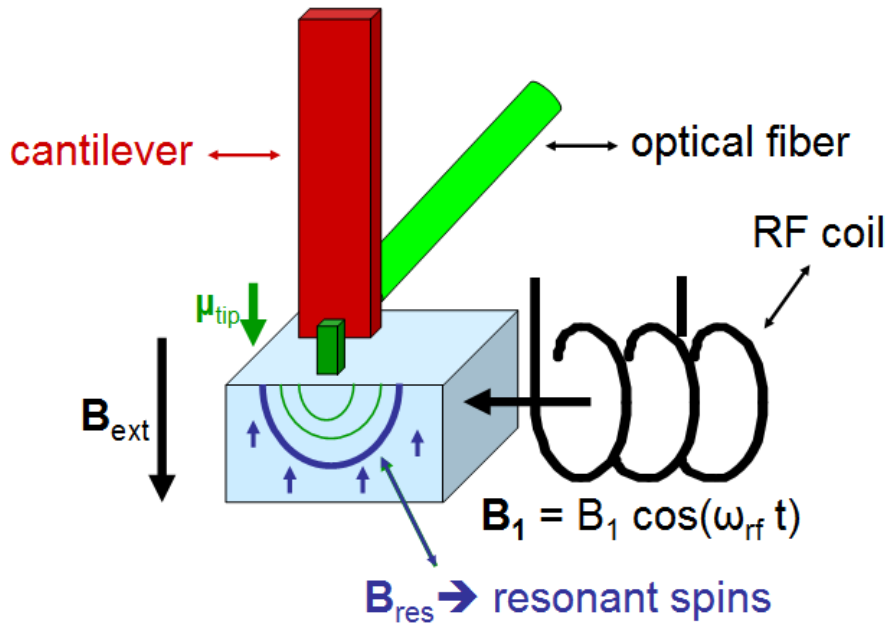

Figure 2.10: MRFM experiment in the vertical cantilever geometry.

perpendicular to the sample. One of the main advantages of this geometry is that the cantilever can be brought much closer to the sample surface without Van-Der-Wal's or electrostatic forces causing cantilever snap-down to the sample surface [13, 14]. In the horizontal geometry snap-down can occur as far away as 500 nm for the soft (low spring contant) cantilevers needed for high sensitivity (see section 2.2.5). Using the vertical geometry in figure 2.10, however, sample tip spacings closer than 10 nm can be achieved before snap-down occurs [14], as long as the accuracy of the cantilever alignment with the surface of the sample is high enough. This close-range probing of the sample exposes the resonant spins to the much higher gradients which occur closer to the cantilever's magnetic tip, resulting in a much higher force. In the vertical geometry the simplified version of equation 2.1 is slightly different than equation

2.12. The new cantilever-spin interaction force for the vertical cantilever geometry is

$$\boldsymbol{F_x} = M_z \frac{\partial B_z}{\partial x} \hat{x} \tag{2.13}$$

Here the magnetic field gradient in the x-direction determines the position-dependent force, since this is the direction of oscillation experienced by the cantilever. This gradient presents some unique phenomenon in MRFM experiments that aren't encountered in the horizontal geometry. One is that the probe interacts more strongly with spins at the edges (to the sides) of the probe. This is because the x-gradient ($\partial B_z/\partial x$) is zero directly beneath the tip and peaks somewhere laterally distant from the center of the tip. A two dimensional plot of the x-gradient profile below a 1 μm diameter spherical magnetic tip is shown in figure 2.11. In addition, one might notice that the sign of the magnetic field gradient is different at opposite sides of the particle. This means that the sign of the force produced is also different, such that much of the force produced by the sensitive slice on one side of the particle is cancelled out by the force produced on the other side. Experiments in this cantilever geometry are, therefore, only able to detect differences in the spin density or spin polarization (which varies statistically) on each side of the magnetic tip.

In early MRFM experiments [9, 10, 11] the sample was placed on the cantilever and the gradient producing magnetic probe was mounted in a stationary position. The "magnetic tip on cantilever" configuration [5] in figures 2.8 and 2.10, however, gained popularity for a couple of reasons. The first is its practicality in scanning the probe over a sample surface to produce an image. The sample can be mounted seperately from the cantilever allowing several different samples to be explored with the same cantilever. The second is that the much larger mass loading resulting from placing a sample on the cantilever instead of a smaller magnetic tip decreases both the

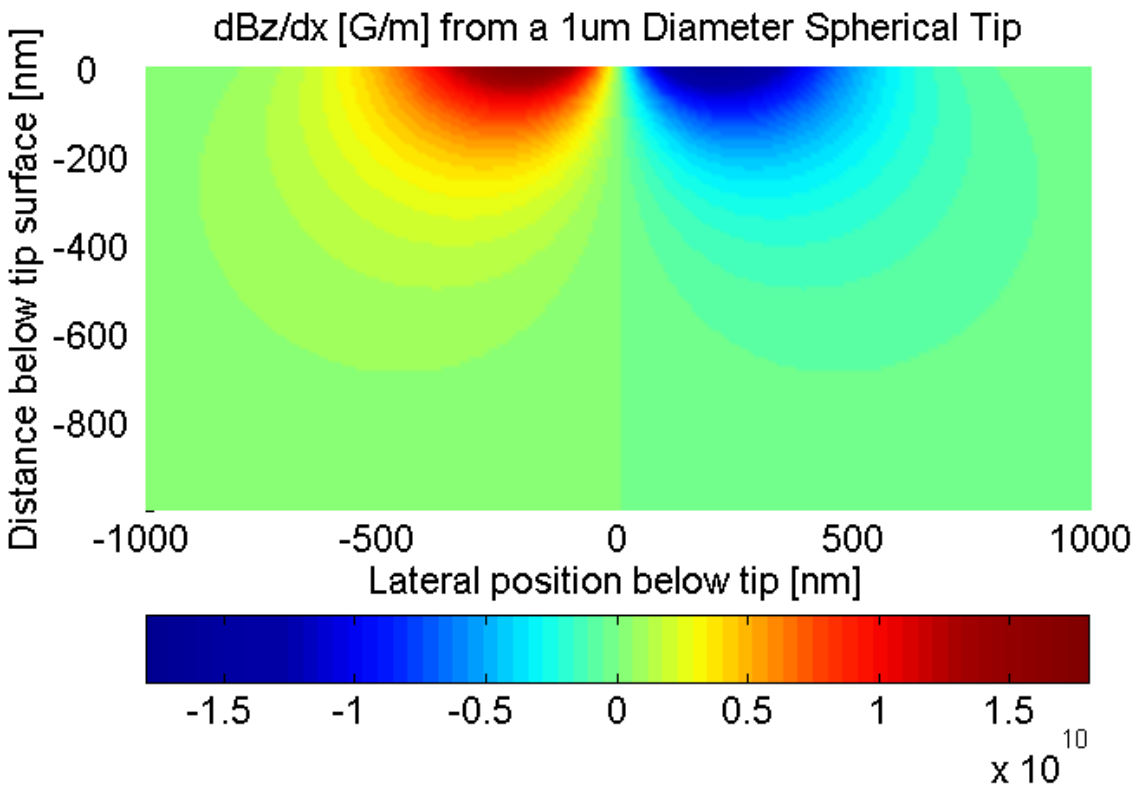

Figure 2.11: $\partial B_z/\partial x$ magnetic field gradient profile below a 1 μm diameter spherical magnetic particle. The origin of the axes represents the surface of the tip radially outward from the center of the tip in the direction of magnetization.

Q and frequency of the cantilever. As described in section 2.2.5, this has a detrimental effect on the signal-to-noise ratio. Some of the most recent and successful NMR force microscopy studies [25, 26], however, have suggested that the sample on cantilever configuration may, in fact, be the optimal setup, especially for small samples, where cantilever mass loading is not a factor. One of the suggested advantages of the sample on cantilever configuration is reduced magnetic damping that occurs when the magnetization of the gradient-producing tip oscillates in the high external fields

required for NMR. This magnetic damping acts to effectively lower the Q of the cantilever and reduce sensitivity.

2.2.5 Sensitivity and Resolution

MRFM owes its very high sensitivity to the use of micron-scale mechanical oscillators which act as signal detectors. These cantilevers are essentially extremely low noise and high gain pre-amplifiers which convert the magnetic force between tip and sample into a measurable cantilever displacement signal. The high gain provided by the cantilever is achieved by coupling the signal to the cantilever at its resonant frequency [10, 14, 15, 24]. On resonance, the vibration amplitude of the cantilever can be described by

$$z = F_z \frac{Q}{k} \tag{2.14}$$

where z is the cantilever vibration amplitude, Q is the cantilever mechanical quality factor, k is the cantilever spring constant, and F_z is the z-component of the force (parallel to the cantilever thickness) between the cantilever's magnetic tip and the resonant spins excited in the sample. The mechanical quality factor of the cantilever is an emperically determined value that is inversely related to the intrinsic mechanical energy loss experienced by the cantilever during each cycle of oscillation. The Q of a cantilever can be considered as the gain it provides to the force signal. With typical MRFM cantilever quality factors ranging from 500 to as high as 200,000 [10, 14, 15, 16, 19, 20, 24, 27] there is the potential for extremely sensitive detection. This makes Q one of the more important cantilever parameters. It should be noted that experimental conditions such as pressure and temperature can have a major impact on cantilever Q [16], and the typical range of values mentioned above were certainly

not all measured under the same experimental conditions. Typically, lower pressures and temperatures result in an increased Q [16], one of main reasons many MRFM experiments are peformed at or below 4 K in vacuum. Quality factor may increase by as much as 2-5 times its value at room temperature when temperature is decreased to several K [16, 27]. Q has an even stronger dependence on pressure, increasing several orders of magnitude from atmospheric pressure to sub-milliTorr pressures. Below about 1 mTorr, however, quality factor becomes relatively independent of pressure [16]. Cantilever quality factor is also discussed in section 4.3.3.

The obvious compliment to cantilever signal strength is cantilever noise. The thermomechanical cantilever vibrations are the current noise barrier in MRFM experiments [14], well above the noise level of the interferometric displacement detectors used. The force noise spectral density of the cantilever [14, 16, 19], also discussed in section 4.2.4 is given by

$$S_F^{1/2} = \sqrt{\frac{2kk_BT}{\pi Q f_0}} \tag{2.15}$$

where $S_F^{1/2}$ is the force noise spectral density, k_BT is the thermal energy, and f_0 is the cantilever resonant frequency. In a bandwidth $\Delta\nu$, the resulting RMS force noise [14, 16, 19] is given by

$$F_n = \sqrt{\frac{2kk_BT\Delta\nu}{\pi Q f_0}} \tag{2.16}$$

Assuming a unity signal-to-noise ratio, the minimum detectable moment is given by

$$\mu_{min} = \frac{1}{g}\left(\frac{4kk_BT\Delta\nu}{\pi Q f_0}\right)^{1/2} \tag{2.17}$$

where g is the magnetic field gradient.

Cantilever resonant frequency is related to cantilever spring constant according to

$$f_0 = \sqrt{\frac{k}{m}} \tag{2.18}$$

which to applies to any simple harmonic oscillator, where m is the effective mass load of the oscillator, i.e. the equivalent mass placed on the end of the cantilever that would produce the same resonant frequency as the actual mass distribution along its length. To decouple the relationship between cantilever mechanical parameters (f_0 and k) and μ_{min} it is useful to express the resonant frequency of the cantilever in terms of spring constant and mass. Spring constant can be expressed in terms of cantilever physical parameters as

$$k = \frac{Et^3w}{4l^3} \tag{2.19}$$

for a beam cantilever, where E is Young's modulus of elasticity and l, w, and t are the cantilever length, width, and thickness, respectively. Cantilever effective mass m can be approximated as

$$m = \rho lwt \tag{2.20}$$

for a rectangular cantilever, where ρ is mass density of the cantilever material. Equation 2.20 is a simplification based on the actual mass of the cantilever and will undoubtedly introduce some error into the calculation but, nevertheless, should provide some first-order insight into sensitivity maximization. Substituting equations 2.18, 2.19, and 2.20 into equation 2.16 yields the RMS force noise

$$F_n = \left(\frac{wt^2k_BT\Delta\nu}{lQ}\right)^{1/2}(E\rho)^{1/2} \tag{2.21}$$

Again, assuming a unit signal-to-noise ratio is required for detection, the minimum detectable moment (of resonant spins in the sample) is given by

$$\mu_{min} = \frac{1}{g}\left(\frac{2wt^2k_BT\Delta\nu}{lQ}\right)^{1/2}(E\rho)^{1/2} \tag{2.22}$$

in terms of basic physical cantilever parameters.

From the above equations it becomes clear that for the best signal-to-noise ratio a long, narrow, and thin cantilever with high Q is required. The most sensitive parameter is the cantilever thickness. Some researchers [24] have already succeeded in fabricating cantilevers as thin as 50nm. Unfortunately, it has proven difficult to maintain high Q values as cantilever thickness is decreased [14, 16]. The fabrication of cantilevers with thermal noise limits as low as 0.82 fN (1 fN = 10^{-18} N) has already been achieved [14].

The resolution achievable in MRFM is mainly dependant upon two factors. The first is the magnetic field gradient produced by the cantilever tip. This gradient defines the length scale (distance from the actual infinitesimally thick sensitive slice) over which the transverse field loses its resonance effect on the spins. Higher gradients also produce higher force signals so it is a major goal in current MRFM research to produce tips with higher gradients. More will be discussed on this in chapter 3. The second factor influencing achievable resolution is the cantilever oscillation amplitude, since spins over the entire distance of sensitive slice oscillation contribute to the signal.

Although current sensitivity limits in MRFM are still far from the predicted single nuclear spin sensitivity there has, nonetheless, been significant progress in the last 15 years. ESR experiments have now demonstrated single electron spin sensitivity with 25 nm spatial resolution [13]. NMR experiments have achieved a sensitivity of about 1200 nuclear spins with 90 nm spatial resolution [26]. It has been asserted in [25] that in order to achieve single nuclear spin sensitivity, technological developments enabling size reduction in many of the most important elements of the experimental apparatus will have to be made. This includes both the radio frequency (in the case

of NMR) magnetic field source (traditionally a coil, although a thin wire was proven very effective in [25]) and magnetic field gradient source (magnetic probe tip).

2.3 Comparison with Other Imaging Technologies

What distinguishes MRFM from other imaging technologies is the combination of both high sensitivity and high 3D resolution, with the capability to probe samples far beneath the surface in a noninvasive manner. MRFM achieves its 3D imaging capability by probing spins at a finite and controllable distance from a magnetic tipped probe. The realization of single electron spin sensitivity [13] and promise of nuclear spin sensitivity result from the use of low thermal noise micro-scale mechanical oscillators, commonly referred to as cantilevers.

Conventional magnetic resonance imaging (MRI) via inductive detection is one popular and very successful imaging technology that is capable of 3D imaging. Conventional MRI is a well-established field with many fruitful commercial applications including the MRI used extensively in the medical field to produce 3D images of human tissue. Although inductive detection of magnetic resonance has revolutionized many fields of science, it still has some limitations and drawbacks. One of the major disadvantages is the sensitivity limitation that originates from the inherent resistive shot noise (or Johnson noise) produced in the detection coils. The resonant spins in the sample interact directly with these coils, inducing a voltage at the frequency of the magnetic resonance. As spatial resolution is increased by increasing the magnetic field gradient of the external field, which defines a thinner resonant slice (smaller resonant volume), signal strength is decreased. It is important to note that the resolution in inductive magnetic resonance imaging is not limited by the field gradient needed

to bring sufficiently small portions of a sample into resonance but rather the ability to detect the signal from such small volumes. According to [13], as of 2004, inductive detection imaging techniques require volume elements containing at least 10^12 nuclear spins or 10^7 electronic spins in order to establish a measureable signal. This limits the spatial resolution of conventional MRI to roughly 10 μm [12, 5]. Magnetic resonance force microscopy (MRFM), however, has already achieved single electronic spin detection with 25nm single dimension spatial resolution[13].

Most scanned probe imaging methods see a steady signal strenth increase as tip-sample spacing decreases, making only local (surface) probing of the sample possible. In STM, for example, the probe interacts with the sample via tunneling currents which are a function of the density of states in the sample [12]. This tunneling phenomenon not only requires conductive samples but also only occurs on an angstrom scale [1] so probing atoms below the surface is virtually impossible. Atomic force microscopy has a similar drawback. AFM detects Pauli-repulsion, Van-der-wal's, and Lennard-Jones interaction forces. Although non-contact mode AFM, mostly dependant on Van-der-wals forces, can operate with tip-sample spacings well into the nanometer range it is still not capable of effectively probing atoms beneath the surface. The reason is that the interaction force falls off quickly with distance so that those atoms which are closest to the probe will (aside from shielding second layer atoms) produces forces that dominate any forces generated by second layer atoms. Magnetic force microscopy (MFM), like MRFM, also detects a magnetic dipolar interaction force, however, the strength of interaction is, again, inversely proportional to distance and since all spins in the sample interact with the probe (unlike in MRFM) it too is limited to surface investigation for the same reasons as AFM and STM. Scanning

capacitance microscopy (SCM) and scanning electron micrscopy (SEM) are two other imaging methods that are limited to surface investigations.

2.4 Potential Applications

One of the most significant potential applications of MRFM is imaging of the molecular structure of biological molecules [8, 12]. This would potentially include such structures as DNA sequences and protein molecules. There already exhist other methods of determining such structures, however, these procedures sometimes take months or years to finish and often signficant obstacles related to chemical purification arise for certain molecules [12]. The combination of such challenges with the immense number of different molecules that are still not structurally characterized creates a huge need for a more efficient method of structural determination. With theoretically feasible improvements in sensitivity and resolution [8] MRFM may be able to fulfill such a need. NMR force microscopy has already proven successful in the imaging of isolated single liposomes [4], an early sign of its value in the field of biology.

The imaging capabilities of MRFM that make it so applicable to the field of biology can be readily applied to the imaging of any number of materials including steels, semiconductors, and magnetic storage devices. Although there are already many other imaging technologies (Transmission Electronic Microscopy, SPM, AFM) that have been used to characterized such materials on the atomic level, none have the ability to probe subsurface defects and interfaces. Such investigation would be very helpful for the semiconductor and magnetic storage device industries. One example of a specific use of the MRFM would be the study of magnetic multi-layer systems displaying giant magnetoresistance [5]. The 3D imaging capability allows properties

beneath several layers to be studied, and the microscopic resolution allows site-specific investigation, as opposed to conventional (inductively detected) FMR which can only study sample-averaged properties.

One final potential application for MRFM discussed here is in the manipulation and detection of nuclear spins states in a quantum computer [7]. This quantum computer would store information in two-qubit quantum logic gates via nuclear spin states. The states would be both manipulated and detected (written and read, respectively) using a typical MRFM cantilever probe. Although this realization would first require single nuclear spin sensivitiy, which faces many technical challenges, the construction of such a device would represent a major technological breakthrough in computing, due to the increased data storage density that could be achieved.

CHAPTER 3

Probe Tip Fabrication

3.1 Overview

In MRFM micron-scale mechanical oscillators, often referred to as cantilevers, are used to detect the force between resonant spins in a sample and a magnetic tip fixed to the end of the cantilever. This combination of cantilever and magnetic tip, which will be referred to as the MRFM probe, is, as described in chapter 2, responsible for the high sensitivity and resolution of the MRFM. This high sensitivity is achieved through the use of a low thermal noise cantilever and high gradient magnetic tip. Because the sensitivity and performance of the microscope is so dependent upon cantilever and magnetic tip properties, probe design and fabrication is a critical aspect of current MRFM experimentation [14, 15, 20, 16, 19, 24].

MRFM researchers are now experimenting with the use of custom fabricated, high Q mechanical oscillators (cantilevers) [14, 15, 16]. This of course, opens up many options for cantilever shape, size, and material, with the ultimate goal of reducing thermal noise and, therefore, increasing force sensitivity. As descriped in chapter 2, this essentially amounts to producing long, thin, and narrow cantilevers with high

Q. The approach taken in this research, however, has relied upon the use of commercially available AFM cantilevers. As a result, the main focus of these fabrication efforts have been on the magnetic tip at the end of the cantilever. While the goal of cantilever fabrication is maximum force sensitivity, the main focus of tip fabrication is on maximizing the tip magnetic field gradient and subsequently the tip-sample magnetic gradient-dipole interaction force. The remainder of this chapter will discuss specific tip fabrication objectives, procedures, and results.

3.2 Probe Materials Selection

Most force microscopy cantilevers (MFM, AFM, EFM) are fabricated from either silicon or silicon nitride [2]. MRFM experiments typically make use of the same materials for cantilevers including both poly-silicon (used more frequently in early experiments) and single crystal silicon [14, 15, 16]. The two types of cantilever materials used in the research presented later in this thesis are Phosphorus (n) doped single crystal silicon and amorphous silicon nitride. The single crystal silicon cantilevers tend to have higher quality factors becuase the ordered crystalline structure experiences less instrinsic mechanical energy loss during oscillation than an amorphous structure. More details on cantilever material selection can be found in section 2.2.3.

There are several factors that play into the choice of material for use in the magnetic tip on the cantilever. The first is remanent magnetization. Remanent magnetiztion provides a measure of the magnetization of the particle after the particle has been saturated and the external field removed. The magnetic field gradient is proportional to magnetization so an increase in magnetization ultimately increases resolution and sensitive. Another consideration is tha ease of fabrication. Two other

important factors are coercivity (switching field) and effective anisotropy (overall particle anisotropy), which are different, but related properties. Stricly speaking, both properties are related to each other through the magnetocrystalline anistropy of the various magnetic phases in the particle. In general, coercivity (switching field) has a positive correlation with (effective) anisotropy field. The relationship, however, is a complex function of the microstructure, shape, and the particular magnetization process of the particle [28, 29, 30]. Although soft (low switching and anisotropy field) magnetic materials such as cobalt, nickel, and permalloy are viable candidates for some MRFM experiments, there are a couple reasons why these materials may not be preferred, especially for MRFM on electron spins. One reason is that, often, it is necessary to apply a strong uniform external bias field in the opposite direction to the tip magnetization in order to position the sensitive slice closer to the tip where magnetic field gradients are higher. Close to the tip the magnetic field is also much higher. In ESR or FMR, Larmor frequencies, according to equation 2.3, extend into the GHz range for even moderate tip fields. Often the application of such high frequency fields poses many experimental challenges. It may become necessary to apply a bias (static) field that opposes the tip field and, therefore, reduces its magnitude along with the Larmor frequency. Also, in FMR experiments, it is often necessary to apply a reversal field to localize the FMR mode. Soft magnetic particles will not maintain their magnetization direction under these reverse bias fields and will switch their field polarization, defeating the initial purpose of applying the bias field.

Another advantage of high anistropy particles is that they are less susceptible to magnetic field fluctuations [19, 31]. Thermal field fluctuations in the cantilever tip are the first concern. These fluctuations can induce spin relaxation in the sample,

impeding MRFM experiments [19, 31]. The second concern is small angle fluctuations of the tip magnetic moment, which cause by oscillatory tilting of the tip in the external field. These fluctuations also result in magnetic energy dissipation, effectively lowering the Q of the cantilever [19].

High anisotropy is also preferred for MRFM on electron spins because it reduces the so called "spurious coupling" between the magnetic tip and various applied fields necessary for experiments [5]. Soft magnetic fields exhibit a magnetization that can change drastically with changes in external field. This would include the oscillating microwave field or the static bias field, which is often swept to scan an image in the z-direction (vertical direction). Although high coercivity particles may be beneficial in these respects for ESR at least one group of researchers [20] found that lower anisotropy/coercivity particles were preferred for NMR because the coupling of the thermomagnetic field fluctuations with the lower Larmor frequency of the nuclear spins was actually lower in low anistropy/coercivity particles.

Rare earth magnets are the most suitable candidates for high coercivity and anisotropy particles. Praseodymium iron boron ($Pr_{12}Fe_{14}B$), neodymium iron boron ($Nd_2Fe_{14}B$), and samarium cobalt (Sm_2Co_{17} and $SmCo_5$) are three rare-earth magnets that have been used in MRFM experiments. The research presented here incorporated the use of both $Nd_2Fe_{14}B$ and Sm_2Co_{17} for cantilever tips. Both materials are very comparable and can achieve remanent magnetizations above 1T and coercive fields above 800 kA/m ($\approx 1T/\mu_0$) in bulk samples. In general, $Nd_2Fe_{14}B$ has a slightly higher remanent magnetization and coercive field while Sm_2Co_{17} has a higher Curie temperature and is less susceptible to oxidation [32, 33]. Oxidation is a legitimate concern when dealing with micron scale magnetic particles, since even thin layers of

oxidation can become a significant portion of the overall particle volume. It should be noted that there are a variety of grades of Sm_2Co_{17} and $Nd_2Fe_{14}B$ [32, 33] with varying magnetic properties. In addition, the bulk properties do not always hold for micron-scale particles [5]. In fact, it is often a matter of trial and error to find a particle with acceptable properties, let alone properties that are characteristic of bulk samples. The results presented in chapter 4 give several supporting examples of this.

3.3 Manual Particle Gluing

In order to fabricate a probe with a coercive magnetic tip it is first necessary to attach a particle displaying such properties to the end of the cantilever. Some commercial MFM cantilevers are available with a layer of low-coercivity magnetic material already deposited onto a sharp tip. Some researchers use their own deposition techniques [15, 19, 20] to apply magnetic tips onto cantilevers. These methods have there merits, but so far this approach is only capable of producing magnetically soft (low coercivity) tips.

The approach used here for tip fabrication first requires manually gluing a micron scale ferromagnetic particle to the end of a commercial AFM cantilever. This process is conducted under a powerful optical microscope with an optical resolution slightly less than 1 micron, which sets the size limit of particles that can be glued. A particle must first be selected from a collection of powdered ferromagnetic particles. Filings from larger bulk magnets can also be used for particle selection. The $Nd_2Fe_{14}B$ particles used here have a characteristic spherical shape, as can be seen in figures 3.1 and 3.2, while the Sm_2Co_{17} particles used here have no regular shape. A characteristic

Sm_2Co_{17} particle is shown in figure 3.3. The irregular shape makes it difficult to distinguish a Sm_2Co_{17} particle from a stray non-magnetic particle that has made its way into the collection.

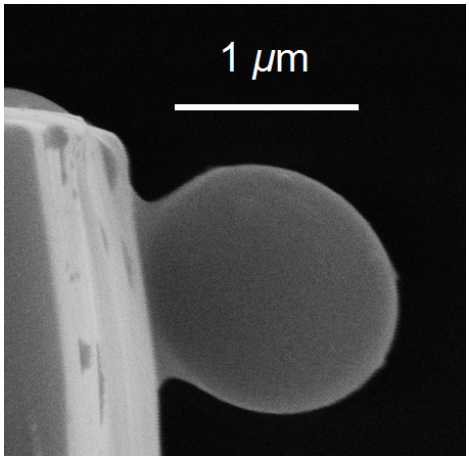

Figure 3.1: SEM micrograph of a micron sized spherical $Nd_2Fe_{14}B$ particle glued on a rectangular silicon cantilever (Veeco, model # MPP-32100). The image shows some distortion probably caused by electrostatic charging during SEM imaging.

Once a particle is selected it must be lifted off of a glass slide using a sharp glass needle and a mechanical micromanipulator. Prior to implementing the use of a glass needle, human eyelashes (as small as several microns wide at the tip) were used to pick up the magnetic particles. The much larger size of the eyelashes made it difficult to pick up particles smaller than several microns. Figure 3.4 shows a human eyelash and a glass needle, both beside a triangular silicon nitride cantilever. The glass needle currently used is produced by heating a pyrex glass rod and drawing the two ends apart using a glass puller, resulting in two sharp-tipped pieces, each with a tip radius of less than 1 micron. A commercially available machine, the model # PC-10

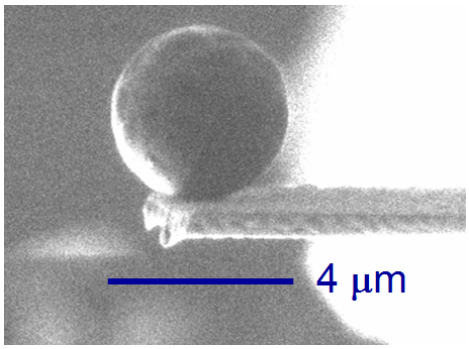

Figure 3.2: SEM micrograph of a spherical $Nd_2Fe_{14}B$ particle glued on a silicon cantilever (Veeco, model # MPP-32100

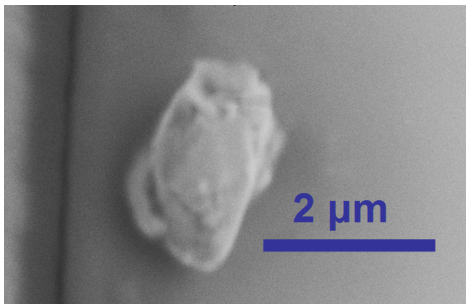

Figure 3.3: SEM micrograph of a Sm_2Co_{17} particle glued on a SiN cantilever (Veeco, model # MLCT-NONM)

manufactured by Narishige, performs this process. Figure 3.5 shows a microscope image of a glass needle beside the same type of cantilever shown in figure 3.4. The glass needle has a small Sm_2Co_{17} particle at the end and the cantilever has a drop of epoxy placed on its free end. The glass needles used to manipulate particles are traditonally used to lift TEM slices from a sample after slice preperation using a focused ion beam (discussed in section 3.4).

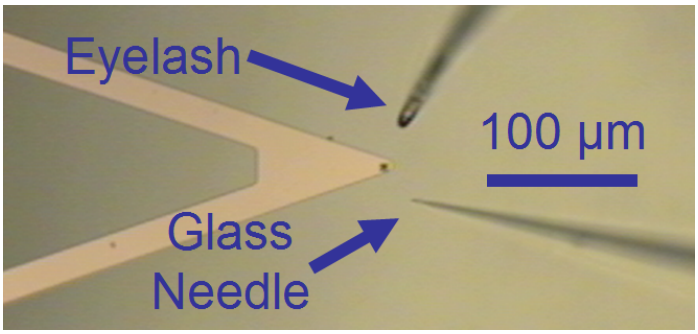

Figure 3.4: Microscope image of a human eyelash (initially used to manipulate micron scale magnetic particles) beside a SiN cantilever and a glass needle (currently the preferred method for manipulating micron scale magnetic particles due to its smaller tip radius).

The goal after particle selection is for the particle to stick to the glass needle via electrostatic forces, however, there are usually more failed attempts than successful ones. One source of difficulty is that, for the Sm_2Co_{17} particles used here, the collection of particles is placed over a permanent magnet during selection to verify that a particle is magnetic. After the particle has been lifted off by the needle, the needle is moved to the edge of the magnet where the magnetic field changes direction. If the particle on the needle is observed to move as the needle is moved back and forth across the edge of the magnet it can be positively identified as a magnetic particle. The drawback to this approach is that, often, the magnetic force on the particle prevents it from attaching electrostatically to the needle. The spherical shape of the $Nd_2Fe_{14}B$ particles used here makes the use of a permanent magnetic unneccesary during gluing since there is a much smaller probability of selecting a non-magnetic (foreign) particle that has the characteristic spherical shape. After a particle has been lifted off the glass slide by the needle it is placed on a small drop of epoxy that

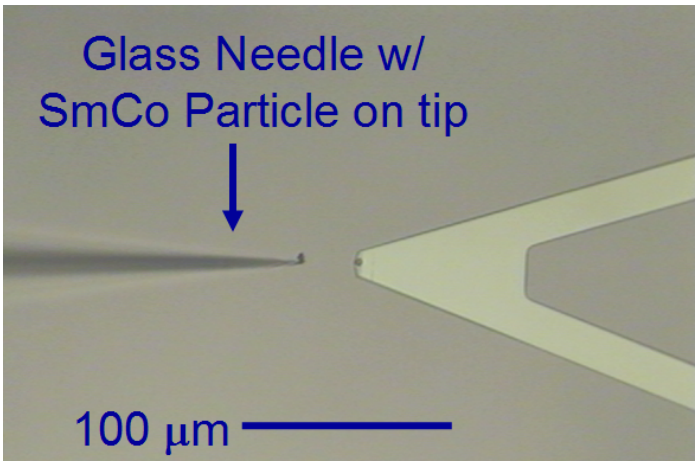

Figure 3.5: Optical microscope image of a glass needle used for gluing magnetic particles. A Sm_2Co_{17} particle is held to the end of the needle via electrostatic forces. The SiN cantilever shown in the image (same type of cantilever shown in figure 3.4) has a small drop of epoxy visible at the end

has already been transferred to the cantilever. The epoxy is transferred using glass needles as well, although needles with broken tips are preferred, because the epoxy tends to be drawn up the needle and away from the tip when very sharp glass needles are used. The two epoxies used for this purpose are Gatan G1 and Stycast®1266 epoxies.

After the particle has been successfully deposited onto the cantilever and the epoxy is given time to dry, the cantilever is placed in a strong ($\sim$9 T) magnetic field while the epoxy dries. This helps to ensure that the easy axis of magnetization (magnetic anisotropy axis) is aligned in the desired direction. This can be either parallel to the length of the cantilever or perpendicular to the surface of the cantilever, depending on the MRFM experimental geometry. One of the drawbacks of $Nd_2Fe_{14}B$ particles is that, because of their spherical shape, they have no shape anistropy. The only contribution to anistropy is from the orientation of the crystalline anistropy axis.

When selecting Samarium Cobalt particles, on the other hand, a particle with a slightly elongated shape can be selected with the hope that it has a much larger overall (effective) magnetic anistropy. This provides an increased rotational force acting to align the particle's easy axis of magnetization with the magnetic field from the permanent magnetic during the drying process. Detailed discussions on magnetic anistropy can be found in sections 4.2.3 and 4.3.7.

3.4 Focused Ion Beam Shaping

In some cases the particle glued on the cantilever will already be of a desirable shape and size. If, however, the particle is too large (which is often the case since it is very difficult to glue particles less than 1 um) or the particle has an irregular or undesirable shape it may be necessary to mill the particle to the size and shape that is desired. This is accomplished through the use of a focused ion beam (FIB) milling tool. For the research presented here the DB235 dual beam instrument from FEI was used. This instrument houses a focused ion beam as well as a scanning electron microscope (SEM).

3.4.1 Focused Ion Beam Instrument Description

The FIB is an instrument that generates a focused beam of gallium ions by accellerating the ions through an electric field. The DB235 is able to produce ion beam energies of either 10 or 30 keV, focused to a spot size as small as several nanometers using magnetic lenses. This beam can then be raster-scanned across the surface of a sample to achieve a variety of objectives. One application of the FIB is to selectively mill material away from a sample with nanometer accuracy. Material is removed via kinetic sputtering of the sample atoms resulting from collisions with the high energy

gallium ions. Computer controls allow the user to accurately select a portion of the sample to be milled by drawing the milling pattern directly on the ion beam generated image. Once the milling area is selected the beam is raster scanned across this area for a length of time deemed appropriate by the user.

As mentioned above, the FIB serves the secondary purpose of imaging. It can generate images in the same way an SEM generates images. As the beam is scanned across a sample surface a variety of detectors can be used to detect scattered ions. An image is generated by the contrast of scattered ions picked up by the detector between. This imaging capability facilitates nanometer precision milling by allowing the user to draw a well-defined milling area directly on the ion beam generated image. In some cases the ion beam can actually generate better images than the SEM depending on the properties of the sample. One final capability offered by the FIB is material deposition. A variety of organometallic compounds can be delivered via a gas injection system (GIS) into the milling area in order to deposit a desired material. The heat energy deposited by the beam causes the gaseous atoms to bond with the sample surface creating a layer of the desired material. This capability can be used, for example, to produce platinum coatings that prevent oxidation or protect from ion beam damage (discussed in the section 3.4.5) over a certain portion of the sample.

The above-mentioned capabilites give the FIB a wide range of practical uses. It is commonly used in TEM sample preperation to mill out a thin sheet from a sample that can be used for TEM studies. The FIB has also been used extensively for magnetic recording head pole piece shaping [34]. It also has many applications in the semiconductor industry including maskless patterning of semiconductor features

[35], photomask repairing, metallic line mending of integrated circuits, semiconductor doping, surface probing of substrate materials, and lithography [36].

3.4.2 Procedures

Use of the FIB as a milling tool for shaping MRFM cantilever tips presents some unique challenges not typically encountered during common FIB applications. One problem that arises is image distortion resulting from the magnetic field of the particle. The ferromagnetic particles glued to the end of the cantilever can exhibit high magnetic fields that can strongly influence both the ion beam and the electron beam when imaging the particle. This interaction produces a force on the beam called the Lorentz force expressed as

$$F = Q(\boldsymbol{v} \times \boldsymbol{B}) \tag{3.1}$$

where Q is the electric charge of a moving particle, $\boldsymbol{v}$ is the velocity of the particle, and $\boldsymbol{B}$ is the magnetic field. Figure 3.6 is an SEM micrograph of a strongly magnetized Sm_2Co_{17} particle exhibiting high stray magnetic fields evidenced by the distortion in the image.

Another source of image distortion originates from the cantilever's ability to store charge introduced by the ion or electron beam. This buildup of charge can also influence the beam via the Coulomb interaction force between charges described by

$$F = Q\boldsymbol{E} \tag{3.2}$$

where $\boldsymbol{E}$ is the electric field at the location of the point charge Q. The buildup of charge is signficantly less in cantilevers fabricated from doped silicon such as that appearing in the SEM micrograph in figure 3.1 (section 3.2), due to increased conductivity, but there is sometimes still some evident distortion as can be seen by the

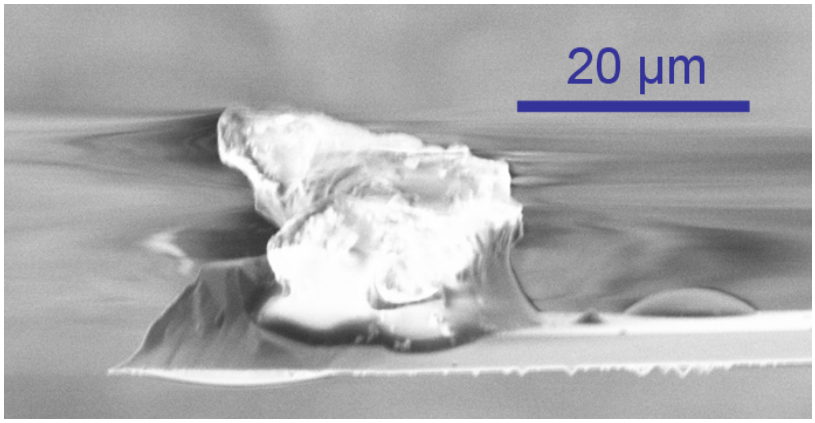

Figure 3.6: SEM micrograph of Sm_2Co_{17} particle showing some image distortion resulting from high stray magnetic fields.

oblong appearance of the spherical $Nd_2Fe_{14}B$ particle on the end of the cantilever in figure 3.1. In contrast, figure 3.7 shows an SEM micrograph of a particle on a silicon nitride cantilever, which has very low conductivity. The distortion here, most likely resulting from electrostatic charging, is much more severe and, in fact, such distortion can seriously impede the process of even finding the particle, let alone accurately milling it. The main impediment to milling is a misalignment between the FIB generated image on the computer screen and constructed milling pattern with the actual location of the beam raster scan on the particle during milling. In addition, it is also common for the particle to "drift" in one direction between successive images during milling. Both of the above effects become worse as the image is zoomed in. In addition to beam distortion, the force between built up charge on the cantilever and the beam can actually cause cantilevers with lower spring constants (such as the SiN and custom fabricated soft Si cantilevers used by our group) to flex, causing further imaging and milling problems.

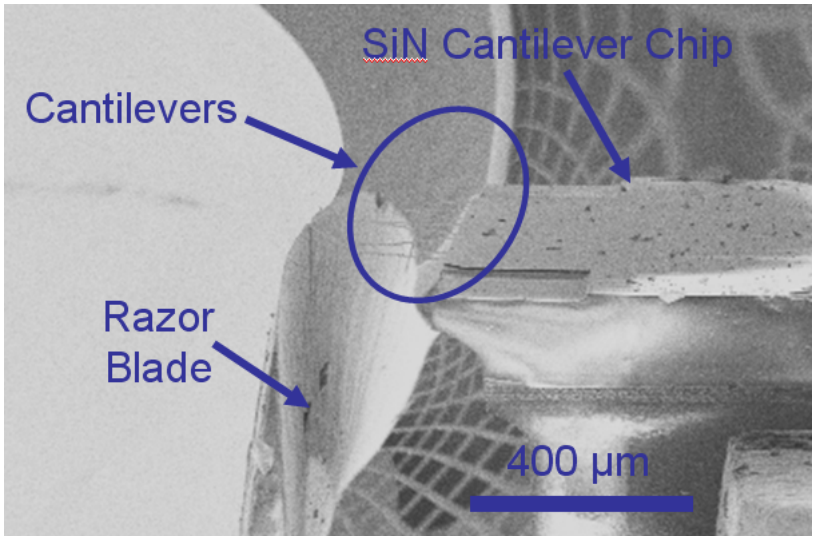

Figure 3.7: SEM micrograph of a SiN cantilever chip showing significant image distortion resulting from electrostatic charging

The best way to reduce the distortion caused by stray magnetic fields is to use particles that have not yet been fully saturated and saturate them after FIB milling. Using unsaturated particles also makes seperating the particles during the gluing process easier since the magnetic attraction between particles is reduced. The disadvantage to this approach is that, with reduced magnetization, the particles are less likely to align with an external field during the drying process. This becomes an even bigger problem when gluing very small particles because the attractive forces between cantilever, particle, and glue become dominant over the magnetic torque relied upon to align the particle's easy axis of magnetization in the proper direction.

The solution developed here to reduce undesired effects from electrostatic charging has been to position the end of the cantilever on the edge of a razor blade and apply slight pressure causing the cantilever to flex a small amount. This serves two purposes. The first is to hold the cantilever in place so that it cannot experience any movement

due to electrostatic forces. The second is to provide a conductive path from the cantilever to ground. Because of the insulative nature of the cantilevers, the razor's edge must be positioned within several microns of the imaging area (magnetic tip) in order to discharge that area of the cantilever. A special fixture was custom designed to allow precise positioning and flexing of the cantilever over the razor blade. The initial design of this fixture is not shown here but consists of a right-angled leaf spring that bends in two roughly orthogonal directions. Pressure is applied to the leaf spring via two 0-80 cap screws. This precise movement allows the cantilever to be positioned correctly on the knife edge with an accuracy of $\approx$ 2-4 μm.

Since the initial design, several revised versions of the FIB milling fixture have been designed and tested. The most recent and effective design is shown in figure 3.8. 0-80 cap screws (shown in black) are used to provide high resolution adjustment of both the vertical position of the cantilever above the razor blade (shown in gray) and the point of contact along the length of the cantilever. For the vertical adjustment, the back pressure needed for two way adjustment is provided by a thin metal piece that acts as a leaf spring (shown in blue). In the horizontal direction, two sliding rods (shown in yellow) guide movement of the leaf spring piece, with an internal compression spring (shown in turquoise) used to provide back pressure. The cantilever chip ($\approx$ 0.120" x 0.060" x 0.012" in dimension) is held in place on a removable block (shown in pink) using a small removable clamp (shown in purple) tightened with an 0-80 cap screw. The ability to quickly and accurately adjust the position of the cantilever relative to the knife edge and safely secure and remove the cantilever has resulted in much higher efficiency during the FIB milling process than the previous designs allowed. Much of decreased time requirement is a result of decoupling the two directions of adjustment

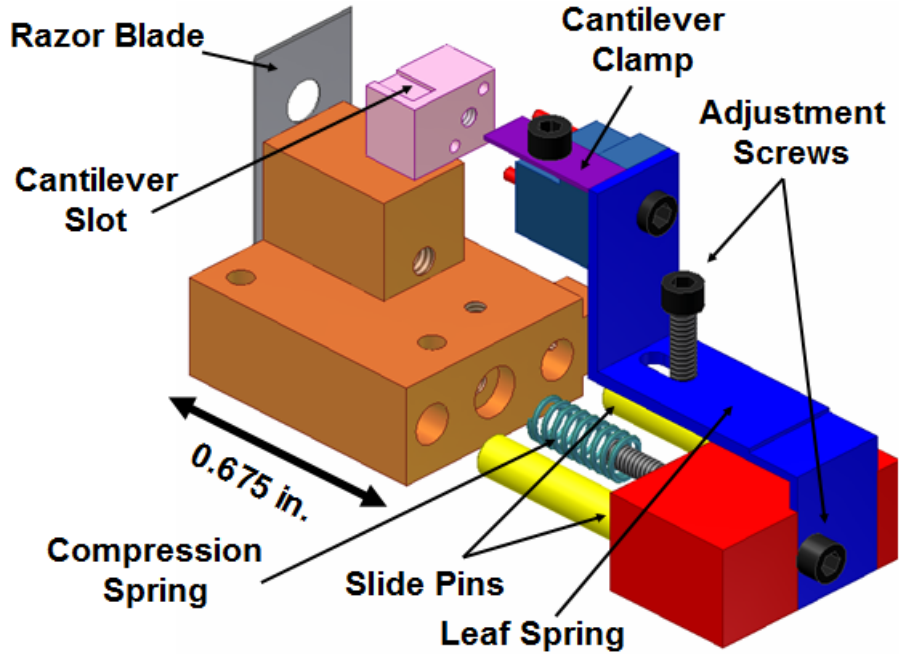

Figure 3.8: Exploded view of the most recent design of the FIB milling fixture used to prevent cantilever movement during FIB milling and provide a conductive path to ground to reduce electrostatic charging near the tip.

in the newer design. The improved image quality resulting from knife edge positioning produces much better FIB milling results during tip fabrication. Another advantage of using this fixture for FIB milling is that the cantilever chip can be held in place without the use of adhesive pads that could potentially contaminate the cantilever surface resulting in reduced Q.

3.4.3 Desired Particle Shapes

For many MRFM experiments of interest, a plain spherical particle or a particle with a flat surface will offer the necessary performance in terms of magnetic field gradient. For maximum sensitivity, however, it is desirable to fabricate tips with the

largest possible magnetic field gradient. In general, field gradient is maximized by making tip size smaller, but as tip size becomes smaller the working distance must also become smaller to take advantage of the increased gradient. For a fixed distance away from the surface of a spherical magnetic particle, however, the magnetic field gradient $\partial B_z/\partial z$ is maximized when the particle radius is one sixth of the distance from the particle's surface. This can be shown by the expression

$$\boldsymbol{H}(r > a) = \frac{3(\boldsymbol{\mu} \cdot \boldsymbol{r})\boldsymbol{r}}{r^5} + \frac{\boldsymbol{\mu}}{r^3} \tag{3.3}$$

for the magnetic field outside of a uniformly magnetized sphere where $\boldsymbol{H}$ is the magnetic field strength from the sphere, r is the distance from the center of the sphere, a is the radius of the sphere, $\boldsymbol{\mu}$ is the magnetic moment of the sphere, and $\boldsymbol{r}$ is a vector from the center of the sphere. The magnetic moment of the sphere is given by

$$\boldsymbol{\mu} = (4/3)\pi a^3 \boldsymbol{M} \tag{3.4}$$

where $\boldsymbol{M}$ is the magnetization of the sphere. From equation 3.3 the magnetic field gradient as a function of distance from the center of the sphere along the direction of magnetization can be expressed as

$$\partial B_z/\partial z = \frac{-6\mu}{z^4} \tag{3.5}$$

where μ is the magnitude of the magnetic moment and (z) is the distance from the sphere's center along the magnetization direction. This can also be expressed as

$$\partial B_z/\partial z = \frac{-8\pi a^3 M}{(a+d)^4} \tag{3.6}$$

where d is the distance from the surface of the sphere and M is the magnitude of the magnetization. This function can be shown to be maximized for a fixed distance

when $a = 3d$. This provides a convenient formula for determining the optimum tip radius for an experiment given a desired distance of the sensitive slice from the tip.

Typical MRFM experiments for the "horizontal geometry" discussed in section 2.2.4 are limited to minimum tip-sample spacings of around 500 nm. This leads to a desired tip radius of around 80 nm for maximized field gradient, and, therefore, sensitivity. For the vertical cantilever geometry much smaller tip-sample spacings can be used and the optimal tip radius is reduced proportionally. Since it is rather difficult to glue spherical tips with radii even as small as 80 nm, the alternative solution is producing tips that narrow down to a point using FIB milling. Below these sharp tips the field gradient is mostly influenced be the small portion of the tip directly above, rather than the much larger bulk of the particle further away. As such, the gradient is more characteristic of a tip with much smaller dimensions. Some disadvantages of this approach, related to ion beam damage layers, are discussed in sections 3.4.4 and 3.4.5.

3.4.4 Tip Fabrication Results

Figure 3.9 shows a milled Sm_2Co_{17} particle with a final tip end radius of about 50 nm. This represents just about the best result achievable (in terms of tip end radius), given the image resolution and ion beam spot size limitations of the instrument used. Sharp tips are desirable because they result in higher magnetic field gradients. If, however, a magnetically damaged layer is present (as discussed in section 3.4.5) as a result of FIB milling then the effective tip radius and maximum gradient will be decreased. MRFM experimental results using the tip shown in figure 3.9 hinted at just such a situation. In fact, data shows that a large portion of the end of the tip was

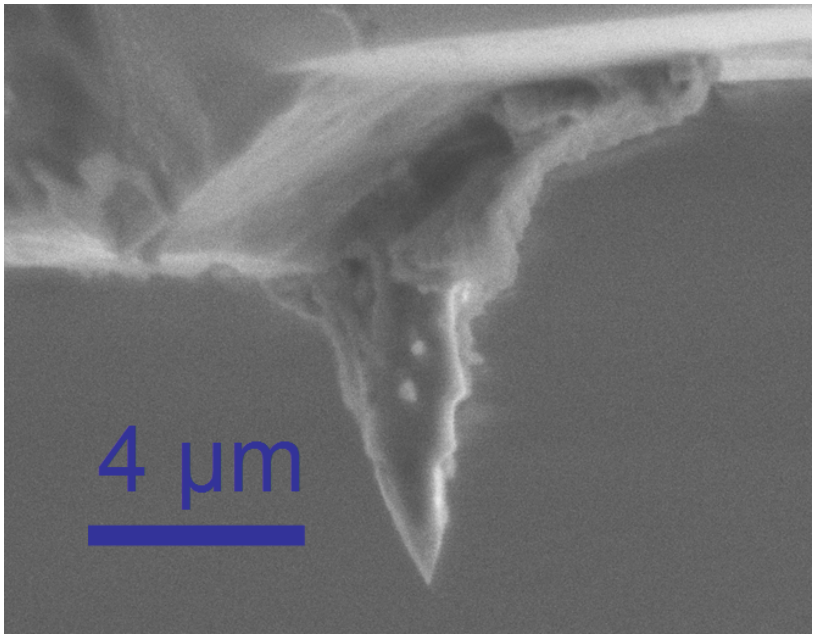

Figure 3.9: SEM micrograph of a FIB milled Sm_2Co_{17} tip with a tip radius of $\approx$ 50 nm on a Si cantilever.

non-magnetic. This increases the minimum distance between the magnetic portion of the tip and the sample and further reduces the maximum available gradient. For reference, figure 3.10 shows the same particle as figure 3.9 before any FIB milling. With the goal of reducing both overall particle size and FIB milling time/exposure, more recent efforts have involved gluing much smaller particles in the size range of a few microns (as small as $\approx$ 1 μm), however, as mentioned in section 3.4.5, this approach has faced significant obstacles related to loss in coercivity. Several images of particles in this size range are shown in section 4.3.7.

As mentioned earlier in this chapter and also in chapter 4, there can often be great variability between the characteristics of fabricated particles, even when consistent fabrication procedures are used. The fabricated magnetic tip in figure 3.11 is a prime

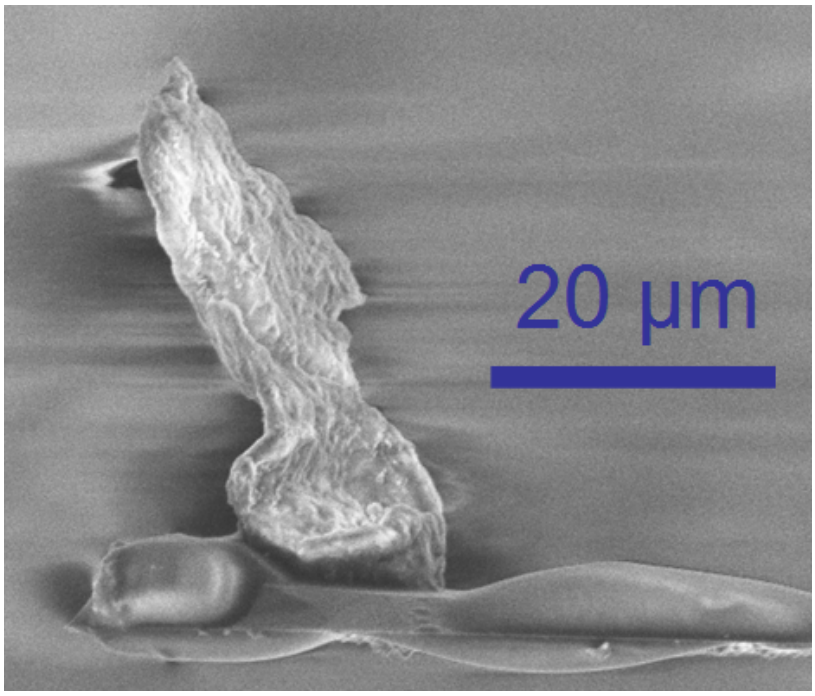

Figure 3.10: SEM micrograph of the same Sm_2Co_{17} tip from figure 3.9 (flipped upside down) before any FIB milling was performed.

example of this. Similar fabrication procedures were used for both this tip and the tip shown in figure 3.9. Although a very small tip radius, approximately 50 nm, was achieved, one can see that there is a large cavity in the middle of the tip indicated by the arrow in figure 3.11. This cavity was not created by the focused ion beam, but was present as a void in the bulk particle before any milling had been performed. This cavity makes the particle undesirable for a couple of reasons. The first is that this may lead to unpredictable magnetic properties such as low coercivity and anistropy. The second is that this artifact would likely make the tip very fragile. Since many MRFM experimental protocols require touching the tip to the sample surface to determine tip-sample spacing (this is also easy to do inadvertantly as well) there is a significant

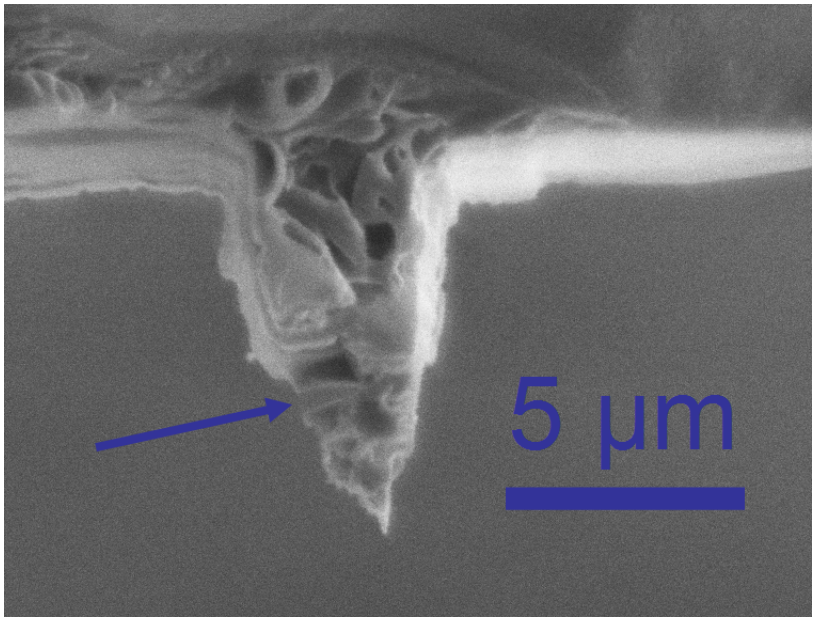

Figure 3.11: SEM micrograph of a Sm_2Co_{17} tip with a tip radius $\approx$ 50 nm on a Si cantilever. This tip shows several cavities from the particle that were exposed by the FIB milling process.

risk of breaking the tip during the experiment. One might also note from figure 3.11 that there are other cavities evident on the upper part of the tip as well. Although it is clear from the SEM image that this particle would not be an ideal choice to glue onto a cantilever, under the optical microscope the cavities in the tip are not visible. In addition, it is possible that many of these cavities were not exposed until after the particle is milled. This result bears evidence of one of many difficulties related to the microscopic nature of the tip fabrication process.

Another SEM image of a tip halfway through the FIB milling process appears in figure 3.12. This is an image of a Sm_2Co_{17} particle after FIB milling in two orthogonal directions. One can clearly see the square nature of the tip profile from this top view (view of the plane parallel to the two directions of ion beam milling). Milling from

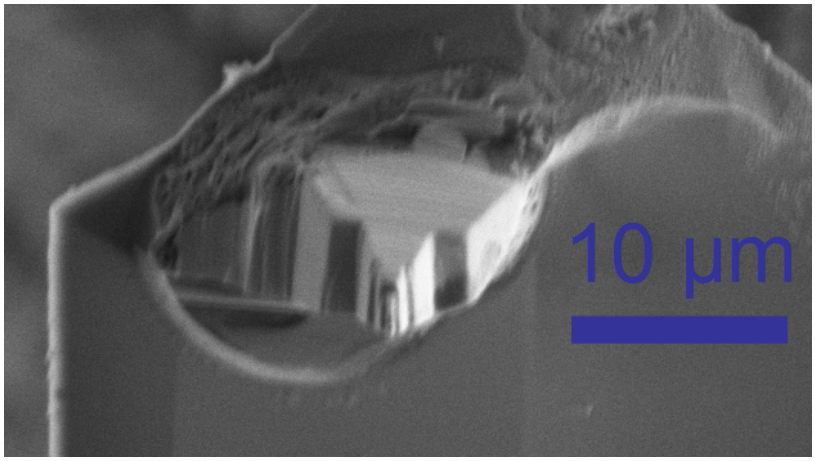

Figure 3.12: SEM image of a partially milled Sm_2Co_{17} tip on a Si cantilever. This is a view of the plane parallel to the two FIB milling directions. This image shows the rectangular profile of the tip produced by milling in the two orthogonal directions.

two different orthogonal directions is the most efficient approach ot particle milling. It is often necessary to perform a couple iterations from each direction because the aspect ratio of the particle after the first mill is often very large, which can lead to "fuzzy" two-dimensional SEM images when imaging from the same direction as the first mill during the final cuts. This often makes it difficult to obtain the clear image needed to produce a very accurate tip. Figure 3.13 shows a top view of the same particle before milling in the second direction. The top surface of the particle is enclosed in the bottom red outline and the side surface is enclosed in the top red outline. The red arrow shows the direction of the ion beam. In addition to the large aspect ratio, one can also see that the sides of the tip are angled rather than parallel to the direction of milling. This results from a combination of two things. The first is that the ion beam has a gaussian distribution. The second is that the material closest to the ion beam source must be removed before the material behind it can

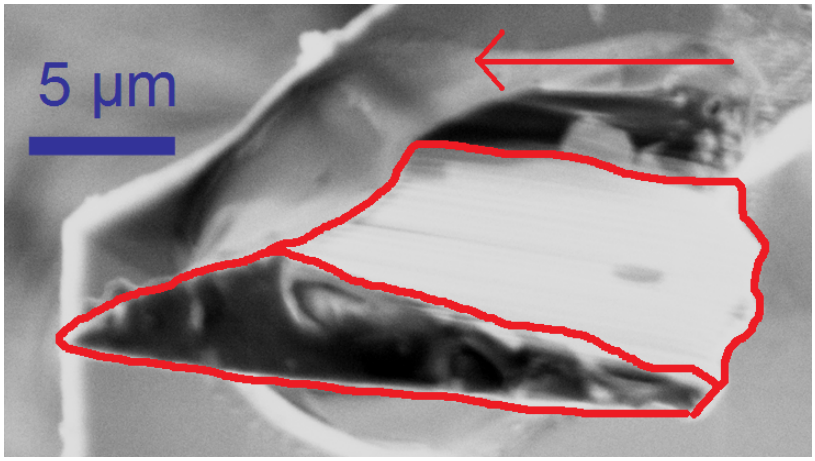

Figure 3.13: SEM image of a partially milled Sm_2Co_{17} tip on a Si cantilever. This is a view of the plane in which FIB milling is performed. This image shows the slight angle of the milled surface with respect to the direction of ion beam milling. The red outlines have been added to help distinguish two perpendicular surfaces on the particle. The red arrow shows the direction of the focused ion beam during this first direction milling.

be sputtered off. The result is that even if one mills in one spot long enough for the beam to breach the other side of the sample the Gaussian distribution of the beam current profile allows material to the sides of the beam to be continuously removed, with the portions closest to the center of the beam experiencing the highest level of material removal and, therefore, depth of penetration. This leads to milled surfaces that are slightly angled with respect to the direction of the ion beam.

3.4.5 Ion Beam Damage

One of the major disadvantages of ion beam milling is that it introduces many different damage effects into the milled sample. During the course of the research presented in this thesis one of the most common obstacles that was repeatedly encountered when trying to fabricate very small (1-2 micron scale) magnetic tips was

a significant decrease in coercivity compared to well-documented bulk values and the measured coercivities of larger particles. This lower than expected and desired coercivity has been observed most frequently in small focused ion beam milled particles, although some unmilled $Nd_2Fe_{14}B$ spheres have also exhibited such behavior. The loss in coercivity, however, has not been observed in any unmilled Sm_2Co_{17} particles or any milled particles larger than a few microns, which suggests that the loss in coercivity is a result of damage effects introduced by FIB milling that become more pronounced in smaller particles. This apparant correlation between ion beam milling and loss in coercivity prompted investigations into the possible mechanisms of damage introduced by the ion beam and the viability of such mechanisms producing the effects that have been observed.

One significant damage artifact is the implantation of gallium ions into the sample [37, 38]. A second is ion-beam induced alterations to the crystal structure which may lead to, among other things, an amorphous layer on the surface of the sample [38, 39, 40, 41]. This crystal damage is a result of both impinging Gallium ions and "recoil" atoms of the sample knocked loose by kinetic collisions with either the Gallium ions or other recoil atoms [38]. Both ion implantation and crystalline structure damage can occur either as "bottom wall" damage directly into the sample when milling into or imaging the surface or "sidewall" damage when milling material off the side of a sample [38, 39, 42]. Figure 3.14 shows an illustration of the bottom wall and sidewall damage areas of a tip that is being milling with the ion beam. The bottom wall damage layer is thicker, as well as more susceptible to ion implantation, as evidenced by higher gallium concentrations in this region [38] after beam exposure. In the case of MRFM probe tip shaping, by the end of the milling process most damage is present

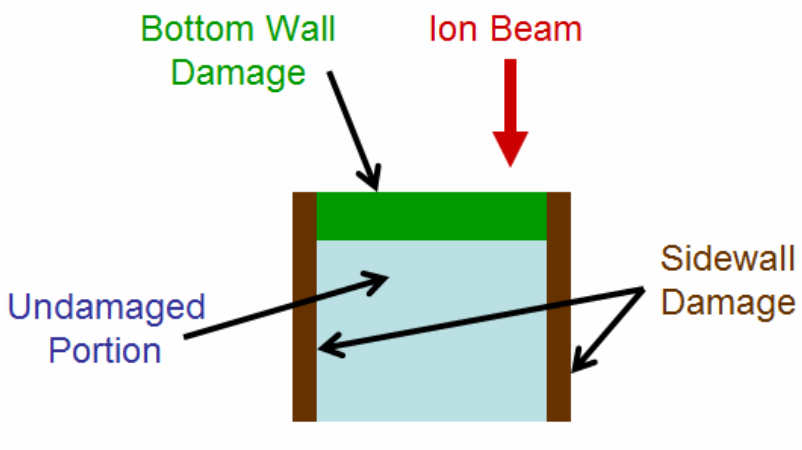

Figure 3.14: Illustration of the bottom wall and sidewall damage regions of a tip after imaging and milling exposure to the ion beam. This image is not drawn to scale.

is sidewall damage since material is typically milled off the sides of the particle. Only one surface will have signficant bottom wall damage, and this is caused by imaging from the last direction of ion beam milling. In order to minimize this damage it is desirable to take as few images as possible during the milling process.

Ion Beam Damage Depths

Since most applications of the FIB are in the semiconductor industry most FIB damage studies have dealt with semiconductor materials such as silicon. Studies on FIB damage in magnetic materials, especially the rare-earth permanent magnets used for MRFM cantilever tips, is limited. Experimentally determined damage depths (for a 30 keV gallium ion beam) in silicon vary from 10-35 nm in the sidewall and 30-60 nm in the bottom wall. [38, 39, 40, 42]. The maximum depth of beam induced point defects is documented to extend as deep as 70 nm in the bottom wall, however, maximum defect density in this study occured at 18 nm [43]. Damage depth has been

found to correlate strongly with beam energy but is relatively independant of beam current [38], once the maximum damage depth has been reached. This maximum damage depth occurs when an equilibrium is formed between the sputtering of ions off of the surface and an increase in damage depth with sample exposure.

Damage Depth Simulations

Ion implantation simulations have proven fairly useful and accurate in predicting FIB induced damage depths [38, 40, 44]. One particularly popular group of simulation programs is called "The Stopping and Range of Ions in Matter" (SRIM) [44]. This program makes use of the "Dynamic Transport of Ions in Matter" (TRIM) code to perform a monte-carlo type statistical simulation of ion implantation using a "quantum-mechanical treatment of ion-atom collisions" [40]. Figure 3.15 shows simulation results from an SRIM simulation of 30keV gallium ion implantation in silicon. The simulation shows trajectories of both gallium ions (shown in red) and secondary recoil silicon atoms (shown in green). The horizontal trajectories (representative of sidewall damage) and vertical trajectories (representative of bottom wall damage) agree well with the maximum damage depths discussed in the previous section. The average ion implantation depth was about 28 nm with a maximum ion density depth of around 20 nm. Because experimental data on damage depths in magnetic materials is limited, SRIM simulations were performed to get some indication of the damage depths that can be expected on these denser materials. Figure 3.16 shows simulation results for 30 keV gallium ion implantation into $Nd_2Fe_{14}B$ and figure 3.17 shows corresponding results for implantation into Sm_2Co_{17}. The simulation damage depths (for both bottom wall and wide wall) for these materials were roughly half of the damage depths yielded by the silicon simulations and experimental results. This is

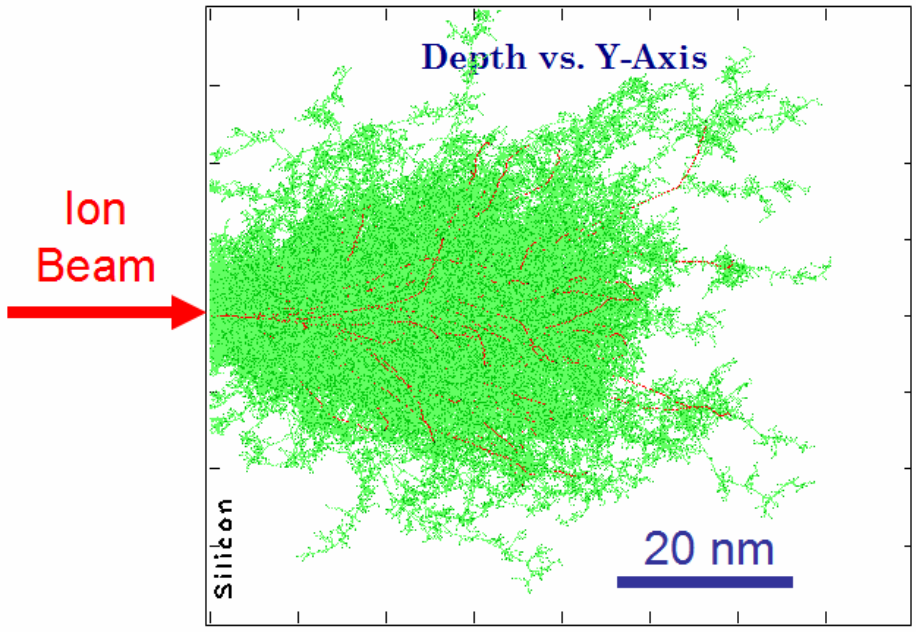

Figure 3.15: SRIM Simulation of ion implantation and recoil atom trajectories from 30 keV Gallium ions into silicon. Gallium ion trajectories are shown in red and recoil silicon atom trajectories are shown in green.

well-explained by the higher atomic weight of the atoms in the rare earth permanent magnets. These heavier atoms will experience less recoil during a collision with an ion of the same kinetic energy than silicon atoms and stop the ions at a shallower depth. Of the two rare-earth magnets simulated, $Nd_2Fe_{14}B$ sustained deeper ion beam damage than Sm_2Co_{17}, however the difference was very small.

FIB Magnetic Damage Studies

FIB induced damage in magnetic materials has been the focus of many studies [34, 37, 45, 46, 47], although certainly not as many as damage in silicon. Most of these studies have focused on the effect of FIB milling on magnetic properties, without *directly* quantifying damage depth, hence the need for the simulations in section

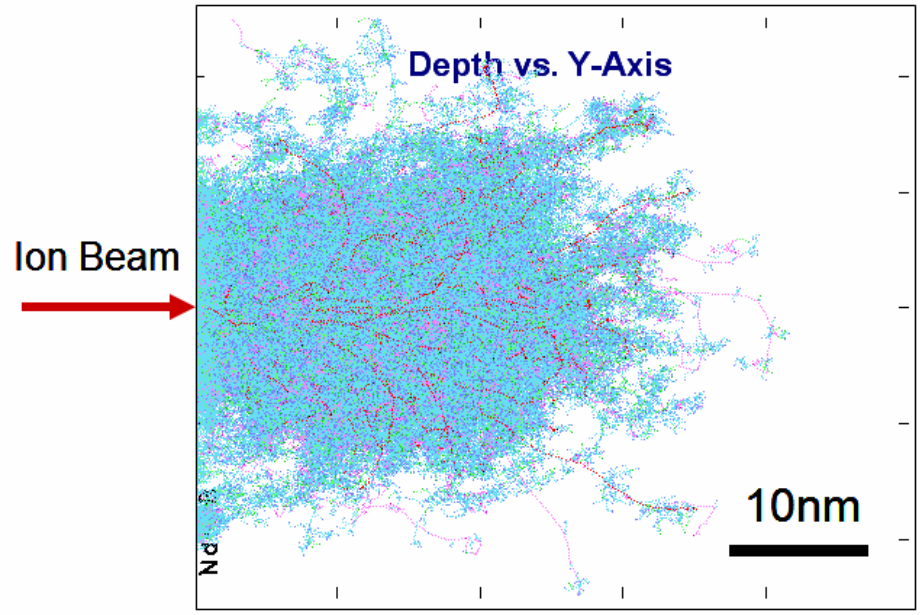

Figure 3.16: SRIM simulation of ion implantation and recoil atom trajectories from 30 keV gallium ions into $Nd_2Fe_{14}B$. Implanted gallium ion trajectories are shown in red and target recoil atoms (Nd, Fe, and B) are shown in the other various colors.

3.4.5. One study [34] did indirectly estimate FIB induced magnetic damage depths in perpedicular magnetic write heads by analyzing the write spacing loss (loss in resolution determining maximum data density) resulting from FIB exposure. The results from this study indicated that FIB milling of the pole tip resulted in a 30 nm magnetically "dead" layer. This result corresponds reasonably well with damage depth simulations performed on Sm_2Co_{17}, $Nd_2Fe_{14}B$, and permalloy ($Ni_{80}Fe_{20}$, results not shown). One should note that the magnetic material in this study was not specified, however, simulations performed on the various magnetic materials mentioned above all yielded very similar results and most magnetic materials have similar mass density (since they are usually primarily composed of Nickel, Iron, and/or Cobalt), which is

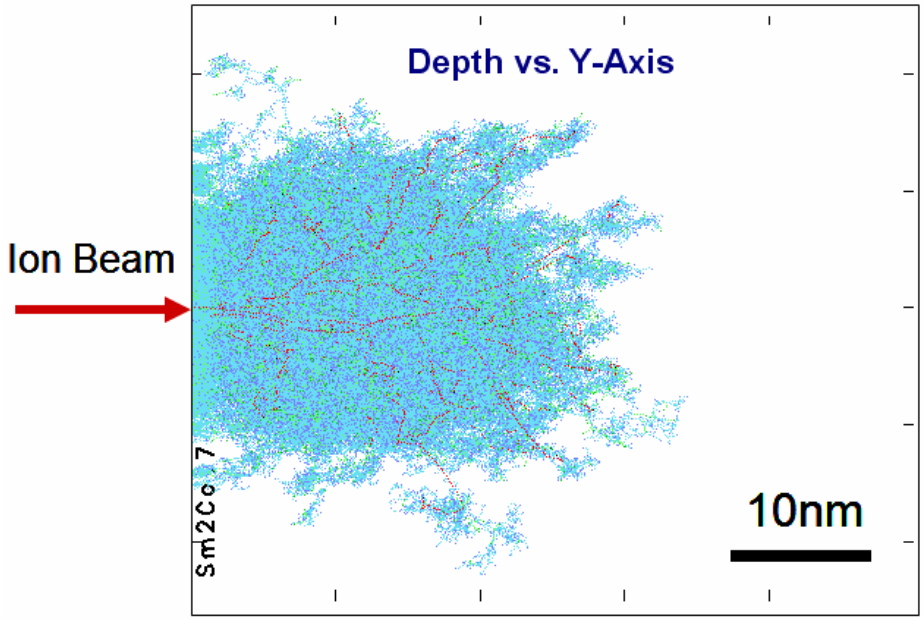

Figure 3.17: SRIM simulation of ion implantation and recoil atom trajectories from 30 keV gallium ions into Sm_2Co_{17}. Implanted gallium ion trajectories are shown in red and target recoil atoms trajectories (Sm and Co) are shown in the other two colors.

perhaps the most influential factor in damage depth. The milling of magnetic particles for use as MRFM cantilever tips is very similar to the milling approach taken in the above-mentioned study, making it extremely relevant to this probe tip fabrication research.

Several studies have focused on the modifications in magnetic properties that result from FIB exposure. Many of these focus on soft (low coercivity) magnets such as permalloy [37, 46]. One study [37] indicates an increase in coercivity in 30 nm permalloy thin films after ion beam exposure, attributed to increased domain wall pinning resulting from higher stress in the implanted region and increased grain size. Another study [46], however, found that comparable ion beam doses resulted in

complete loss of ferromagnetic properties for films thinner than 15.5 nm. It in unclear how to extend these results to larger rare-earth magnets or how to experimentally determine the thickness of certain damage layers in such particles, but there is little doubt that magnetic alteration on some scale will occur with exposure to ion beam irradiation.

Magnetic Damage Conclusions

As mentioned earlier and shown by several of the magnetometry measurements in section 4.3.7 (see specifically figures 4.20 & 4.21 and 4.16 & 4.17), there has been extensive observation of significantly lowered coercivity exhibited by micron-sized focused ion beam milled particles in this research. Although, there is no doubt that significant direct local FIB induced damage can lead to loss in coercivity or magnetic behavior altogether, such damage should be confined to the outer portions of the particle within the ion and recoil atom penetration depth of the surface. Even assuming a 50 nm non-coercive magnetic layer is produced on the entire outside surface of a 1 μm diameter sphere by the FIB milling process, over 70 % of the particle should still maintain its normal magnetic properties. Based on the damage depth research presented, above the bottom wall damage layer should be closer to 20 nm thick and the bi-directional FIB milling process discussed in section 3.4.4 should reduce the damage to the other surfaces since they only experience sidewall damage. The conclusion is that direct ion beam implantation and seconary recoil atom damage cannot be the cause of the observed loss in coercivity.

One theory proposed here for the observed loss in coercivity is that FIB induced particle heating results in changes to the crystalline and, therefore, magnetic properties of the entire particle. A significant amount of heat is deposited into any sample

that is exposed to the ion beam. Simple thermal calculations reveal that if the amount of beam energy deposited over even a short time period compared to the normal milling time is transferred completely into heat energy to even a larger sized (many micron) particle, the temperature increase would far exceed that necessary to drastically alter the magnetic properties of the material. Assuming that all the ion beam energy is deposited into the particle as heat energy and none is dissipated through thermal contact with the cantilever, a spherical Sm_2Co_{17} particle with a radius of 1 μm and specific heat of 376 J/kg°C would experience an over 10^6 C° temperature increase after 2 minutes of exposure to a 30 keV (typical ion beam energy used during milling) 30 pA ion beam. Usually the necessary exposure time is much longer, even when using higher ion beam currents around 100 pA for the initial milling stages. Obviously, only a fraction of the beam energy is deposited as heat due to kinetic sputtering of atoms, the alteration of chemical bonds, etc. Furthermore, some of the heat energy is able to escape the particle through thermal contact with the epoxy and cantilever. Modeling these dynamics would be extremely complicated and was beyond the scope of the research effort available for this study, so no definite conclusion has yet been drawn about this theory. Nonetheless, the theory appears to offer a reasonable explanation for the loss in coercivity. Based on the lower heat capacity of smaller particles, it would also explain why smaller particles seem to be more susceptible to the loss in coercivity.

Several studies [48, 49, 28, 50, 29, 51, 52, 53, 54, 30] have shown that alterations to the microstructure of rare earth permanent magnets, including grain size, grain size distribution, the spatial distribution and amorphisation of magnetic phases, and the migration of impurities can affect coercivity. Naturally, the subjection of any

crystalline material to large amounts of heat can result in such changes. If ion beam induced heating is resulting in changes to the crystal structure or an altogether transition from the crystalline phase to an amorphous phase, it is likely that coercivity would decrease. If enough heat is being transferred to the particle it would be possible for the entire particle to undergo such changes, not just the outer layers that are directly affected by the ion beam. The reported sensitivity of coercivity to heat treatment and annealing procedures for sintered rare-earth permanent magnets in [29, 53] gives further cause for concern that ion beam induced heating could be the origin of the loss in coercivity.

There is definitely a need for further exploration of the loss in coercivity discussed above. Although the research goal here is to eliminate this loss in coercivity, it would also be of interest to understand its origin. In the interest of the progress of MRFM experiments, however, a satisfactory solution without fully understanding the underlying mechanism(s) of the damage would be acceptable. One such proposal would be to use reduced ion beam currents and longer milling times to allow the heat deposited by the ion beam to dissipate through the cantilever, reducing the temperature increase experienced by the magnetic tip. Such efforts, along with more investigations of possible damage mechanisms related to FIB milling, especially ion beam induced heating, will be a major focus of future MRFM tip fabrication research.

CHAPTER 4

Magnetic Tip Characterization

4.1 Overview

Cantilever and magnetic tip characterization is an important part of MRFM experimentation. The magnetic properties of the tip and mechanical properties of the cantilever have a dominant influence on sensitivity and resolution, which are ultimately determined by the magnetic field gradient of the tip and thermally driven cantilever vibrations (thermal noise). I have developed a room temperature cantilever magnetometer that is used to characterize the magnetic moment, anisotropy, and coercivity, and obtain the hysteresis loop of the magnetic tip. This instrument is also capable of measuring the cantilever Q, which plays a part in determining the ultimate sensitivity of a particular cantilever for both magnetometer and MRFM measurements.

As discussed in section 2.2, one of the most important cantilever properties is the mechanical quality factor (Q), since the minimum detectable force for a particular cantilever has an inverse square root dependence on the cantilever Q. If a certain experiment, such as the single electron spin experiment described in [13], requires very high sensivity it may be necessary to find a cantilever with a very high Q before

the experiment can be conducted. Although most cantilever properties of interest such as physical dimensions, resonant frequency, and spring constant are reasonably consistent in a fabricated batch of cantilevers, quality factor can vary over a large range, and must therefore be determined experimentally. Cantilever properties and their effects on sensitivity are discussed in section 4.2.4. Cantilever quality factor is discussed in more detail in section 4.3.3.

The magnetic cantilever tip typically has more uncertainty concerning its properties of interest than the cantilever. For this reason, more effort is usually expended characterizing this part of the probe. The magnetic field gradient of the particle and its spatial mapping is one of the quantities of greatest interest. Increasing the field gradient is the most effective way to increase the force produced from the probe-sample interaction. Another property of interest is the overall magnetic moment of the tip. In general, it is advantageous to have a small magnetic moment. One reason is that smaller magnetic moments produce less spurious coupling with externally applied fields [5]. The coercivity, anisotropy, and overall moment of the tip and magnetic field induced damping experienced by the cantilever are also properties of interest for many MRFM experiments. As discussed in section 3.2, some experiments require high-coercivity and high-anisotropy tips so that external fields do not influence the magnetic field produced by (or magnetization of) the tip.

There are a variety of methods and instruments that can be used for tip and cantilever characterization. The most versatile instrument used for such characterization is the MRFM itself. A typical MRFM has all the capabilities needed to quantify the properties mentioned above. This instrument is also, however, costly and time consuming to operate. In terms of sensitivity, versatility, efficiency, and cost, cantilever

magnetometry is a very effective tool for characterizing cantilevers and magnetics tips used in MRFM. Cantilever magnetometry has proven to be an extremely sensitive tool for extracting hysteresis loops from individual micron and submicron magnetic tips on cantilevers [19, 20]. Tip magnetic moment, coercivity, anisotropy, thermomagnetic fluctuations, and magnetic dissipation can also all be determined from measurements taken using this instrument [19, 20]. In addition, the instrument allows for easy measurement of cantilever quality factor [19, 20].

4.2 Cantilever Magnetometry

The term cantilever magnetometry can be used to refer to a number of different techniques used for characterizing the magnetic properties of samples fixed to the end of micromechanical oscillators. They all rely on the detection of certain interactions between the magnetic sample and externally applied field(s) by measuring a certain response in the cantilever. There are many variables in the experimental setup that make some cantilever magnetometers much different from others in terms of performance [17, 18, 19]. Some of these include operation temperature, air pressure, maximum external field, cantilever properties, vibration isolation, and vacuum pumping technique. The last two affect the susceptibility of the instrument to outside sources of noise.

There are several different options for displacement detection of the cantilever in the magnetometer. The most widely used method is probably optical inteferometry (Discussed in section 2.2.1) due to its high sensitivity. The choice of detection method, however, is not usually the deciding factor in ultimate sensitivity. Like the MRFM, the ultimate sensivity of the cantilever magnetometer is usually determined

by the thermomechanical noise of the cantilever being used, which depends on the physical properties of the cantilever. Previous research [19] has reported magnetic moment resolution (sensitivity) as high as 10^4 μ_B or approximately 10^4 electron spins for a cyrogenic magnetometer with a superconducting 6 T magnet, when measuring magnetic fluctuations in particles. This corresponds to a magnetic moment of about 10^{-19} J/T.

4.2.1 Principles of Cantilever Magnetometry

The cantilever magnetometer, in the simplest of terms, measures the magnetic moment of a sample fixed to the end of a cantilever as a function of external field. Cantilever magnetometry can make use of one of two different interactions to generate a force between the magnetic particle and the external magnetic field. The first interaction, made use of in the alternating gradient magnetometer [55], relies on the gradient coupling between the sample magnetic moment and an alternating (oscillating) magnetic field gradient. This produces a force

$$\boldsymbol{F} = (\boldsymbol{\mu} \cdot \nabla)\boldsymbol{B} \tag{4.1}$$

where $\boldsymbol{\mu}$ is the magnetic moment of the sample and $\boldsymbol{B}$ is the external magnetic field. The second interaction, made use of in the cantilever magnetometer (sometimes referred to as the cantilever bending magnetometer or torque magnetometer) used for this research, relies on the torque produced on a magnetic sample (moment) from a magnetic field [18] given as

$$\boldsymbol{\tau} = \boldsymbol{\mu} \times \boldsymbol{B} \tag{4.2}$$

where $\boldsymbol{\tau}$ is the magnetically induced torque on the sample. For a particle attached to the end of the cantilever this torque is mechanically equivalent to a force

$$F = \frac{\tau\alpha}{l} \tag{4.3}$$

at the end of the cantilever acting parallel to the cantilever's thickness, where l is the length of the cantilever and α is correction factor that accounts for nonlinear bending of the cantilever. Because of this bending the effective length $l_e = l/\alpha$ is shorter than the actual length of the cantilever. For the first flexural mode of a beam cantilever α equals 1.38 [12, 19, 56, 57]. For the large triangular cantilever on the Veeco SiN chip (model # MLCT-NONM), finite element analysis simulations [1] showed the correction factor α to be about 1.28. The cantilever, tip, and external field interaction discussed above is illustrated in the diagram shown in figure 4.1.

There are also two different modes of operation in which the above described forces can be detected [17]. The first is the static mode of operation. In static mode the force produced on the cantilever by the interaction results in a cantilever displacement

$$z = \frac{F_z}{k} \tag{4.4}$$

where F_z is the force component in the direction of cantilever displacement and k is the spring constant of the cantilever in the direction of displacement. The second mode of operation is the dynamic mode in which the cantilever is driven at its resonant frequency by one of the methods described in section 2.2.2. In this mode of operation the force signal coupled to the cantilever is amplified by an amount equal to the Q of the cantilever, resulting in much higher sensitivity. The signal is actually deteced as

[1] Denis Pelekhov, Unpublished

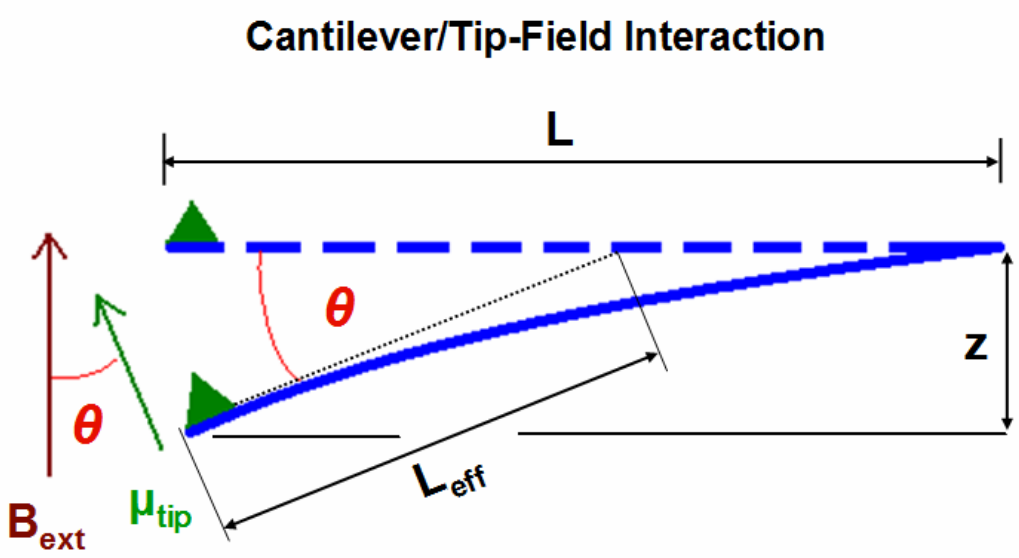

Figure 4.1: Illustration showing some of the key concepts involved in the interaction between magnetic particle, cantilever, and magnetic field in cantilever magnetometry.

a frequency shift

$$\Delta f + f_0 = \sqrt{\frac{k + \Delta k}{m}} \tag{4.5}$$

in the cantilever's resonant frequency f_0 resulting from a modified spring constant $k + \Delta k$, where m is the effective mass of the cantilever and sample. Effective mass is the equivalent mass at the end of the cantilever that would result in the same resonant frequency as the true mass distributed along the length of the cantilever.

4.2.2 Magnetic Moment Derivation

In order to effectively modifiy the spring constant of the cantilever, the force produced on the cantilever from the magnetic tip must be position dependent. This is exactly the case for the torque produced between the particle and magnetic field.

When performing torque magnetometry there are two possible cantilever-particle orientations that can be used. In the first case (depicted in figure 4.1) the magnetic moment of the particle is parallel to the thickness of the cantilever. In the second case the magnetic moment of the particle is oriented parallel to the length of the cantilever. In both cases the external magnetic field is applied parallel to the magnetic moment of the particle and the torque equation describing the interaction applies to both orientations. Because the external field is approximately homegenous, gradient dependent forces on the magnetic tip can be ignored. The torque produced according to equation 4.2 can be rewritten as

$$\tau = \mu B \sin\theta \tag{4.6}$$

where θ is the angle between the magnetic moment and external field. Assuming that the angle between the magnetic moment and the cantilever is fixed, for small vibration amplitudes a small angle approximation can be used to simplify the equation to

$$\tau = \mu B \frac{z}{l_e} \tag{4.7}$$

where z is the displacement at the end of the cantilever. As the deflection of the cantilever increases during an oscillation cycle an equivalent force that also increases with deflection is produced. This position dependent force effectively stiffens or softens the cantilever (spring constant), changing its resonant frequency. Equating the change in spring constant with a force per unit displacement distance as in equation 4.4 and combining this with equations 4.3 and 4.7 results in

$$\delta k = \frac{\mu B}{l_e^2} \tag{4.8}$$

where all the quantities on the right are known under normal experimental conditions.

Although cantilever spring constant is usually reasonably well-known, in most cases the effective mass of the cantilver and sample is unknown, making equation 4.5 difficult to apply for calculating change in spring constant from a measured change in resonant frequency. By taking the derivative of k with respect to f_0 in the following equation for oscillations of a spring:

$$k = mf_0^2 \tag{4.9}$$

we obtain

$$\delta k = 2mf_0\delta f_0 \tag{4.10}$$

Combining equations 4.9 and 4.10 to eliminate m yields

$$\delta k = 2k\frac{\delta f}{f_0} \tag{4.11}$$

Equation 4.11 can then be combined with equation 4.8 to eliminate δk and solved for μ resulting in

$$\mu = \frac{2kl_e^2\Delta f}{Bf_0} \tag{4.12}$$

where δf has been replaced by the measurable frequency shift Δf. This provides a direct method for calculating the magnetic moment of a particle for small $\Delta f/f_0$. As mentioned earlier, this derivation assumes that the tip has a much higher anisotropy field than the external field applied so that the direction of magnetization does not tilt toward the external field as the cantilever bends away from the equilibrium position. This will be discussed more in section 4.2.3, but it turns out to be a valid assumption for rare-earth magnets possessing anisotropy fields much higher than the applied external field.

4.2.3 Hysteresis and Anisotropy Effects

The derivation for magnetic moment presented in section 4.2.2 assumes that the direction of magnetization of the particle on the cantilever is fixed with respect to the cantilever and as the cantilever tilts by an angle θ, the tip magnetization also tilts by an angle θ. According to the model in [19] for a single domain particle, the magnetization direction of the particle will always tilt by an angle ϕ with respect to the cantilever toward the direction of the external field as the cantilever tilts the particle's original magnetization axis away from the external field axis. This is illustrated for a single domain particle in figure 4.2. The angle ϕ can be determined by minimizing the magnetic energy of the particle, which is the sum of the anisotropy and Zeeman energies [19] given by

$$E_m = K_u V \sin^2\theta - H M_s V \cos(\theta - \phi) \tag{4.13}$$

where E_m is the total magnetic energy, K_u is the uniaxial anisotropy, V is the volume of the particle, H is the external field strength, and M_s is the saturation magnetization of the particle. Minimizing E_m in the small-angle approximation results in the expression

$$\mu = 2kl_e^2 \frac{\Delta f}{f_0} \frac{H + H_k}{H H_k} \tag{4.14}$$

where $H_k = 2K_u/M_s$ is the anistropy field. Some particles studied in [19] using this model had uniaxial anistropy fields dominated by shape anistropy (oblong soft magnetic particles), while others had fields dominated by magnetocrystalline anistropy (coercive/hard rare-earth magnetic particles). For particles possessing high uniaxial (overall) anisotropy ($H_k \gg H$) equation 4.14 simplifies to the expression in equation 4.12. Rare-earth magnetic particles often satisfy this condition of high uniaxial

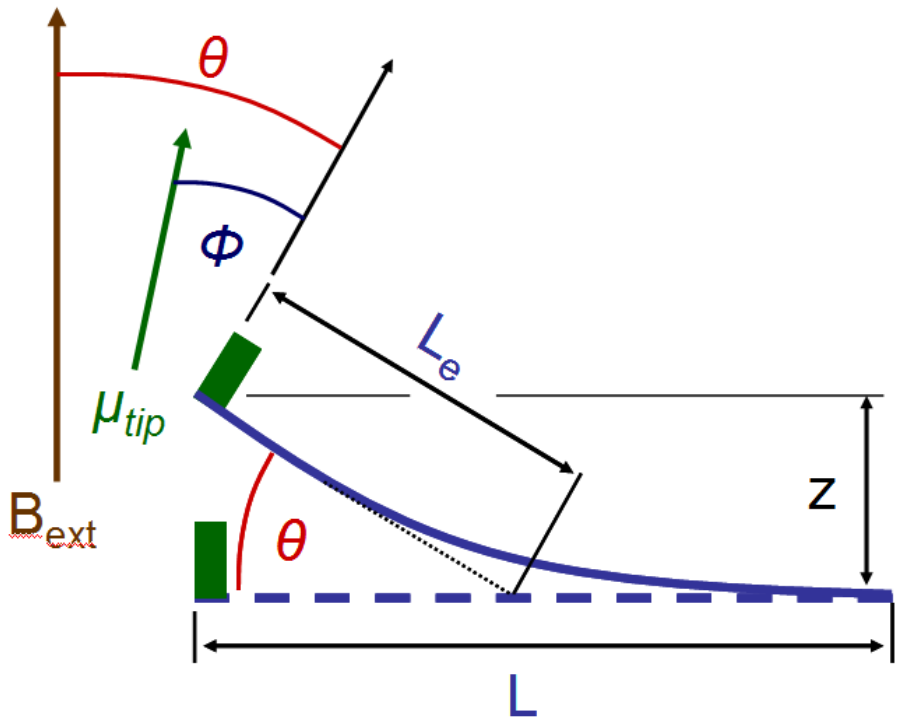

Figure 4.2: Model showing the interaction between a single domain particle on a vibrating cantilever and an static external field. The tilting of the particle's moment away from its original position with respect to the cantilever is an effect of finite magnetic anisotropy.

anistropy for magnetic fields below a few Tesla depending on temperature, which has a large effect on magnetocrystalline anistotropy. For example, the bulk value of $\mu_0 H_k$ (magnetocrystalline anisotropy contribution only) for $Pr_2Fe_{14}B$ at 4.2 K is 30 T [19, 58] while at room temperature the bulk value of $\mu_0 H_k$ decreases to 8.7 T [58]. In [19] the experimental value of $\mu_0 H_k$ (total uniaxial anisotropy) for a submicron particle was found to be 16.2 T, with the reduced anisotropy attributed to possible oxidation or FIB milling damage.

Another tip-field interaction model, similar to that discussed above, was developed in [57] and used to study nickel magnets in [20]. This model also considered a minimization of the magnetic energy of the particle, but modeled the shape anisotropy of the particle, only, as

$$E_s = \frac{1}{2V}\mu_0\mu^2[N_t\cos^2(\phi) + N_L\sin^2(\phi)] \tag{4.15}$$

where N_t and N_L are the demagnetization factors of the particle in the directions perpedicular and parallel to the length of the cantilever, respectively. Because nickel magnets have domains much smaller than the size of the magnets studies in [20] it appears that this model was established to represent the more general case of a multi-domain particle with properties more typical of bulk samples. Minimizing the magnetic energy of the particle and using a small angle approximation and the generally valid assumption that $\Delta f \ll f_0$ yields the model

$$\Delta f = \frac{f_0\mu B\Delta B}{2kl_e^2(B + \Delta B)} \tag{4.16}$$

where

$$\Delta B = \mu_0\mu\frac{N_t - N_L}{V} \tag{4.17}$$

In this model, the effective anisotropy field ΔB is equivalent to the anisotropy field H_k in the first model if the internals of each variable (anisotropy energy and its origin) are ignored. The researchers in [20] established that solving equation 4.16 as a quadratic equation for B_m, where $B_m = \mu_0\mu/V$, yields the equation

$$B_m = \frac{B_k}{2B} \pm \frac{1}{2B}\left(B_k^2 + \frac{4B_kB^2}{N_t - N_L}\right)^{1/2} \tag{4.18}$$

where

$$B_k = \frac{2k\Delta f\mu_0 l_e^2}{Vf_0} \tag{4.19}$$

allowing hysteresis loop extraction. The key to using this formula is finding a least squares fit of the data for $\Delta N = N_t - N_L$ and μ using equation 4.16 where μ is assumed to be the saturation magnetic moment. Although the modeling of shape anisotropy only (represented by ΔN) was valid based on the isotropic and low coercivity properties of the nickel magnets studied in [20], a least squares fit of this parameter to the magnetometry data would reflect any magnetocrystalline anisotropy contributions to the overall (uniaxial or effective) anisotropy. Likewise, in the first model, a least squares fit of H_k to the data would reflect any shape anisotropy contribution to the uniaxial anisotropy. In fact, the authors who developed the first model [19] used this model to evaluate the properties of low-coercivity cobalt magnets which experienced anistropy fields dominated by their shape rather than crystalline structure. Hence the two models discussed above are equally valid, but have different ways of calculating anisotropy field, based on the dominant anisotropy mechanism (magnetocrystalline or shape). In [20] they were able to obtain an excellent fit to the data, however, there was significant deviation at low external field. According to the authors of [20], this occurs because the magnetic moment is not yet saturated at low external field, as assumed in the model. This appears, then, to be a shortcoming experienced by the model in [19] as well. Because of this, it may be difficult to apply these techniques for hysteresis extraction accurately to low coercivity particles for small external field sweep ranges that do not fully saturate the particle and, therefore, do not allow an accurate fit of the anisotropy constant to the data.

Stricly speaking uniaxial anisotropy and coercivity (switching field) are related to each other through the magnetocrystalline anisotropy of the various magnetic phases in the particle and the particle shape. In general, coercivity (switching field) has a

positive correlation with (effective) anisotropy field. The relationship, however, is a complex function of the microstructure and particular magnetization process of the particle [28, 29, 30] as well as particle shape. This can help to explain some of the magnetometry data shown in section 4.3.7 that can mislead one into thinking that coercivity and anisotropy are not related.

4.2.4 Magnetometer Sensitivity and Noise

As mentioned earlier, the sensitivity of cantilever magnetometry is limited by the intrinsic thermomechanical noise, analogous to Johnson noise across a resistor, of the cantilever used in the measurement [16, 19]. This noise originates from the angstrom scale vibrations experienced by the cantilever at finite temperature. Thermal noise in a cantilever can be modeled according to the equipartition theorem and the fluctuation-dissipation theorem of statistical mechanics as the RMS force noise [14, 16, 19]

$$F_n = \sqrt{\frac{2kk_BT\Delta\nu}{\pi Q f_0}} \tag{4.20}$$

where k is the cantilever spring constant, k_BT is the thermal energy, $\Delta\nu$ is the bandwidth, Q is the quality factor of the cantilever, and f_0 is the cantilever resonant frequency. The signal-to-noise ratio of the measurement can be expressed as

$$(SNR) = \frac{F}{F_n} \tag{4.21}$$

where

$$F = \mu B \frac{z_{pk}}{l_e^2} \tag{4.22}$$

is the force in equation 4.3 produced on the end of the cantilever by the magnetic tip-field interaction given by equation 4.2, where z_{pk} is the peak oscillation amplitude

of the cantilever. Combining equations 4.20, 4.21, and 4.22 and solving for moment yields

$$\mu_{min} = \frac{(SNR)l_e^2}{Bz_{pk}} \left(\frac{4kk_BT\Delta\nu}{\pi Q f_0} \right)^{1/2} \tag{4.23}$$

where μ_{min} is the minimum detectable magnetic moment given a required (SNR) and B is the uniform externally applied field. According to equation 4.23, sensitivity can be increased by increasing external field, cantilever oscillation amplitude, cantilever quality factor, and resonant frequency and decreasing temperature, bandwidth, cantilever spring constant, and effective length. It should be noted, however, that cantilever resonant frequency and spring constant are related through equation 4.9 such that increasing one, in general, increases the other. In addition, increasing the effective length of the cantilever, in general, decreases the cantilever spring constant and resonant frequency. To decouple some of these relationships it is useful to express the resonant frequency and spring constant of the cantilever in terms of basic physical cantilever parameters. Spring constant can be expressed in terms of cantilever physical parameters as

$$k = \frac{Et^3w}{4l^3} \tag{4.24}$$

for a beam cantilever, where E is Young's modulus of elasticity and l, w, and t are the cantilever length, width, and thickness, respectively. Cantilever mass m can then be expressed as

$$m = \rho lwt \tag{4.25}$$

where ρ is mass density of the cantilever material. It should be noted that the mass used to subtitute into equation 4.9 should actually be the effective mass of the cantilever, taking into account the distribution of mass along its entire length.

This would be the equivalent mass at the end of the cantilever resulting in the same frequency as the mass distribution rather than the actual mass of the cantilever. Equation 4.25 is, therefore, a simplification and will undoubtedly introduce some error into the calculation but, nevertheless, should provide some first-order insight into sensitivity maximization. Combining equations 4.9, 4.24, 4.25, and 4.23 yields

$$\mu_{min} = \frac{l^{3/2} t w^{1/2} (E\rho)^{1/4} (2k_B T \Delta\nu)^{1/2} (SNR)}{z_{pk} B (\pi Q)^{1/2}} \tag{4.26}$$

where μ_{min} is expressed in terms of basic cantilever parameters. Note that actual cantilever length l and effective length l_e have been combined into one quantity here. Although this will also produce some error in the equation both quantities are nearly equal (related by a constant of proportionality close to 1) so no qualitative insight offered by the equation is lost. According to this expression we can make the initial conclusion that smaller, lighter, and softer cantilevers maximize sensitivity, although because of material constraints E and ρ are not generally parameters that fabricators have much control over. In general, though, this expression can be helpful for choosing a cantilever that will maximize measurement sensivitiy in both equations 4.23 and 4.26 and providing insight into experimental procedures that can increase sensitivity such as generating higher fields, operating at cryogenic temperatures, increasing cantilever excitation and, therefore, oscillation amplitude, increasing signal averaging time, and increasing cantilever Q through fabrication procedures and materials and operation at low vacuum.

The calculated sensitivity limit of the room temperature magnetometer used in this research using low noise commercially available cantilevers is around 4×10^{-17} J/T. This calculation is for the smallest triangular cantilever (assuming a Q of 10000) on a Veeco (model # MLCT-NONM) SiN cantilever chip (same chip containing the

large triangular SiN cantilever used for some of the data presented here). This smaller cantilever cannot be used in the current magnetometry setup due the incompatibility of its high resonant frequency with the digital sampling board used. The only SiN cantilever used thus far in the research has been the largest triangular cantilever; see figure 2.6). Its sensitivity limit is 3×10^{-16} J/T. Using ultra-soft silicon cantilevers obtained from Dan Rugar's research group at IBM Almaden Research Center, the room temperature magnetometer used for the research presented here has a current predicted sensitivity limit of 5×10^{-18} J/T. This is assuming a unity signal-to-noise ratio and a cantilever Q of 7000. Table 4.2.4 shows some nominal physical properties and the magnetometry sensitivity limit of four different cantilevers used in (or readily available to) our research group. The calculated sensitivity is based on a temperature of 300 K, available external field of 0.5 T, bandwidth of 1 Hz, oscillation amplitude of 300 nm and unity signal-to-noise ratio. The value of Q was chosen for each cantilever to reflect a typical (mid to upper range) value based on previous measurements. The cantilevers in the second row (Si model # MPP-32100), third row (SiN model # MLCT-NONM, largest triangular cantilever), and fourth row (SiN model # MLCT-NONM, smallest triangular cantilever) of table 4.2.4 are all manufactured by Veeco Probes [2]. See the caption of table 4.2.4 for referral to images of each Veeco cantilever. Although our instrument is not capable of higher magnetic fields or cryogenic temperature operation, by reducing the temperature to 4 K, increasing magnetic field to 6 T, and using a cantilever with a low-temperature Q (at 4 K) of 20000, the sensitivity is increased to around 3×10^{-20} J/T for the IBM ultra-soft silicon rectangular cantilever. This is comparable to the sensitivity of the low temperature magnetometer described in [19], which was claimed to be better than 10^4 μ_B or 9×10^{-20} J/T.

Cantilever	μ_{min} (J/T)	Q	f_0 (kHz)	k (mN)	l (μm)	l_e (μm)	t (μm)
A-Si	5×10^{-18}	7000	2	0.12	90	65	N/A
B-Si	5×10^{-16}	100000	10	100	450	326	2.0
C-SiN	3×10^{-16}	10000	7	10	320	250	0.6
D-SiN	4×10^{-17}	10000	120	500	85	66	0.6

Table 4.1: Various properties for three cantilevers used in MRFM research. The minimum detectable moment (in torque magnetometry measurements) is based on a temperature of 300 K, available external field of 0.5 T, bandwidth of 1 Hz, oscillation amplitude of 300 nm and unity signal-to-noise ratio. Q values for each cantilever were chosen to be in the practial upper range of experimental values. Cantilevers are as follows: A - IBM ultra-soft Si; B - Veeco Si Rectangular (model # MPP-32100), figure 2.7; C - Veeco SiN (model # MLCT-NONM) Largest Triangular, figure 2.6 blue arrow; D - Veeco SiN (model # MLCT-NONM) Smallest Triangular, figure 2.6 rightmost cantilever.

More information about mechanical quality factor (Q), in general and as it pertains to the four cantilevers discussed above, can be found in sections 4.3.3 and 2.2.5.

4.3 Characterization Via Cantilever Magnetometry

As mentioned previously, characterization of small micron and submicron ferromagnetic particles can be accomplished with extreme sensitivity through the use of the cantilever magnetometer. This, combined with the relatively low cost of operation has made the cantilever magnetometer the primary instrument for characterizing MRFM probes before experimental use. The instrument presented in this research and used for the measurements discussed later is commonly used to characterize probes for ESR, NMR, and FMR expiriments. This section will first give a detailed description of the custom built magnetometer used here, then describe procedures for measuring cantilever Q and oscillation amplitude. Experimental noise limits and frequency drift

will then be discussed and, finally, some particle measurements of interest obtained using this instrument will be presented and discussed.

4.3.1 Description of the Instrument

The magneometer discussed here is a room temperature, high vacuum, cantilever magnetometer. The magnetic field is supplied by a water-cooled 0.5 T (5000 G) magnet. The magnetic poles of the magnet are spaced approximately 3 inches apart. The magnet's pole spacing is adjustable, however, decreasing the pole spacing to produce higher magnetic fields is not practical in this setup due to space requirements. The cantilever position is detected using a fiber optic interferometer. The laser wavelength for the interferometer is 1550 nm. Cantilever excitation is accomplished by applying an AC voltage at the cantilever resonant frequency to a 0.250" diameter x 0.100" thick piezoelectric disc. This disc is driven through a gain-controlled positive feedback loop from the interferometer, which allows the cantilever excitation to track the resonant frequency of the cantilever. The inteferometer signal is sent into a computer through a digital signal processing board. Once digitized, a frequency measurement is applied to the signal and digital control is implemented for the feedback loop. An similar approach for frequency measurement is described in [59]. Vacuums lower than 0.4 mTorr are obtained using a turbo pump. The instrument rests on several vibration isolation pads in order to reduce acoustic noise coupled to the instrument from outside sources.

One of the most difficult tasks required to operate this instrument is fiber-cantilever alignment. Each cantilever must be manually aligned with the optical fiber with both precise lateral positioning and fiber-cantilever separation. The optical fiber consists

of a flexible outer covering, a middle layer made of glass, and a core through which the infrared light passes. This core is only about 10 μm in diameter, and typical cantilever widths vary from 20-30 μm at the free end, requiring extreme precision during alignment.

The alignment stage used when my work on the magnetometer first began is shown in figure 4.3. A small copper leaf spring was used to apply the pressure required to

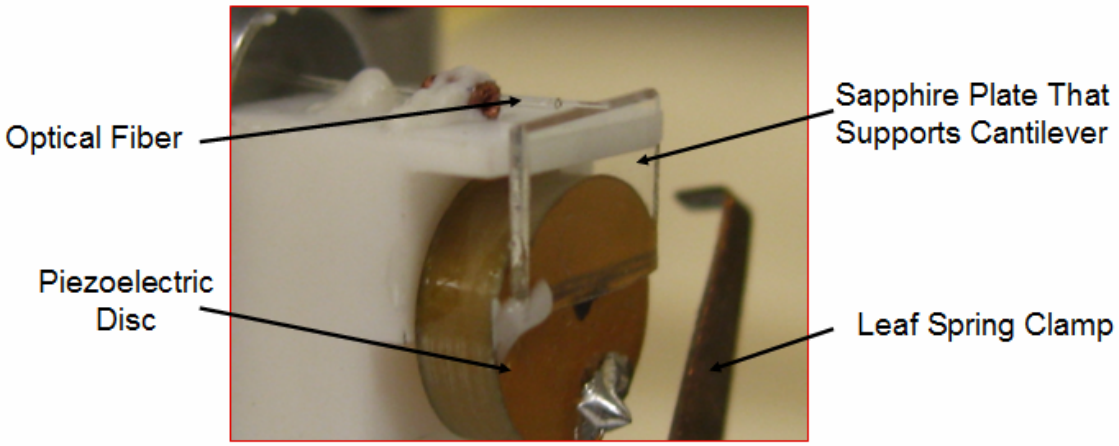

Figure 4.3: Photograph of the original fiber-cantilever alignment stage of the cantilever magnetometer

hold the cantilever in place. This leaf spring was held between two peices of teflon using two 4-40 cap screws. The cantilever had to be position manually using tweezers and then secured in place by tightening the cap screws, which applied pressure on the copper clamp. Becuase the alignment was completely manual extreme coordination, steadiness of hand, patience, and time was required. The alignment procedure is conducted under an optical microscope. One of the main problems with this system was that the optical fiber was permanently glued in place with respect to the sapphire

plate on which the cantilever chip rested. As a result, there was no adjustment in the fiber-cantilever spacing, which is rather critical for the low coherence length laser used in the setup. When a new cantilever was to be measured it was often discovered that the fiber-cantilever seperation was not suitable (due to varying cantilever chip thicknesses) and the fiber had to be repositioned and reglued. Repositioning the fiber required the fiber to be broken, the cladding to be stripped off, the fiber to be cleaved, and the fiber to be reglued in the proper position. This process usually required several hours of work. In addition, because the alignment procedure required precise manipulation with tweezers, there was always a high risk that the cantilever chip would be mishandled and the cantilever would break. One of the tasks I set out to accomplish during my research was to design and implement a new fiber-cantilever alignment stage that was easier to use and more versatile than the one previously in operation.

There were three main objectives in my fiber-cantilever alignment stage design. The first was to allow the fiber-cantilever separation to be adjustable so that cantilevers with different chip thicknesses could be measured without regluing the optical fiber. The second was to reduce the risk of damaging the cantilever during the process of alignment. The third was to speed up the process of aligning the cantilever with the fiber. The result was the design shown in figure 4.4. In this design the optical fiber is first glued into a glass ferrule using Stycast®1266 epoxy. The glass ferrule is then glued inside a stainless steel cylindrical sleeve (shown in red) using Torr Seal epoxy (manufactured by Varian). The stainless steel sleeve was actually designed by Dan Rugar's group for a similar purpose at the IBM Almaden Research Center. The metal sleeve (and, therefore, fiber) is held in place by a set screw, allowing the fiber to

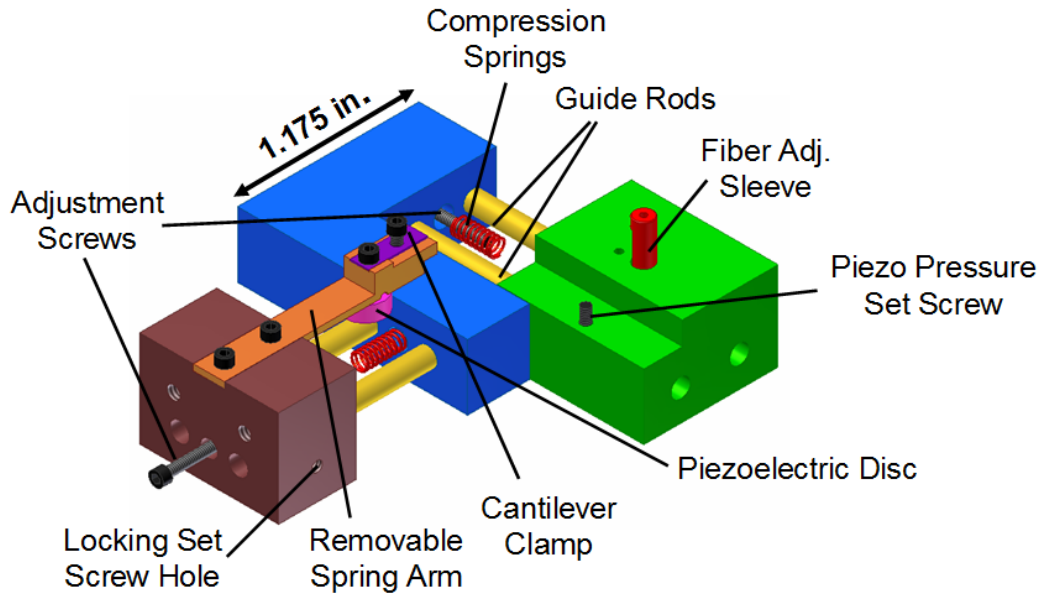

Figure 4.4: Exploded computer drawing of the most recent fiber-cantilever alignment stage design for the room temperature cantilever magnetometer.

be placed in relation to the cantilever with any spacing desired. The cantilever lateral position can be adjusted with extreme precision using 0-80 cap screws (all shown in black). Two cap screws provide motion in two orthogonal directions. Each direction of motion is guided by two stainless steel pins (shown in yellow). Back pressure for each direction of movement is provided by an internal compression spring (shown in red). Once the desired lateral postition is achieved, one of the slide pins for each direction of movement is locked in place using a set screw. The cantilever is held in place on a removable leaf spring arm (shown in orange) in a slightly depressed slot by means of a small removable leaf spring cantilever clamp (shown in purple). Glued to the bottom of this leaf spring is the piezoelectric disc (shown in pink) used for cantilever excitation. Pressure is applied to the bottom of this disc by a set screw attached to the block (shown in green) holding the metal fiber sleeve. With this

new system cantilever lateral positioning is greatly facilitated by the use of high resolution screw adjustment. The fiber-cantilever separation can be easily adjusted by repositioning the metal fiber sleeve. Finally, the arm that holds the cantilever can be removed allowing the cantilever to be safely clamped in position before any alignment procedures begin. The entire alignment stage is secured to a platform via the brown block using two cap screws. This platform is then attached to four rods suspended from the bottom of a vacuum flange. The new alignment stage design resulted in a significant decrease in the amount of time needed to take a measurement, fewer accidents involving cantilever damage, and less required optical fiber regluing. Since the positioning of the fiber during gluing is not nearly as critical for the new design, if regluing is required the process is much simpler and faster.

4.3.2 Measuring Cantilever Oscillation Amplitude

Like cantilever quality factor, knowing the oscillation amplitude is not necessary for magnetometer measurements of a magnetic particle. It is, however, important when assessing sensitivity, because sensitivity depends directly on oscillation amplitude. The review of optical interferometry given in section 2.2.1 is helpful for understanding the following discussion. The first step when using the interferometer is to adjust the light wavelength by heating or cooling the laser diode until the cantilever equilibrium position is centered on a point of maximum destructive interference. This results in a relationship between position change and light amplitude that is nearly linear for small cantilever oscillations. For oscillation amplitudes smaller than 1/8 of the wavelength of light used in the interferometer, the response from the interferometer detector appears as an approximate sine wave following the position of the

cantilever. This is because the cantilever's position changes with time in a sinusoidal fashion and the cantilever position has a nearly linear relationship with the interference dependent light amplitude. In order to calibrate the interferometer to obtain oscillation amplitude, the cantilever must first be driven to the points of maximum constructive interference and then centered between these two points. When the cantilever oscillations begin to extend beyond these points of maximum light amplitude a high frequency component will be visible in the oscilloscope signal. The points of maximum light amplitude are spaced one half of the laser wavelength apart so the amplitude of oscillation of the cantilever is one quarter of the wavelength of the laser when driven these points. Because the position response of the piezo and cantilever are fairly linear with applied piezo voltage, one can then just scale the oscillation amplitude with the drive voltage applied to the piezo. This is generally a good first order approximation.

For more accuracy, one can observe the decrease in oscilloscope oscillation amplitude and fit this decrease to the sinusoidal interference pattern. The response of (signal from) the detector can be modeled as

$$V = C_1 \sin\left(\frac{2\pi z_c}{\lambda}\right) + C_2 \tag{4.27}$$

where C_1 is a constant of proportionality, z_c is the oscillatory position of the cantilever, λ is the wavelength of the laser, and C_2 is the DC level of the detector. C_1 can be found by observing the response when the cantilever is centered between and driven to the points of maximum light amplitude and C_2 is easily determined by observing the DC level of the detector. The resulting relationship can then be solved for z_c given an offset sinusoidal voltage signal from the detector.

4.3.3 Measuring Cantilever Quality Factor

As discussed in section 2.2.5 and 4.2.4, cantilever quality factor plays a major role in both MRFM sensitivity and magnetometer measurement sensitivity. Sensitivity has an inverse square root dependence on quality factor as shown in equations 2.21 and 4.23. The Q of a cantilever is easily measured in the cantilever magnetometer by observing the cantilever ring-down transient occurring after cantilever excitation is abruptly stopped [16]. The Q of the cantilever is given by

$$Q = \pi \tau_0 f_0 \tag{4.28}$$

where f_0 is the cantilever resonant frequency and τ_0 is the time constant of the exponential decay of the cantilever oscillation amplitude. τ_0 can be found by fitting the cantilever ring down transient (envelope) to an exponential decay. Although this parameter is not necessary for measurements of magnetic properties of a particle it is necessary for determining the ultimate sensitivity for a given cantilever and evaluating the noise level from results obtained during measurements. Table 4.3.3 shows room temperature quality factors for 6 different Veeco silicon rectangular cantilevers (Model # MPP-32100) organized from lowest to highest Q. These quality factors were measured using the ringdown technique discussed above in the room temperature magnetometer. Cantilever frequency is included to give some indication of variability of properties between identical cantilever models. The air pressure during the measurement is also shown. Cantilever Q is inversely proportional to air pressure because air friction leads to damping, however, variability of the air pressure within the range shown for the measurements in table 4.3.3 should have little effect on the corresponding quality factors [16]. In fact, below about 1 mTorr the quality factor

Quality Factor	Resonant Frequency (Hz)	Measurement Pressure (mTorr
7700	13861	0.35
24000	10323	1.14
55000	17469	0.61
61000	15612	1.57
110000	17036	0.47
140000	12368	0.84

Table 4.2: Room temperature quality factors, resonant frequencies, and measurement pressures for 6 different Veeco (model # MPP-32100) silicon rectangular cantilevers. Frequency and Q measurements were conducted using a custom built room temperature cantilever magnetometer.

is relatively independent of air pressure [16]. The full range of quality factors for various MRFM and magnetometry cantilevers at pressures below 1mTorr can extend from 500 to 200000 [10, 14, 15, 16, 19, 20, 24, 27]. One can see from table 4.3.3 that even for the same type of cantilever Q varies over a large range between individual cantilevers; much larger, in fact, than other parameters such as frequency and spring constant. This is one reason why it may be necessary to characterize the cantilever before use in an experiment, especially when maximum sensitivity is required. Results of Q measurements in [16] show less variability in the quality factors of their custom fabricated silicon nitride and single crystal silicon cantilevers. This may be a result of more consistent fabrication procedures than those used in the fabrication of the Veeco single-crystal silicon cantilevers. The single cyrstal silicon cantilevers studied in [16] were in the thickness range of 60-240 nm compared to the 2 μm thickness of the Veeco single crystal silicon cantilevers measured here, so the increased variability

in quality factors of the cantilevers measured here may also be a direct result of the increased thickness. For more details on cantilever quality factor see section 2.2.5.

4.3.4 Experimental Noise Measurements

One area of great interest when assessing the performance of the magnetometer is a comparison between theoretical and experimental sensitivity limitations. The sensitivity of the cantilever magnetometer should, ultimately, be limited by the intrinsic thermomechanical vibrations of the cantilever [14, 15, 16, 19]. These vibrations are discussed in detail in sections 4.2.4. They appear as noise in the frequency measurement performed by the magnetometer. The force noise (RMS value) generated by a particular cantilever can be described by equation 4.20. This force noise can be converted into an effective noise variation in the cantilever spring constant given by

$$k_n = \frac{F_n}{z_{pk}} \tag{4.29}$$

where z_{pk} is the peak oscillation amplitude of the cantilever. The frequency noise is related to the effective spring constant noise by

$$f_n = f_o \left(\frac{k_0 + k_n}{k_0} - 1 \right) \tag{4.30}$$

where f_n is the frequency noise generated by thermal cantilever vibrations, f_0 is the cantilever's resonant frequency, and k_0 is the cantilever spring constant. Assuming that $k_n \ll k_0$, equation 4.30 simplifies to

$$f_n = \frac{k_n f_0}{2k_0} \tag{4.31}$$

Substituting equations 4.20 and 4.29 into equation 4.31 yields the RMS frequency noise

$$f_n = \frac{f_0}{2k_0 z_{pk}} \sqrt{\frac{2k k_B T \Delta\nu}{\pi Q f_0}} \tag{4.32}$$

The noise level from the frequency drift data shown in figures 4.6 and 4.7 was compared to the theoretical noise limit given in equation 4.32. The cantilever Q, measured using the ringdown technique discussed in section 4.3.3, was found to be about 7700. The oscillation amplitude was set at about 85nm, using the procedure described in section 4.3.2. Using these parameters, the theoretical RMS frequency noise was calculated to be about 0.0013 Hz. This was slightly lower than the experimental value of about 0.0035 Hz. The discrepency could be the result of error in some of the values used in the calculation, particularly spring constant, which was not measured. Spring constant is supplied by the manufacturer of the cantilever, but the manufacturer's tolerance is between 0.05 and 0.2 N/m with a nominal value of 0.1 N/m. The higher experimental noise could also be the result of acoustic noise coupled into the instrument from the vacuum pump or from other noise sources throughout the building.

4.3.5 Frequency Drift

One of the problems encountered with the room temperature magnetometry studies in this research was a significant cantilever resonant frequency drift that degraded the accuracy and viability of small moment measurements. Although some frequency drift was observed with the original (old) alignment stage (see figure 4.5), the rate of drift seemed to be even higher with the new alignment stage design. The implementation of the new alignment stage also coincided with a move of the instrument to a new building so it is not entirely clear if the frequency drift is related to the new alignment stage or another variable that changed with the building. Figure 4.6 shows cantilever frequency drift vs. time for a silicon Veeco (model #MPP-32100) cantilever

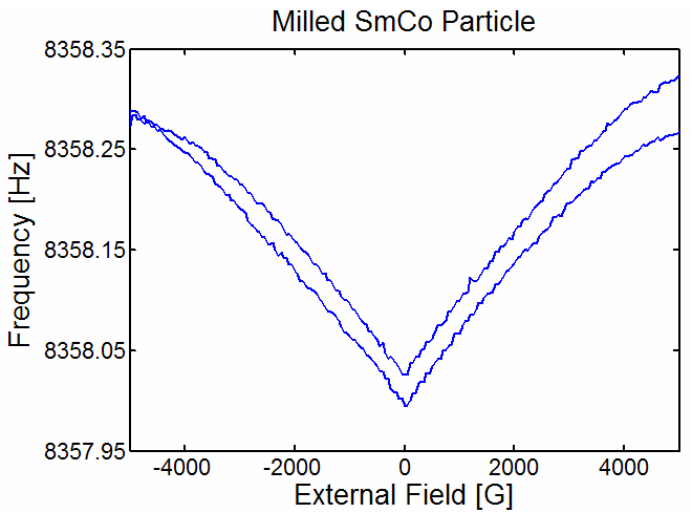

Figure 4.5: Magnetometer measurement of a low-coercivity magnetic particle using the initial original alignment stage. The measurement started at +5000 G so the frequency difference between the two plotted points at 5000 G show the freqeuncy drift over one loop.

like that pictured in figure 2.7. The data in figure 4.6 was taken with the chilled water supply for the magnet on but no external magnetic field applied. This plot shows frequency drifts as high as 0.0024 Hz/min. This can seriously impede measurements of small particles where expected frequency shifts approach the amount of frequency drift occuring over the duration of the measurement. Obviously, the longer the measurement takes, the more frequency drift will affect the results. This is an important consideration during measurements because smaller field sweep steps, although giving more resolution and accuracy to the hysteresis curve, also result in longer measurement times and more overall frequency drift.

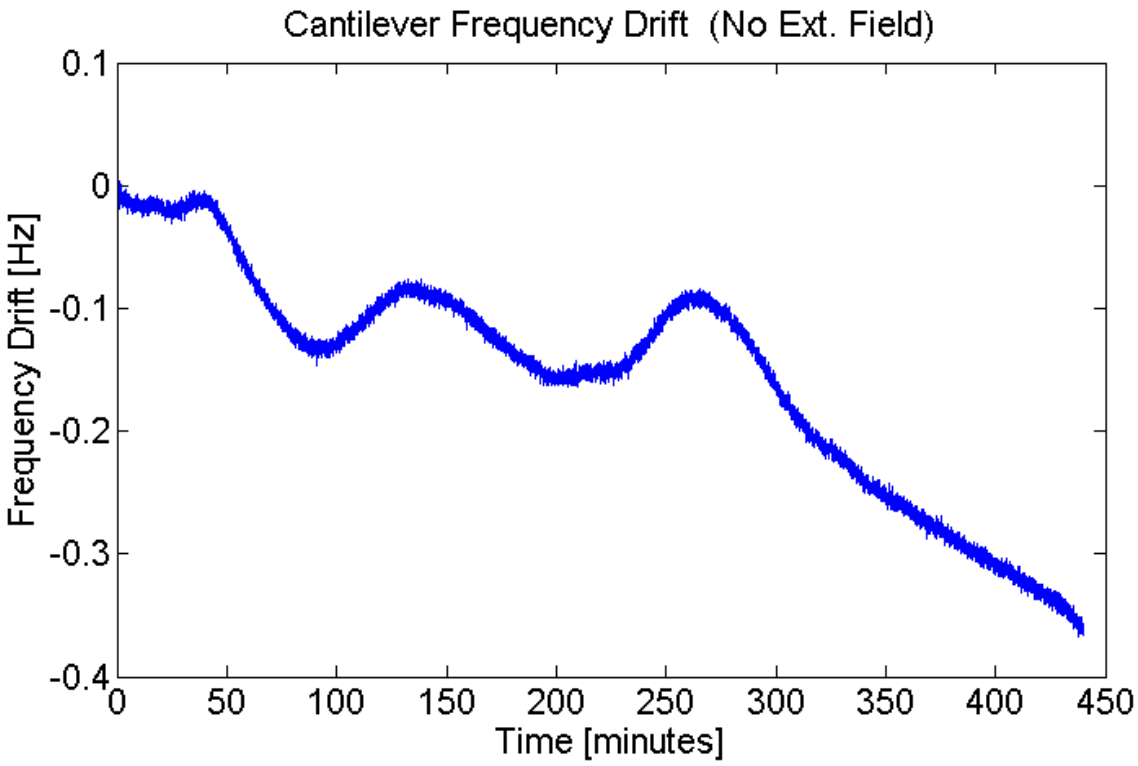

Figure 4.6: Silicon cantilever frequency drift measurement. The measurement was taken with the original stainless steel alignment stage support rods still in place and the chilled water on.

Since frequency drift has not been well-documented in magnetometry at cryogenic temperatures it appears as though the frequency drift experienced by the room temperature magnetometer is related to some sort of temperature instability of the cantilever. It was initially hypothesized that temperature drift in the new closed-circuit chilled water supply was responsible for the increased freqeuency drift observed after the new aliginment stage was implemented. Although the chilled water supply may indeed result in some temperature drift, data shown in figure 4.7, taken after the chilled water had been shut off for several weeks, shows that there is still significant frequency drift. In addition, the data in figure 4.7 was also taken after the original

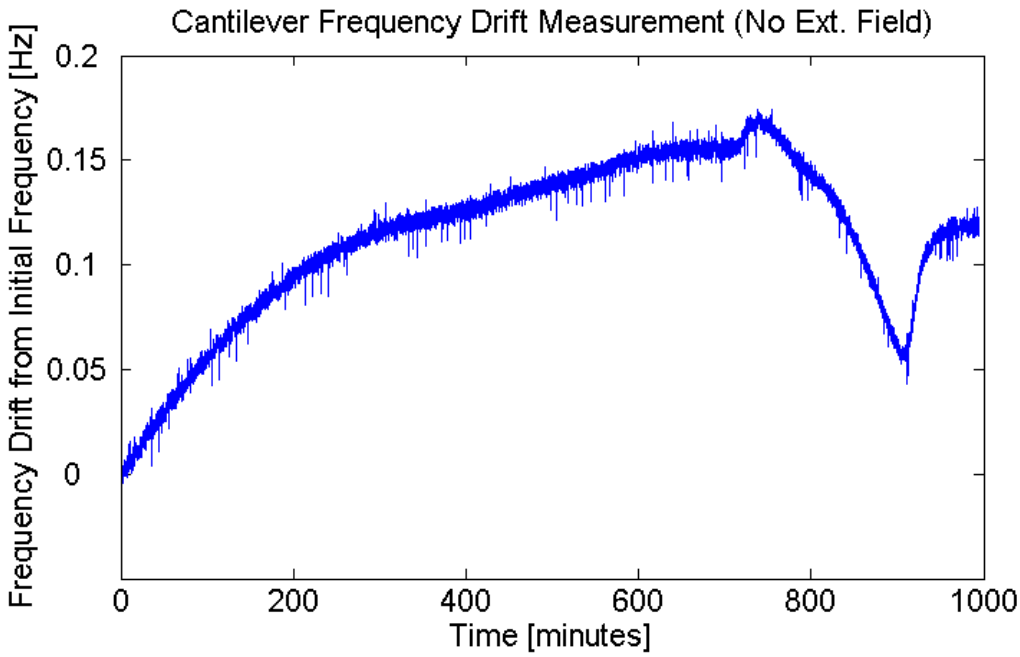

Figure 4.7: Cantilever frequency drift measurement using the same Silicon cantilever from figure 4.6. This data was taken after replacing the original stainless steel alignment stage support rods were replaced by G10 rods. The chilled water had been turned off for several weeks before this measurement was taken.

stainless steel rods supporting the alignment stage were replaced with G10 temperature insulating rods. These rods have a thermal conductivity around 30 times less than the 316 stainless steel used in the original rods [60]. It was hoped that the new support rods would slow down any temperature drift to a time scale much longer than the desired measurement time of 10-60 minutes. Except during the initial cool down occurring when the chilled water is first turned on, there was no real discernable difference in frequency drift measurements between water off and water on conditions or between the stainless and G10 support rods. In the future, a temperature monitored and, if necessary, temperature controlled alignment stage may be implemented

to determine with greater certainty if frequency drift is a result of temperature drift. Procedures to subtract frequency drift out of the measurements have been successfuly implimented. These will be discussed in more detail in section 4.3.6

4.3.6 Frequency Drift Subtraction

As discussed later in section 4.3.5, frequency drift is one problem that has been encountered during room temperature magnetometer measurements. Figure 4.8 shows a characteristic magnetometer measurement of a focused ion beam milled Sm_2Co_{17} particle (particle (1) in table 4.3.7) on a Veeco (model # MPP-32100) silicon cantilever. An SEM micrograph of the particle is shown in figure 4.9 This measurement

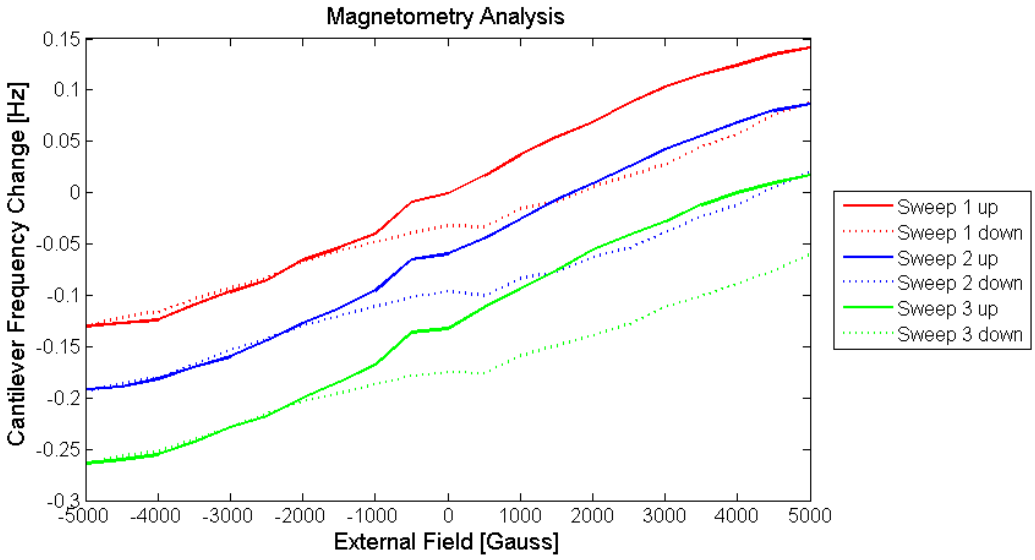

Figure 4.8: Magnetometer measurement of a focused ion beam milled Sm_2Co_{17} particle.

consisted of 3 sweeps from 5000 G to -5000 G and back again. Ideally each sweep should follow an identical path, however, one can easily see that there is a downward

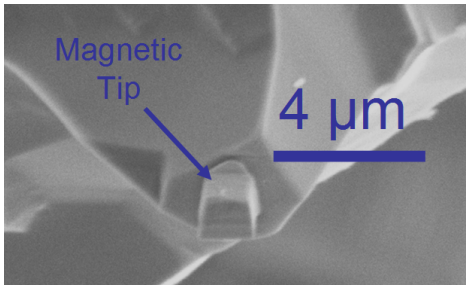

Figure 4.9: SEM micrograph of the focused ion beam milled Sm_2Co_{17} particle from the measurement in figures 4.8, 4.10, and 4.11.

frequency drift that seperates each sweep. Each sweep took about 4 minutes and the average frequency drift per sweep was about 0.05 Hz. The results is a frequency drift of about 0.012 Hz/min.

The first step taken to eliminate the frequency drift from the data was to align each sweep so that they all had the same first zero field frequency point. The results of this shift of the curves is shown in figure 4.10. One can now see that the curves overlap much more closely, but there is still frequency drift visible during each individual sweep. The final step was to subtract out the average frequency drift between each point on the plot. This alteration resulted in the plot shown in figure 4.11. One can now see that each sweep overlaps nearly perfectly and that the begining and end points of each sweep are nearly coincident. This is the result one would expect from a measurement with no frequency drift. This result also shows that the frequency drift during each individual sweep is nearly constant. This is probably a reasonable approximation for most measurements that occur on a similar time scale. If frequency sweep was not constant during each sweep the three sweep curves would not overlap after a linear correction procedure was applied.

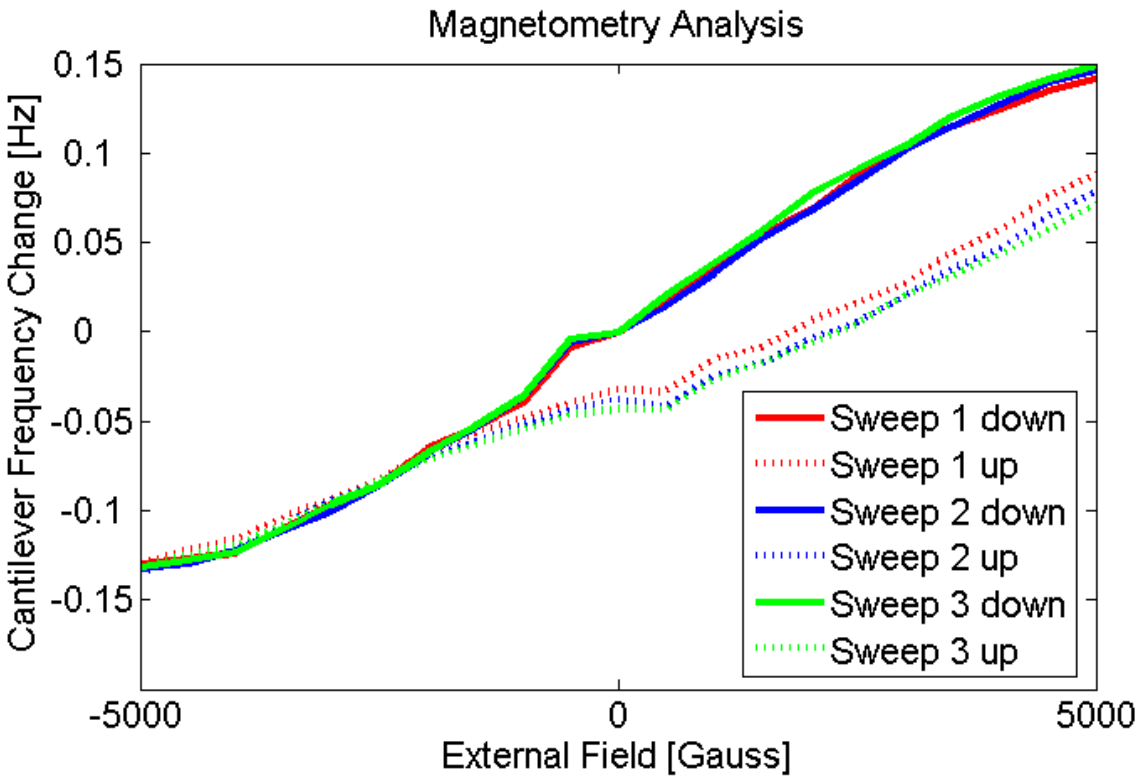

Figure 4.10: Magneometer measurement of figure 4.8 with frequency drift correction made to align the first zero-frequency points of each curve.

4.3.7 Particle Measurements and Results

In this section actual results obtained from particles measured with the magnetometer will be displayed and discussed. The particles chosen each display a characteristic or effect, of interest not only to MRFM research, but to the physics community in general. Unless stated otherwise, all measurements are assumed to have been taken using the new magnetometer alignment stage design discussed in section 4.3.1. Also, unless stated otherwise, all particles discussed below have been fully saturated in a 9 T magnet before measurement. Table 4.3.7 summarizes the measured properties of all

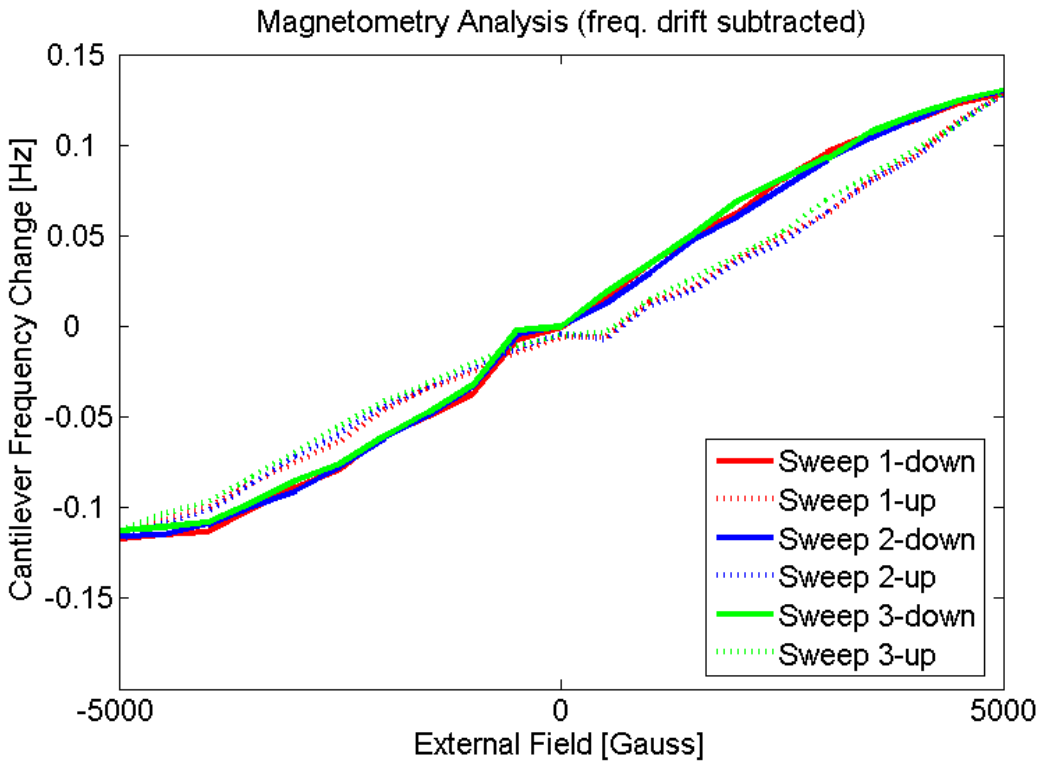

Figure 4.11: Same magneometer measurement of a coercive Sm_2Co_{17} particle (see figure 4.9 for SEM image) as in figures 4.8 and 4.10 with frequency drift correction made between successive points on the plot based on average frequency drift during each sweep. $\mu = 6.6 \times 10^{-13}$ J/T

the particle discussed below. These properties include magnetic moment (μ), coercive field ($\mu_0 H_c$), effective radius (R_e), and effective volume (V_e). If particle coercivity is higher than 0.5 T then its value cannot be measured with this instrument so it will not be shown in the table.

Particle/Material	μ (J/T)	$\mu_0 H_c$ (G)	R_e (μm)	V_e (μm^3)
(1) - Sm_2Co_{17}	2.1×10^{-11}	N/A	1.8	24
(2) - Sm_2Co_{17}	6.6×10^{-13}	N/A	0.56	0.72
(3) - $Nd_2Fe_{14}B$	1.8×10^{-12}	2200	0.77	2.0
(4) - Sm_2Co_{17}	5.5×10^{-13}	500	0.52	0.60
(5) - Sm_2Co_{17}	5.0×10^{-13}	N/A	0.51	0.54
(6) - Sm_2Co_{17}	1.3×10^{-13}	< 200	0.32	0.14

Table 4.3: Summary of magnetic properties from the six ferromagnetic tip magnetometry measurements shown and discussed in section 4.3.7. More information about each tip can be found by reading under the six subheadings of section 4.3.7 corresponding to each of the six tips.

Large Coercive Sm_2Co_{17} Particle (1)

Figure 4.12 shows a standard magnetometer measurement of a large FIB milled (see section 3.4) coercive Sm_2Co_{17} particle glued to the end of a Veeco silicon cantilever. This measurment was taken using the original (older) alignment stage design discussed in section 4.3.1. The SEM micrograph of this magnetic particle on the cantilever is shown in figure 4.13. Using equation 4.12, the calculated magnetic moment of the particle in figure 4.13 was approximately 2.1×10^{-11} J/T. One can see that the correlation between frequency and external field is nearly independent of the direction of the external field. This indicates that the particle has a coercive field that is larger than the applied field in the measurement and that within the range of applied field the moment is nearly constant. In order to validate the magnetic moment measurement, the effective radius of the particle can be compared to the dimensions visible in the SEM micrograph of figure 4.13. The effective radius for this particle is 1.8 μm

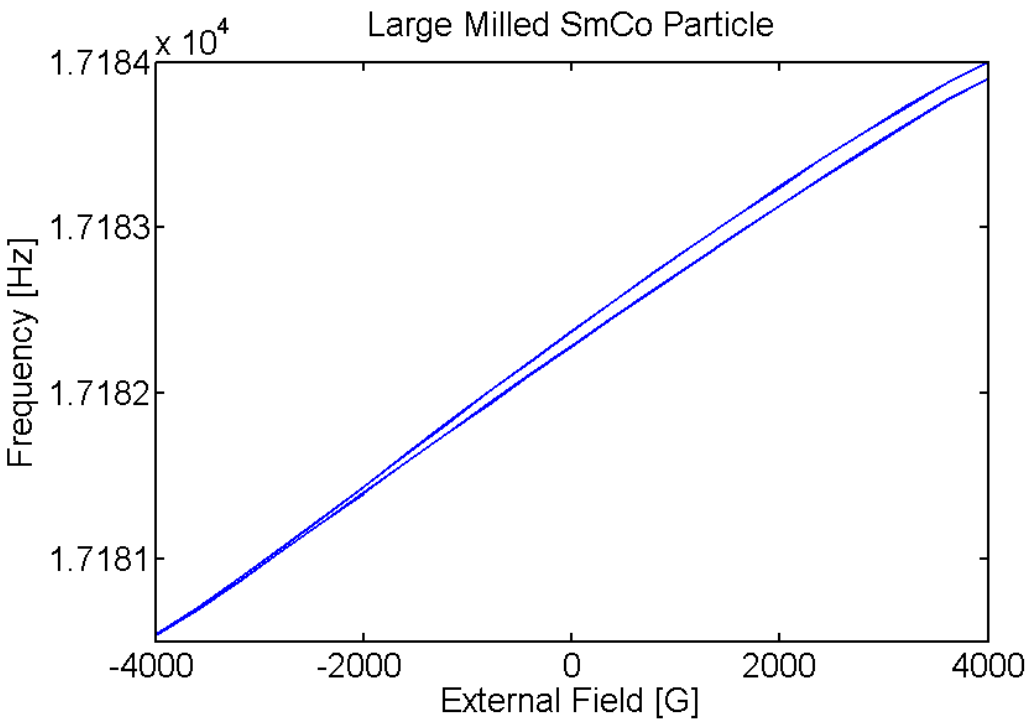

Figure 4.12: Magnetometer measurement of a large coercive Sm_2Co_{17} particle (see figure 4.13). $\mu = 2.1 \times 10^{-11}$ J/T

and is calculated from

$$R_e = \left(\frac{3\mu}{4\pi M_s}\right)^{1/3} \tag{4.33}$$

where μ is the magnetic moment of the particle and $M_s = 9.18 \times 10^5 A/m$ is the approximate saturation magnetization of Sm_2Co_{17} and $Nd_2Fe_{14}B$. The effective radius is defined here as the radius of a uniformly magnetized sphere with saturation magnetization M_s, possessing a magnetic moment μ. The saturation magnetization of Sm_2Co_{17} is only slightly different from $Nd_2Fe_{14}B$, but not enough to overcome the overall error in the calculation due to the other uncertainties, so the same value of saturation magnetization will be used for both magnetic materials. One could also

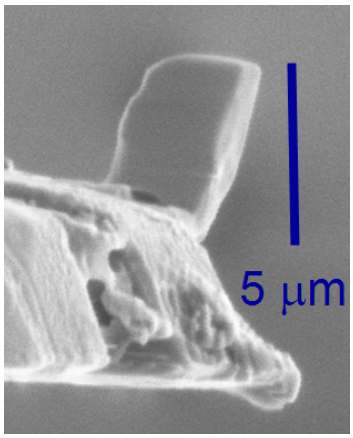

Figure 4.13: SEM micrograph of the Sm_2Co_{17} particle from the measurement in figure 4.12.

refer to an "effective volume" for a particle calculated as

$$V_e = \frac{4\pi R_e^3}{3} \tag{4.34}$$

The effective volume for the particle of figures 4.12 and 4.13 is 24.4 μm^3. This corresponds well with the actual particle volume as estimated by the SEM image of the particle in figure 4.13.

There is almost no visible noise in this measurement. The reason for this is that the scale of the frequency shift resulting from such a large magnetic moment is much larger than the noise level of the cantilever. There is a frequency drift of approximately 0.1 Hz that is visible from the begining to the end of the measurement. Althought this drift is minimal on the frequency shift scale of this measurment, it could be significant for a much smaller particle. It should also be noted, however, that this measurement took much longer than measurements of smaller particles conducted using the new alignment stage. This longer measurement resulted from 100 G field sweep steps instead of the usual minimum of 500 G for the new alignment stage. The

larger frequency drift experienced with the new stage has limited the temporal length of measurements and therefore the available field sweep resolution.

Sm_2Co_{17} Particle (2)

The next particle measurement to be discussed is the measurement of a milled coercive Sm_2Co_{17} particle on a Veeco silicon cantilever. The magnetometry measurement (after the frequency drift subtraction discussed in section 4.3.6) is shown in figure 4.11 in section 4.3.6. An SEM micrograph of this picture is shown in figure 4.9 in section 4.3.6. An analysis of the data shown in figure 4.11 indicates a coercive magnetic moment of approximately 6.6×10^{-13} J/T. This corresponds to an effective particle radius of about 0.56 μm and effective volume of about 0.72 μm^3, which is in good agreement with the SEM image in figure 4.9. The area of overlap between the upward and downward portion of each curve indicates a strange behavior that would probably be dismissed as some sort of error, were it not for the repeatability of the loops. For a typical magnetometry hysteresis behavior of a low coercivity particle see section 4.3.7.

Low-Coercivity Particle (3)

Figure 4.14 shows a magnetometer measurement (with frequency drift subtracted) of a ≈ 2 μm diameter unmilled $Nd_2Fe_{14}B$ sphere glued to the end of a SiN Cantielver. The measurement in figure 4.14 was taken before this particle was saturated in the 9 T magnet. The measurement in figure 4.14 consisted of three field sweep loops from -5000 G to 5000 G and back with 500 G steps. One can easily see that the upward and downward sweep portions of each curve do not overlap. This feature is a result of the low coercivity of the particle. The area between the curves is analogous to the

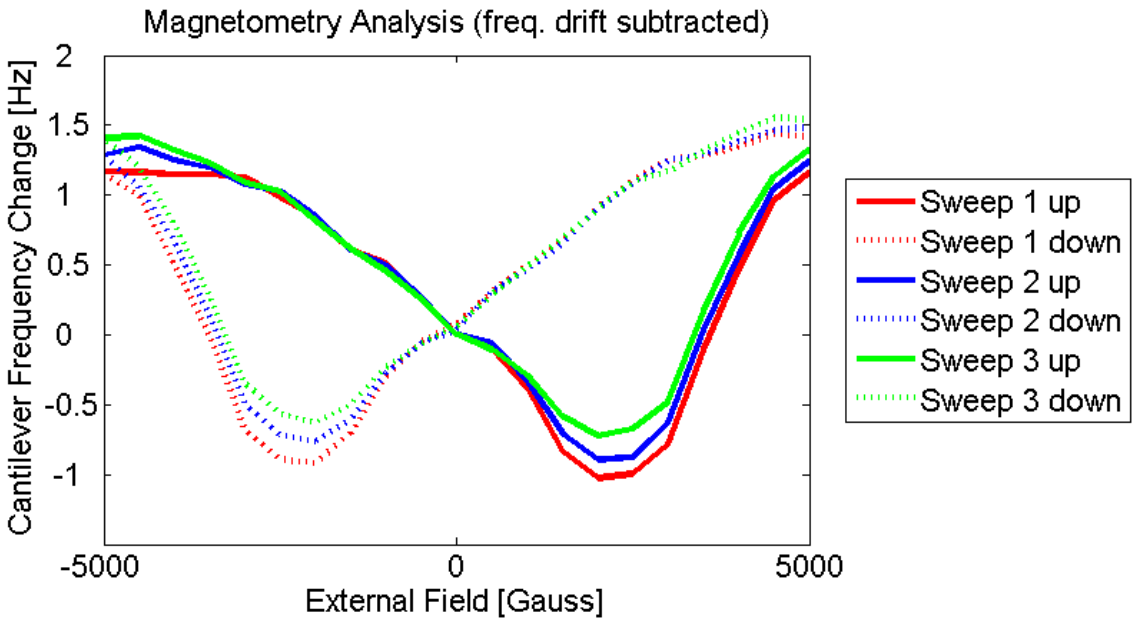

Figure 4.14: Magnetometer measurement of a low-coercivity $Nd_2Fe_{14}B$ sphere before saturation. $\mu = 1.8 \times 10^{-12}$ J/T

area between the curves in a hysteresis loop. The point at which the slope of the curves becomes zero is the coercive field (switching field) of the particle, which for this particle is around 2200 G. If enough external field is applied even high coercivity particles will exhibit the curve shape shown in this measurement. Based on the slope of the curve and frequency shift between 0 and 2000 G the magnetic moment was calculated to be 1.8×10^{-12} J/T. This results in an effective particle radius of about 0.77 μm and an effective particle volume of about 2.0 μm^3. The effective radius is slightly lower than the estimated radius of 1 μm, but this is easily explained by the fact that the particle will probably not become fully saturated in a magnetic field of only 2000 G. It is also expected that particles will not be uniformly magnetized, so their effective particle volume will usually appear smaller than the actual particle volume.

Data above 2000G was not used for the moment calculation because anistropy effects begin to change the slope of the curve requiring an anisotropy fit to one of the models discussed in section 4.2.3.

After the measurement discussed above was taken the same particle was saturated in a 9 T magnet. The measurement taken after saturation is shown in figure 4.15 One can now see that, although the general shape is the same, the curve has lost

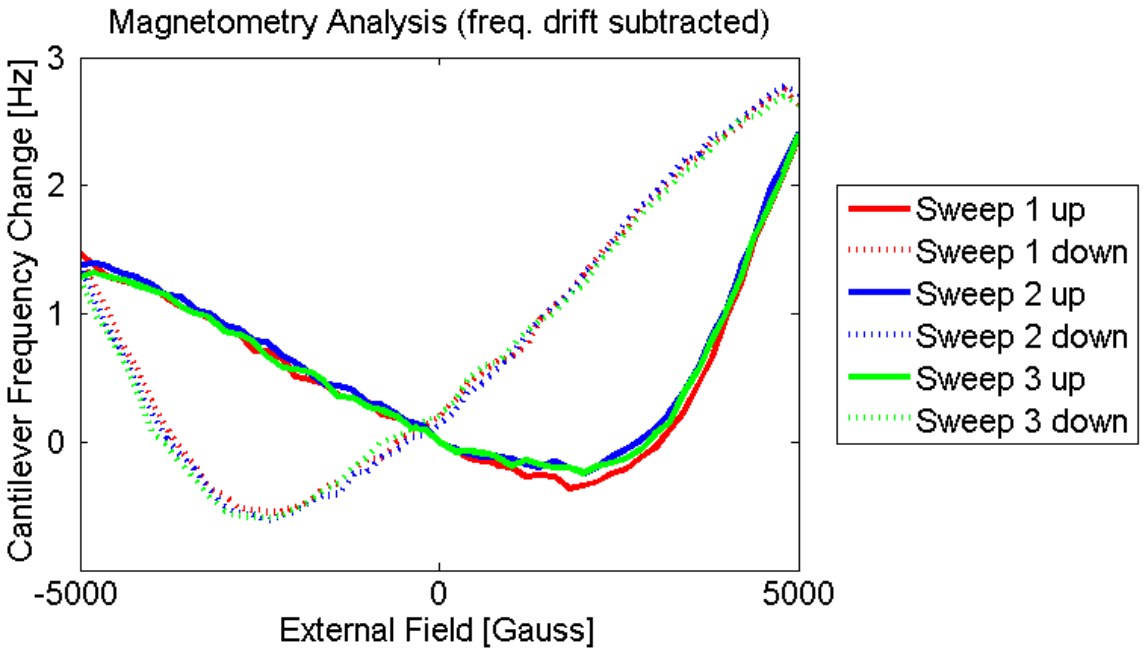

Figure 4.15: Magnetometer measurement of the same low-coercivity $Nd_2Fe_{14}B$ sphere from figure 4.14 after saturation.

symmetry. A possible explanation for this is that the particle has been saturated in the direction of positive field, and since the applied negative field is not enough to resaturate it in that direction, the hysteresis curve may retain some memory of its original saturation. As a result, the magnetic moment when positive field is applied

reaches a higher maximum than the magnetic moment when negative field is applied. Also, the coercive field ($\sim$ 2000 G) in the direction of positive external field is slightly less than the coercive field ($\sim$ 2400 G) in the negative direction of external field.

Weak Anisotropy Particle (4)

Figure 4.16 shows the magnetometry measurement results for a focused ion beam milled Sm_2Co_{17} particle on a Veeco silicon cantilever. An SEM micrograph of this

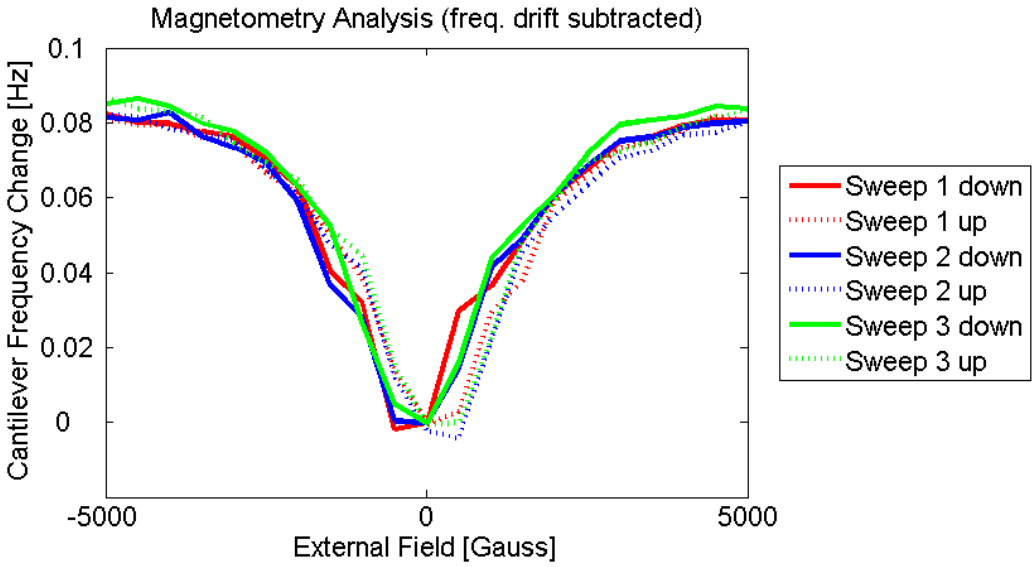

Figure 4.16: Magnetometry measurement of a focused ion beam milled Sm_2Co_{17} particle (see figure 4.17) with a weak anisotropy. $\mu = 5.5 \times 10^{-13}$ J/T

particle is shown figure 4.17 The measurement consisted of 3 field sweep loops from 5000 G to -5000 G and back. The data shown in figure 4.16 has been altered to, again, subtract out the average frequency drift between data points. The symmetry about the y-axis in this measurement is characteristic of a low coercivity particle, given the maximum applied field of only 5000 G. As mentioned earlier, the point where the

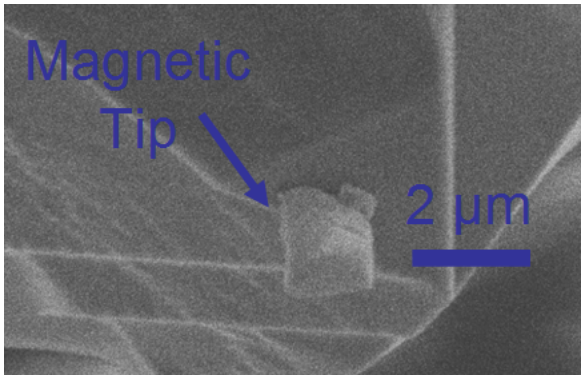

Figure 4.17: SEM micrograph of the focused ion beam milled Sm_2Co_{17} particle from the measurement in figure 4.16. The particle is glued on a Veeco silicon cantilever

slope of the curve changes sign indicates the coercive field of the particle, which is probably a little less than 500 G (0.05 T) for this particle. Based on the frequency shift from 0 G to 2000G the magnetic moment of this particle is around 5.5×10^{-13} J/T. This corresponds to a particle radius of about 0.5 μm and an effective particle volume around 0.6 μm^3. This agrees well with an estimate of the actual particle volume based on figure 4.17. The effective radius appears to be slightly less, but this is, again, is expected because the particle will probably not reach saturation at 2000 G and does not match the ideal assumption of uniform magnetization.

One thing unique about this measurement compared to previously discussed measurements is the flattening of the slope at high field. This indicates that the particle has low overall anistropy. As a result, the particle's magnetic axis begins to tilt toward the external field direction during oscillation as the external field is increased. This decreases the torque applied to the particle (compared to the torque if the particle's magnetization direction didn't tilt), resulting in a decreased frequency shift.

Models for this behavior based on magnetic energy minimization are discussed in section 4.2.3. Because the anisotropy of this particle is so low the slope of the curves at ±5000 G is almost zero. This indicates that the frequency shift is almost independant of magnetic field.

Small Coercive Sm_2Co_{17} Particle (5)

Figure 4.18 shows the magnetometer measurement of a small unmilled coercive Sm_2Co_{17} particle on triangular Veeco SiN cantilever (largest triangular cantilever on model # MLCT-NONM). An SEM micrograph of this particle is shown in figure

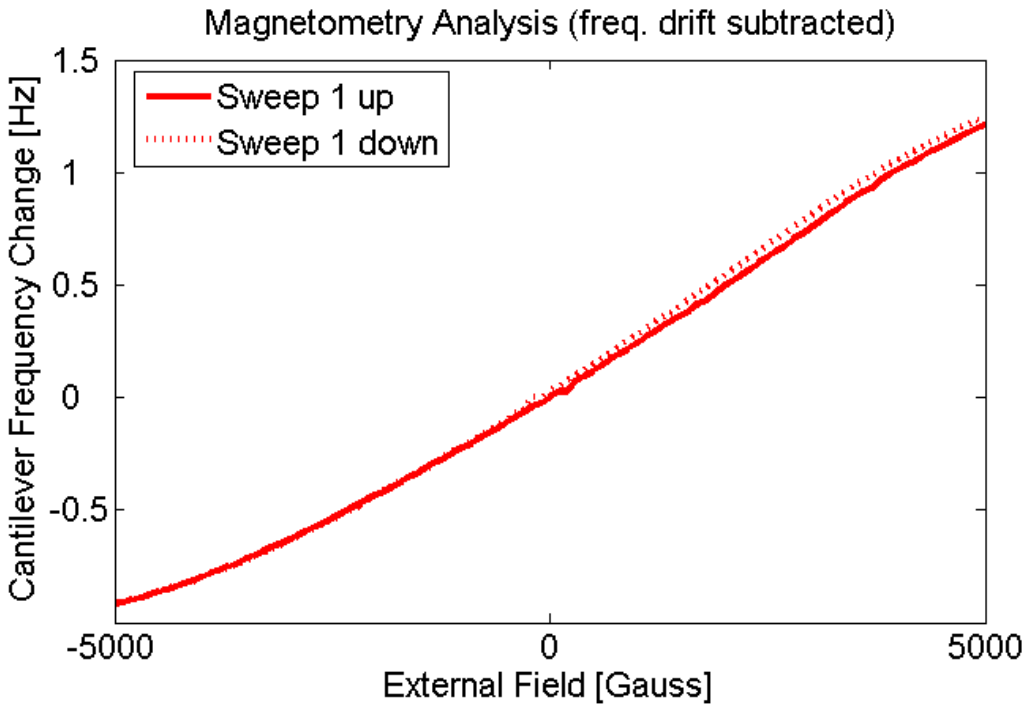

Figure 4.18: Magnetometer measurment of a small unmilled coercive Sm_2Co_{17} particle (see figure 4.19). $\mu = 5 \times 10^{-13}$ J/T

4.19. Based on the measurement in figure 4.18 the magnetic moment of this particle

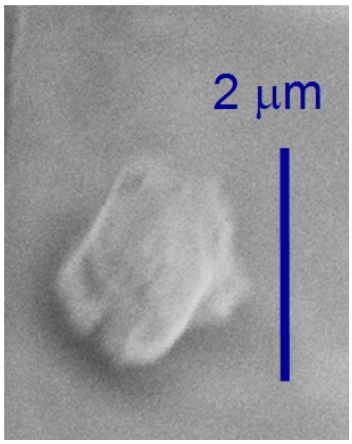

Figure 4.19: SEM micrograph of the small unmilled coercive Sm_2Co_{17} particle from the measurement in figure 4.18. This particle is glued to the end of a Veeco SiN triangular cantilever.

was calculated to be about 5×10^{-13} J/T. This corresponds to an effective radius of about 0.5 μm and an effective particle volume of about 0.5 μm^3, which is, again, only slighly less than one might estimate for the actual particle volume based on the SEM image in figure 4.19. The measurement in figure 4.18 also shows some slight curvature at high external fields which could be a result of external field miscalibration (due to nonlinear relationship between magnet current and external field), weak anisotropy, or both.

Small Non-coercive Sm_2Co_{17} Particle (6)

Figure 4.20 shows the magnetometer measurement of a focused ion beam milled Sm_2Co_{17} particle on the same type of SiN cantilever as the previous particle (5). An SEM micrograph of this particle is shown in figure 4.21. The calculated magnetic moment of this particle was approximately 1.3×10^{-13} J/T. This corresponds to an effective particle radius of 0.32 μm and an effective particle volume of 0.14 μm^3. From

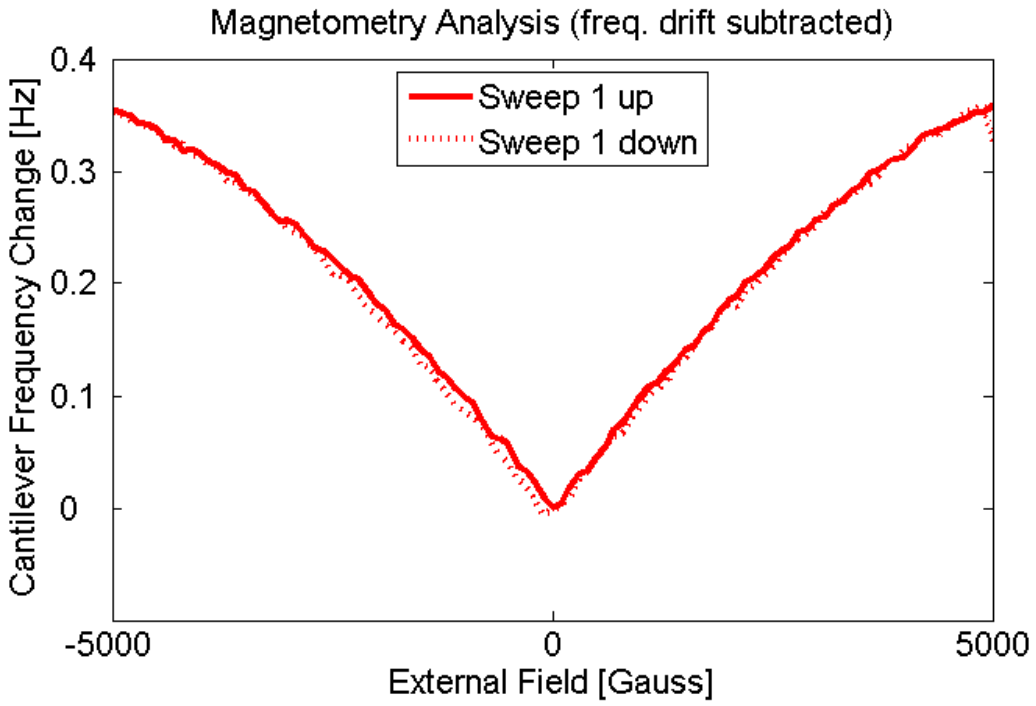

Figure 4.20: Magnetometer measurment of a small non-coercive focused ion beam milled Sm_2Co_{17} particle (see figure 4.21). $\mu = 1.3 \times 10^{-13}$ J/T

figure 4.20 it is clear that this particle has almost no coercivity, as the slope of the particle changes sign abruptly near zero field. The curvature shown in the measurement also indicates either a slightly low anisotropy and/or external field miscalibration.

4.4 Conclusions and Future Work

The data above supports the assertion that the room temperature cantilever magnetometer is a very sensitive intstrument for measuring the magnetic moment and hysteresis loops of micron and submicron particles. This makes the instrument extremely valuable for the development and testing of optimal MRFM magnetic cantilever tips. This method of tip characterization ultimately saves significant time and

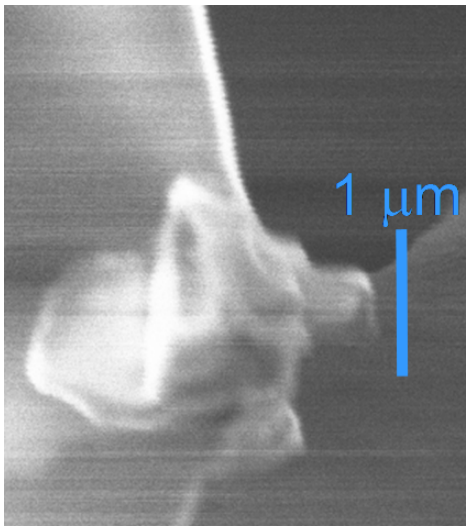

Figure 4.21: SEM micrograph of the Sm_2Co_{17} particle measured in figure 4.20.

money when trying to fabricate and select an appropriate magnetic tip for a specific experiment. The three main advantages the room temperature version has over instruments operating at cryogenic temperatures is its ease of, less time required for, and lower cost of operation. Some of the disadvantages are higher thermal noise, lower available external fields, and temperature instability. It is believed that this temperature instability is responsible for the cantilever frequency drift observed in many of the measurements shown earlier (although most of the particle measurements had been frequency drift corrected).

One of the main focuses of future work with this instrument will be the elimination of the frequency drift. This frequency drift presents a major obstacle to measurements with high resolution field sweep steps requiring significantly more time. Although a method of subtracting frequency drift was shown above to be fairly effective, this procedure only works well for short measurements where the frequency drift can

be approximated as being constant. Sometimes, even for short measurements, this approximation does not hold up very well, as evidenced by the variation between sweeps in figure 4.14. The first step in eliminating frequency drift will be to determine the cause. Since it is believed to be temperature related, the first course of action will be to monitor the alignment stage temperature using a thermal couple. If a correlation between frequency and temperature is found then a method of controlling the stage temperature will have to be implimented. One way of accomplishing this would be to add a temperature controller to the stage. One possible simple configuration would consist of a resistive heater and a thermal couple that can be used in a negative feedback loop. If the stage is kept above the temperature of the chilled water used to cool the magnet then the chilled water will act as a continuous source of cooling power that can be compensated with the resistive heater using a simple PID controller.

After the frequency drift problem is solved it would be desirable to begin investigating much smaller magnetic particles. To date, the magnitude of the frequency drift has made it difficult to measure such small particles with accuracy since the frequency drift on even a short time scale is much larger than the frequency shift expected from the moment of such small particles. Demonstration of the ability to measure small particles, such as that shown in [19], is important for improving the senstivity and resolution of the MRFM. The reason is that much smaller particles will be required the produce the higher gradients needed for increased sensitivity and resolution. Magnetic characterization of such particles via cantilever magnetometry will be an integral part of implementing these smaller tips in MRFM experiments.

CHAPTER 5

Conclusions

The magnetic resonance force microscope (MRFM) has great potential for bringing major scientific advancements in a variety of fields including chemistry, biology, materials science, and computing. If predictions of potential sensitivity and resolution are someday realized MRFM would provide the first method of three dimensional subsurface imaging with atomic resolution. This would allow the atomic level exploration of various materials and, particularly, biological molecules with much greater speed and precision that any current methods allow. The MRFM may also have the potential for implimenting quantum computation, allowing much higher data density than current data storage methods allow. To date, the MRFM has demonstrated single electron spin sensitivity with 25 nm spatial resolution [13] and a nuclear spin sensitivity of 1200 spins with spatial resolution of 90 nm [26], however, if advancements continue at the current pace it is only a matter of time before atomic level sensitivity is reached.

One of the most important parts of the MRFM is the magnetic tipped cantilever (or stationary magnetic, in the case of the sample on cantilever configuration) that serves as the probe. Many future improvements in sensitivity and resolution will be made through either the cantilever or magnetic tip. Lowering the thermal noise and

increasing the Q of the cantilever is one main objective. The other is increasing the magnetic field gradient of the magnetic tip. In this area, the focus of this research has been primarily on the magnetic tip fabrication and characterization. The approach taken here, manual particle gluing following by focused ion beam milling, has been proven to be an effective method of producing the high coercivity magnetic tips required for many MRFM experiments (specifically ESR experiments). Because of the variability in particle and cantilever properties it is necessary to characterize each individual probe to ensure it has the required properties for a given MRFM experiment. Cantilever magneometry has been shown, both in this paper and in other publications [19, 20], to be an effective method of characterizing these probes. The results presented earlier show that the magnetometer is a very sensitive instrument for characterizing the coercivity, anisotropy, hysteresis, and magnetic moment of micron scale particles. The main advantages of the room temperature magnetometer include easier and quicker measurement procedures , as well as lower cost of operation (compared with low temperature magnetometry). Using a room temperature magnetometer, measurements on moments as small as 10^{-13} J/T were demonstrated with estimated sensitivity as high as 3×10^{-16} J/T. In other magnetometers operating with superconducting magnets at cyrogenic temperatures, sensitivity around 3×10^{-20} J/T should be achievable with silicon cantilevers custom fabricated by Dan Rugar's research group at the IBM Almaden Research Center.

Several future research efforts will likely stem from the research presented here. One will be a focus on finding the cause of the well-documented magnetometer frequency drift, which is suspected to be temperature related, and implimenting a solution to counteract this cause. One possible solution is a temperature controlled

magnetometer alignment stage. A procedure for mathmatically subtracting frequency drift was shown to yield very repeatable hysteresis loops. Nonetheless, this procedure works only for short (temporally) measurements where frequency drift is relatively constant. A second area of future research will be in determining the mechanism causing the observed loss of coercivity in micron scale focused ion beam milled rare earth permanent magnets. Although this loss in coercivity is believed to be related to ion beam induced heating a definitive diagnosis would be helpful for devising a scheme for preventing the loss in coercivity during tip fabrication.

BIBLIOGRAPHY

[1] D. K. Pelekhov and P. C. Hammel, "Scanning probe microscopy with emphasis on magnetic resonance force microscopy," 2007, lecture Notes from Physics 880.A20, The Ohio State University.

[2] "Veeco instruments," http://www.veecoprobes.com/probes.asp, probes.

[3] K. R. Thurber, L. E. Harrell, and D. D. Smith, "170nm nuclear magnetic resonance imaging using magnetic resonance force microscopy," *Journal of Magnetic Resonance*, vol. 162, pp. 336–340, 2003.

[4] S. Tsuji, T. Masumizu, and Y. Yoshinari, "Magnetic resonance imaging of isolated single liposome by magnetic resonance force microscopy," *Journal of Magnetic Resonance*, vol. 167, pp. 211–220, 2004.

[5] Z. Zhang and P. C. Hammel, "Magnetic resonance force microscopy with a ferromagnetic tip mounted on the force detector," *Solid State Nuclear Magnetic Resonance*, vol. 11, pp. 65–72, 1998.

[6] D. P. DiVincenzo, "Two-bit gates are universal for quantum computation," *Physical Review A*, vol. 51, pp. 1015–1022, 1995.

[7] G. P. Berman, G. D. Doolen, P. C. Hammel, and V. I. Tsifrinovich, "Solid-state nuclear-spin quantum computer based on magnetic resonance force microscopy," *Physical Review B*, vol. 61, no. 21, pp. 14 694–14 699, 2000.

[8] J. A. Sidles, "Noninductive detection of single-proton magnetic resonance," *Applied Physics Letters*, vol. 58, no. 24, pp. 2854–2856, 1991.

[9] D. Rugar, C. S. Yannoni, and J. A. Sidles, "Mechanical detection of magnetic resonance," *Letters to Nature*, vol. 360, pp. 563–566, 1992.

[10] O. Züger and D. Rugar, "First images from a magnetic resonance force microscope," *Applied Physics Letters*, vol. 63, no. 18, pp. 2496–2498, 1993.

[11] ——, "Magnetic resonance detection and imaging using force microscope techniques (invited)," *Journal of Applied Physics*, vol. 75, no. 10, pp. 6211–6216, 1994.

[12] J. A. Sidles, J. L. Garbini, K. J. Bruland, D. Rugar, O. Züger, S. Hoen, and C. S. Yannoni, "Magnetic resonance force microscopy," *Reviews of Modern Physics*, vol. 67, no. 1, pp. 249–265, 1995.

[13] D. Rugar, R. Budaklan, H. J. Mamin, and B. W. Chul, "Single spin detection by magnetic resonance force microscopy," *Nature*, vol. 430, pp. 329–332, 2004.

[14] T. D. Stowe, K. Yasumura, T. W. Kenny, D. Botkin, K. Wago, and D. Rugar, "Attonewton force detection using ultrathin Silicon cantilevers," *Applied Physics Letters*, vol. 71, no. 2, pp. 288–290, 1997.

[15] N. E. Jenkins, L. P. DeFlores, J. Allen, T. N. Ng, S. R. Garner, S. Kuehn, J. M. Dawlaty, and J. A. Marohn, "Batch fabrication and characterization of ultrasensitive cantilevers with submicron magnetic tips," *Journal of Vacuum Science and Technology*, vol. 22, no. 3, pp. 909–915, 2004.

[16] K. Y. Yasumura, T. D. Stowe, E. M. Chow, T. Pfafman, T. W. Kenny, B. C. Snipe, and D. Rugar, "Quality factors in micron- and submicron-thick cantilevers," *Journal of Microelectromechanical Systems*, vol. 9, no. 1, pp. 117–125, 2000.

[17] C. Rossel, P. Bauer, D. Zech, J. Hofer, M. Willemin, and H. Keller, "Active microlevers as miniature torque magnetometers," *Journal of Applied Physics*, vol. 79, no. 11, pp. 8166–8173, 1996.

[18] T. Höpfl, D. Sander, H. Höche, and J. Kirschner, "Ultrahigh vacuum cantilever magnetometry with standard size single crystal substrates," *Review of Scientific Instruments*, vol. 72, no. 2, pp. 1495–1501, 2001.

[19] B. C. Snipe, H. J. Mamin, T. D. Stowe, T. W. Kenny, and D. Rugar, "Magnetic dissipation and fluctuations in individual nanomagnets measured by ultrasensitive cantilever magnetometry," *Physical Review Letters*, vol. 86, no. 13, pp. 2874–2877, 2001.

[20] T. N. Ng, N. E. Jenkins, and J. A. Marohn, "Thermomagnetic fluctuations and hysteresis loops of magnetic cantilevers for magnetic resonance force microscopy," *IEEE Transactions on Magnetics*, vol. 42, no. 3, pp. 378–381, 2006.

[21] C. P. Slichter, *Principles of Magnetic Resonance*, 3rd ed. New York: Springer-Verlag, 1996.

[22] D. Rugar, H. J. Mamin, and P. Guethner, "Improved fiber-optic interferometer for atomic force microscopy," *Applied Physics Letters*, vol. 55, no. 25, pp. 2588–2590, 1989.

[23] P. J. Mulhern, C. S. Arnold, B. L. Blackford, and M. H. Jericho, "A scanning force microscope with a fiber-optic-interferometer displacement sensor," *Review of Scientific Instruments*, vol. 62, no. 5, pp. 1280–1284, 1991.

[24] H. J. Mamin and D. Rugar, "Sub-attonewton force detection at millikelvin temperatures," *Applied Physics Letters*, vol. 79, no. 20, pp. 3358–3360, 2001.

[25] M.Poggio, C. L. Degen, C. T. Rettner, H. J. Mamin, and D. Rugar, "Nuclear magnetic resonance force microscopy with a microwire rf source," *Applied Physics Letters*, vol. 90, no. 26, pp. 263 111–263 111–3, 2007.

[26] H. J. Mamin, M. Poggio, C. L. Degen, and D. Rugar, "Nuclear magnetic resonance imaging with 90-nm resolution," *Nature Nanotechnology*, vol. 2, pp. 301–306, 2007.

[27] K. Wago, O. Züger, R. Kendrick, C. S. Yannoni, and D. Rugar, "Low-temperature magnetic resonance force detection," *Journal of Vacuum Science & Technology B*, vol. 14, no. 2, pp. 1197–1201, 1996.

[28] R. Skomski, "Domain-wall curvature and coercivity in pinning type Sm-Co magnets," *Journal of Applied Physics*, vol. 81, no. 8, pp. 5627–5629, 1997.

[29] B. Streibl, J. Fidler, and T. Schrefl, "Domain wall pinning in high temperature SM(Co, Fe, Cu, Zr)$_{7-8}$ magnets," *Journal of Applied Physics*, vol. 87, no. 9, pp. 4765–4767, 2000.

[30] Y. Sun, R. W. Gao, W. C. Feng, G. B. Han, G. Bai, and T. Liu, "Effect of grain size and distribution on the anisotropy and coercivity of nanocrystalline $Nd_2Fe_{14}B$ magnets," *Journal of Magnetism and Magnetic Materials*, vol. 306, pp. 108–111, 2006.

[31] J. D. Hannay, R. W. Chantrell, and D. Rugar, "Thermal field fluctuations in a magnetic tip/implications for magnetic resonance force microscopy," *Journal of Applied Physics*, vol. 87, no. 9, pp. 6827–6829, 2000.

[32] "Magnetic materials & components corp," http://www.mmcmagnetics.com /ourproducts/main_NdFeB.htm, 2003, neodymium iron boron Magnets.

[33] "Magnetic materials & components corp," http://www.mmcmagnetics.com /ourproducts/main_SmCo.htm, 2003, samarium cobalt Magnets.

[34] C. Park, J. A. Bain, T. W. Clinton, and P. A. A. van der Heijden, "Effects of focused-ion-beam irradiation on perpedicular write head performance," *Journal of Applied Physics*, vol. 93, no. 10, pp. 6459–6461, 2003.

[35] P. D. Rose, S. J. Brown, G. A. C. Jones, and D. A. Ritchie, "A method to profile ion beam line exposures *in situ* using STM," *Microelectronic Engineering*, vol. 41/42, pp. 229–232, 1998.

[36] A. A. Tseng, I. A. Insua, J. Park, and C. D. Chen, "Milling yield estimation in focused ion beam milling of two-layer substrates," *Journal of Micromechanics and Microengineering*, vol. 15, pp. 20–28, 2004.

[37] D. O. L., R. M. Langford, W. L. Chan, and A. K. Petford-Long, "Effect of Ga implantation on the magnetic properties of Permalloy thin films," *Journal of Applied Physics*, vol. 91, no. 12, pp. 9937–9942, 2002.

[38] S. Rubanov and P. R. Munroe, "FIB-induced damage in Silicon," *Journal of Microscopy*, vol. 214, pp. 213–221, 2004.

[39] ——, "Investigation of the structure of damage layers in TEM samples prepared using a focused ion beam," *Journal of Materials Science Letters*, vol. 20, pp. 1181–1183, 2001.

[40] J. P. McCaffrey, M. W. Phaneuf, and L. D. Madsen, "Surface damage formation during ion-beam thinning of samples for transmission electron microscopy," *Ultramicroscopy*, vol. 87, pp. 97–104, 2001.

[41] W. Brenza, H. Wanzenböck, A. Lugstein, E. Bertagnolli, E. Gornik, and J. Smoliner, "Focussed ion beam induced damage in Silicon studied by scanning capacitance microscopy," *Semiconductor Science and Technology*, vol. 18, pp. 195–198, 2003.

[42] N. I. Kato, Y. Kohno, and H. Saka, "Side-wall damage in a transmission electron microscopy specimen of crystalline Si prepared by focused ion beam etching," *Journal of Vacuum Science and Technology A*, vol. 17, no. 4, pp. 1201–1204, 1999.

[43] J. F. Walker and R. F. Broom, "Surface damage of semiconductor TEM samples prepared by focused ion beams," *Microscopy of Semiconducting Materials X, Institute of Physics Conference Series 157*, vol. 157, pp. 473–478, 1997.

[44] J. F. Zeigler, "Particle interactions with matter," http://www.srim.org, 2007.

[45] A. Fnidiki, F. Studer, J. Teillet, J. Juraszek, H. Pascard, and S. Meillon, "Damage processes in Fe_3O_4 magnetic insulator irradiated irradiated by swift heavy

ions. experimental results and modelisation," *The European Physical Journal B*, vol. 24, pp. 291–295, 2001.

[46] W. M. Kaminsky, G. A. C. Jones, N. K. Patel, W. E. Booij, M. G. Blamire, S. M. Gardiner, Y. B. Xu, and J. A. C. Bland, "Patterning ferromagnetism in $Ni_{80}Fe_{20}$ films via Ga^+ ion irradiation," *Applied Physics Letters*, vol. 78, no. 11, pp. 1589–1591, 2001.

[47] D. McGrouther, J. N. Chapman, and F. W. M. Vanhelmont, "Effect of Ga^+ ion irradiation on the structural and magnetic properties of CoFe/IrMn exchange biased bilayers," *Journal of Applied Physics*, vol. 95, no. 12, pp. 7772–7778, 2004.

[48] R. Ramesh, G. Thomas, and B. M. Ma, "Magnetization reversal in nucleation controlled magnets. II. effect of grain size and size distribution on intrinsic coercivity of Fe-Nd-b magnets," *Journal of Applied Physics*, vol. 64, no. 11, pp. 6416–6423, 1988.

[49] S. Szymura, H. Bala, Y. M. Rabinovich, V. V. Sergeev, G. Pawlowska, and D. V. Pokrovskii, "The dependence of coercivity and corrosion resistance on grain size in Nd–Fe–b-type sintered permanent magnets," *Journal of Physics: Condensed Matter*, vol. 3, pp. 5893–5901, 1991.

[50] O. V. Billoni, S. E. Urreta, L. M. Fabietti, and H. R. Bertorello, "Dependence of the coercivity on the grain size in a FeNdB + αFe nanocrystalline composite with enhanced remanence," *Journal of Magnetism and Magnetic Materials*, vol. 187, pp. 371–380, 1998.

[51] Y. Zhang, M. Corte-Real, and G. C. Hadjipanayis, "Magnetic hardening studies in sintered $Sm(Co,Cu_x,Fe,Zr)_z$ 2:17 high temperature magnets," *Journal of Applied Physics*, vol. 87, no. 9, pp. 6722–2000, 2000.

[52] C. H. Chen, S. Kodat, M. H. Walmer, S. Cheng, M. A. Willard, and V. G. Harris, "Effects of grain size and morphology on the coercivity of $Sm_2(Co_{1-x}Fe_x)_{17}$ based powders and spin cast ribbons," *Journal of Applied Physics*, vol. 93, no. 10, pp. 7966–7968, 2003.

[53] Y. Zhang, W. Tang, G. C. Hadjipanayis, C. H. Chen, D. Goll, and H. Kronmüller, "Magnetic domain structure in SmCo 2:17 permanent magnets," *IEEE Transactions on Magnetics*, vol. 39, no. 5, pp. 2905–2907, 2003.

[54] F. Wei-Cun, G. Ru-Wei, L. Wei, H. Guang-Bing, and S. Yan, "Dependence of coercivity on phase distribution and grain size in nanocomposite $Nd_2Fe_{14}B/\alpha$–Fe magnets," *Chinese Physics*, vol. 14, no. 8, pp. 1649–1652, 2005.

[55] G. A. Gibson and S. Schultz, "A high-sensitivity alternating-gradient magnetometer for use in quantifying magnetic force microscopy," *Journal of Applied Physics*, vol. 69, no. 8, pp. 5880–5882, 1991.

[56] P. M. Morse and K. U. Ingard, *Theoretical Accoustics*. New York: McGraw-Hill, 1968.

[57] J. A. Marohn, R. Fainchtein, and D. D. Smith, "An optimal magnetic tip configuration for magnetic-resonance force microscopy of microscale buried features," *Applied Physics Letters*, vol. 73, no. 25, pp. 3778–3780, 1998.

[58] S. Hirosawa, Y. Matsuura, H. Yamamoto, S. Fujimura, M. Sagawa, and H. Yamauchi, "Magnetization and magnetic anisotropy of $R_2Fe_{14}B$ measured on single crystals," *Journal of Applied Physics*, vol. 59, no. 3, pp. 873–879, 1986.

[59] Y. Obukhov, K. C. Fong, D. Daughton, and P. C. Hammel, "Real time cantilever signal frequency determination using digital signal processing," *Journal of Applied Physics*, vol. 101, no. 3, pp. 034 315–034 315–5, 2007.

[60] S. W. K. Yuan, "Thermal and mechanical properties of G-10CR," Yutopian Online, 2000, http://www.yutopian.com/Yuan/prop/G10.html.